Trapping of Ba^+ using an Autoionizing Resonance and Construction of an Academic Ba^+ Testbed

by

Noah Greenberg

A thesis
presented to the University of Waterloo
in fulfillment of the
thesis requirement for the degree of
Doctor of Philosophy
in
Physics

Waterloo, Ontario, Canada, 2024
© Noah Greenberg 2024

Examining Committee Membership

The following served on the Examining Committee for this thesis. The decision of the Examining Committee is by majority vote.

External Examiner:	David Lucas Professor, Dept. of Physics, University of Oxford
Supervisor(s):	Crystal Senko Associate Professor, Dept. of Physics and Astronomy, University of Waterloo
Internal Member:	Alan Jamison Assistant Professor, Dept. of Physics and Astronomy, University of Waterloo
Internal-External Member:	Michal Bajcsy Associate Professor, Dept. of Electrical and Computer Engineering, University of Waterloo
Other Member(s):	Dmitry Pushin Associate Professor, Dept. of Physics and Astronomy, University of Waterloo

Author's Declaration

I hereby declare that I am the sole author of this thesis. This is a true copy of the thesis, including any required final revisions, as accepted by my examiners.

I understand that my thesis may be made electronically available to the public.

Abstract

Trapped ions are at the forefront of the quantum information processing field. This platform has demonstrated some of the highest native gate fidelities, in addition to offering fully connected qubits with incredibly long coherence and trapping lifetimes. Among the trapped ion candidates, barium is emerging as one of the top contenders. Barium has a long lived metastable state, which can either be exploited to greatly increase the fidelity of processes like state preparation or can be used to store information in additional hyperfine levels. This attractive atomic structure, combined with the fact that many transitions fall within the visible wavelength spectrum, eases optical design and makes barium an ideal trapped ion candidate to move the technology forward.

Researchers have been working with barium ions for decades, but quickly trapping long chains of this element is more of a challenge compared with other species because it reacts in the atmosphere forming oxides and salts. Furthermore, the two most promising isotopes of barium, $^{137}Ba^+$ and $^{133}Ba^+$, have their own added barriers, with the former being a mere $\sim 11\%$ naturally abundant and the latter usable in only microgram quantities due to its radioactivity. Improving the loading efficiency of these isotopes will be key to reliably generating long chains of these ions, and realizing quantum information processing with barium in the most complex trapped ion platforms the technology has to offer. To this end, we demonstrate the use of an autoionizing transition to increase our loading rate of Ba^+ by a factor of ~ 7 compared with a non-resonant photoionization scheme. We utilize the largest experimentally measured photoionization cross-section in barium, which is the most power efficient scheme that exists for generating Ba^+ from neutral atoms in an isotope-selective manner. This is the first reported use of an autoionizing transition to trap Ba^+ and this scheme is applicable to all isotopes of barium.

In order to further aid in trapping of the most elusive isotope, $^{133}Ba^+$, methods for fabricating microgram quantity targets for ablation loading trapped ions are also presented. Loading an ion trap with microgram materials of any element is incredibly difficult, and even more so when it only exists as a salt, as is the case with $^{133}Ba^+$. Heat-treatment of these salt ablation targets is shown to increase the consistency of neutral barium production as well as the lifetime of the ablation target, which will make trapping more predictable.

The work surrounding the use of a novel photoionization scheme and testing of ablation targets was done in order to facilitate the reliable trapping of long chains of Ba^+ in a surface trap. The design and initial construction of an ultra-high vacuum system and the supporting optical infrastructure for eventually trapping Ba^+ in a chip trap is detailed and evaluated as well. This vacuum chamber prioritizes optical access for individual addressing ions to drive laser-based gates and allow imaging of ion chains, while still maintaining sufficient optical access for multiple global addressing zones. This chamber and experiment

will serve as a platform to further probe Ba^+ as a front running candidate for quantum simulation and information processing in one of the most sophisticated surface trap that exists. Finally, studies of an alternative approach for driving amplitude-modulated entangling gates between ion pairs in chains is numerically simulated. This technique leverages existing practices found in signal processing for driving spin-spin interactions in ion pairs via their collective motional modes. The purpose of this numerical project is to provide a basis for creating pulse-shapes that will entangle ions and act as a resource for when the platform has the capability to manipulate qubits.

Acknowledgements

I would like to thank Transformative Quantum Technologies for providing the funding, infrastructure, and support for many of the projects contained in this thesis. I would also like to thank the team at RAC II for their help, in particular: Don Carkner for all things related to the building (like helping me install optical tables), Sara Clark for her involvement in procuring the many necessary components to build these experiments, and Alex Mitrovic for machining the intricate designs that we, somewhat naively, create in our CAD programs. Furthermore, I would like to thank the University of Waterloo QNFCF team. I have had the opportunity to utilize many of the machines maintained and operated by the nanofab as we have built up the lab.

I have had the pleasure of working with many graduate students over the past few years, that have uniquely shaped my experience, and from whom I have garnered innumerable valuable insights. First and foremost, I would to thank Brendan Bramman and Pei Jiang Low for being a resource when needed and providing assistance when I was running experiments on the four-rod Paul trap. I would also like to thank Richard Rademacher for his advice, irrespective of the exact problem I was facing, and for teaching me how to communicate complex designs between teams on large-scale projects. Relating to vacuum work, I would like to acknowledge Sainath Motlakunta and Nikhil Kotibhaskar for allowing us to use their setup for prebaking and for the many conversations that we have had relating to the technicalities of attaining ultra-high vacuum. Now at Columbia University, Ali Binai-Motlagh, was a tremendous assist when initially building and testing our vacuum system as well. I would also like to acknowledge Stephen Del Grosso Milek's work in helping to draw many machined parts and assembly of optical pegboards as he spent two CO-OP terms with us. To the next generation of graduate students on the project; Collin Epstein, Xinghe Tan, Ana Bershanska, Akimasa Ihara and Ali Mustafa Khatai, I have enjoyed working with you all and I thank you for your enthusiasm. I have no doubt that many interesting experiments lie ahead.

I have had the opportunity to work with five post-doctoral researchers, from whom I have gleaned precious lessons: Roland Hablützel, Matt Day, Virginia Frey, Mahmood Sabooni, and Akbar Jahangiri Jozani. Most recently, it has been a joy and productive past 18 months working with Akbar as we edge closer to getting the surface trap project online. I would also like to thank my committee members: Alan Jamison, Dmitry Pushin, and Thomas Jennewein for providing me with their guidance over the years, especially when it came to motivating the autoionizing experiments. Many of the results in this thesis would likely not exist without their direction. I would also like to thank Rajibul Islam for the guidance he has given me over the past five years.

Finally, I would like to thank my advisor, Crystal Senko, for everything.

Dedication

This thesis is dedicated to my loving fiancée, Jessa, and to my parents for their unwavering support. I would also like to dedicate this to all the ion trappers out there—happy trapping!

Table of Contents

Examining Committee Membership ii

Author's Declaration iii

Abstract iv

Acknowledgements vi

Dedication vii

List of Figures xi

List of Tables xiv

1 Introduction 1

1.1 Background 4

1.1.1 $^{133}Ba^{+}$ Atomic Structure 6

2 Exploiting an Autoionizing Resonance to Trap Ba^{+} 9

2.1 Motivation and Context 10

2.2 Experimental Overview 14

2.3 Saturation of the Loading Rate 18

2.4 Loading Rate Comparison 21

2.4.1 $^{138}Ba^{+}$ Loading Rates . . . 21
2.4.2 $^{137}Ba^{+}$ Loading Rates . . . 24
2.5 Discussion and Outlook . . . 25

3 Barium Chloride Ablation Targets **29**
3.1 Motivation for Testing $BaCl_2$ Atomic Sources . . . 30
3.2 Deposition of $BaCl_2$ . . . 33
3.2.1 Deposition Process . . . 34
3.3 Heat-Treatment of Ablation Targets . . . 35
3.3.1 Resistive Melting of $BaCl_2$ on Platinum . . . 35
3.3.2 High-Vacuum Heating of Aluminium with $BaCl_2$ . . . 37
3.4 Energy Dispersive X-Ray Spectroscopy . . . 39
3.4.1 Post-Deposition Spectroscopy of $BaCl_2$ Ablation Targets . . . 40
3.5 Neutral Fluorescence Collection . . . 41
3.5.1 Experimental Setup . . . 43
3.5.2 Spot Lifetimes of 5 μg $BaCl_2$ Ablation Targets . . . 44
3.6 Testing Macroscopic Ablation Targets . . . 48
3.6.1 Trap Contamination . . . 49
3.6.2 Spot Lifetimes of Macroscopic Targets . . . 50
3.7 Concluding Remarks . . . 53

4 Infrastructure for a Chip Trap **55**
4.1 Vacuum Overview . . . 57
4.1.1 Experiment Chamber . . . 61
4.2 Initial Construction and Testing . . . 64
4.3 Trap Alignment and Additional Infrastructure . . . 69
4.4 Optical Infrastructure . . . 71
4.5 Current State . . . 76

5 Amplitude-Modulated Entangling Gates **78**
5.1 Background and Motivation . . . 78
5.2 Bichromatic Laser Field Hamiltonian Simulations . . . 81
5.3 Mølmer–Sørensen Hamiltonian Simulations . . . 84
5.3.1 Double-Sideband Amplitude Modulation . . . 87
5.3.2 Detuning and Rabi Frequency Errors . . . 97
5.3.3 Introducing Noise . . . 99
5.4 Outlook . . . 102

6 Conclusion **104**

References **106**

APPENDICES **123**

A Barium Atomic Sources **124**
A.1 Optical Profilometer Measurements . . . 124
A.2 Optical Beampaths for Barium Ablation Testing . . . 125
A.3 Selected SEM Images of Ablation Targets . . . 128
A.4 Metallic ^{133}Ba Recipe . . . 129

B Infrastructure **131**
B.1 Electrical Infrastructure . . . 131

C Amplitude-Modulated Entangling Gates **135**
C.1 Code Description . . . 135
C.2 Analytical Expression for α_{ij} Integral using Double-Sideband Amplitude Modulation . . . 137
C.3 Amplitude-Modulation in Long Ion Chains . . . 138

List of Figures

1.1 Mass Spectrometer Patent 5
1.2 Four-Rod Paul Trap 6
1.3 $^{133}Ba^{+}$ Atomic Structure 7

2.1 Relevant Neutral Barium Structure 11
2.2 Various Two-Step Isotope-Selective Photoionization Schemes for Trapping Ba^{+} 14
2.3 Experimental Overview for Trapping Ba^{+} with an Autoionizing Resonance 17
2.4 Loading Rate (Ions/Pulse) Comparison 19
2.5 Compared Isotope-Selective Loading Rates of $^{138}Ba^{+}$ 21
2.6 Compared Isotope-Selective Loading Rates of $^{137}Ba^{+}$ 24
2.7 Dark and Dim Ions in a Chain 26
2.8 Mosaic of $^{138}Ba^{+}$ Chains 28

3.1 $BaCl_2$ Fracturing, Ring Formation, & Ablation Targets 31
3.2 Deposition Setup for $BaCl_2$ 33
3.3 Methods for Heat-Treatment of $BaCl_2$ Ablation Targets 37
3.4 Typical Energy Dispersive X-Ray Spectroscopy of $BaCl_2$ Ablation Targets 39
3.5 EDS of Pt and Pt* Ablation Targets Post-Deposition 40
3.6 Neutral Barium Fluorescence Spectrum 41
3.7 Ablation Experimental Overview 43
3.8 SEM Images and Lifetimes of ~ 5 μg Ablation Targets 45

3.9 Longest Lasting 5 μg Ablation Spots for Pt, Pt*, & Al Targets 47
3.10 EDS and SEM Images of Platinum Targets after Ablation 48
3.11 Trap Contamination due to Ablation of $BaCl_2$ 49
3.12 Spot Lifetimes of Macroscopic Pt* $BaCl_2$ Ablation Targets 51
3.13 SEM Image after Ablation of a ~ 5 μg Pt Target 52
3.14 SEM and EDS Images of ~ 2 mg $BaCl_2$ Ablation Targets 53

4.1 Beam Orientation and Phoenix Trap 56
4.2 $^{133}Ba^{+}$ Testbed Project Timeline 57
4.3 Ultra-High Vacuum Overview 60
4.4 CAD Rendering of the Re-Entrant Viewports 62
4.5 CAD Rendering of the Internal Vacuum Components 63
4.6 Prebaking Stainless Steel Components 65
4.7 Baking and Pressure Testing 67
4.8 Trap Alignment Process 69
4.9 Lead Castle 70
4.10 Achromatic Telescope Design 73
4.11 Optical Pegboards for Globally Addressing Ions 74
4.12 Optical Table Layout 75
4.13 Beam Preparation 76

5.1 CNOT Constructed from Native Gates 80
5.2 Bichromatic Evolution of an Ion Pair Spin System via a Single Motional Mode 82
5.3 Bell State Fidelity of an Ion Pair with Varying Parameters 84
5.4 Mølmer–Sørensen Hamiltonian Example with Two Ions and a Single Mode 86
5.5 Constant Pulse Example for a Chain of Three Ions 91
5.6 Results for a Three Ion Chain using DSAM Example 1 93
5.7 Results for a Three Ion Chain using DSAM Example 2 95
5.8 Results for a Three Ion Chain using DSAM Example 3 96

5.9 Detuning and Rabi Errors in an Amplitude Modulated Scheme 98
5.10 Impact of Mode Noise on Fidelity 99
5.11 Motional Mode Noise Simulation Example 1 100
5.12 Motional Mode Noise Simulation Example 2 101
5.13 Rabi Frequency Fluctuation Noise Examples 102

A.1 Estimation of $BaCl_2$ Ring Thickness and Ablation Spot Size 124
A.2 Ablation Beampath CAD Image 125
A.3 Ablation Beampath Optical Diagram 127
A.4 SEM Image after Ablation of a ~ 5 μg Pt Target 128
A.5 $BaCl_2$ Crystal Contamination on Microfabricated Au Chips 129

B.1 AHU Feedthrough 132
B.2 Resonator Support Structure 133

C.1 Phase-Space Trajectories for a Chain of Five Ions 138

List of Tables

2.1 Intermediate Levels for Isotope-Selective Loading of Ba^+ 12
2.2 Autoionizing States Accessible from the $6\,s\,6\,p\,{}^1P_1$ Level 27

3.1 Average Spot Lifetimes of 5 μg $BaCl_2$ Ablation Targets 46
3.2 Average Spot Lifetimes of Macroscopic Pt* $BaCl_2$ Ablation Targets 50

5.1 Parameters for Bichromatic Hamiltonian Simulations 83
5.2 Parameters for Mølmer–Sørensen Hamiltonian Simulations 87
5.3 Parameters for DSAM Optimization 92

Chapter 1

Introduction

Nearly three decades ago, the quantum computing "revolution" kicked off with the advent of algorithms that promised either exponential [1] or quadratic speedup [2] compared with their classical counterparts. It was during this same period of time that many fundamental processes for laser cooling ions [3] and realizing quantum logic with trapped ions [4] came to fruition as well. While these algorithms have been realized with trapped ions [5, 6], the pinnacle of what could be achieved with a theorist's idealised quantum computer has yet to be demonstrated. There is no doubt that quantum information processing has come a long way from a practical standpoint since the 1990's. There are many platforms with incredible promise and results such as neutral atoms [7] and superconducting qubits [8], in addition to the trapped ion platform [9, 10]. Like all quantum computing platforms, trapped ions utilize the quantum mechanical superposition property, and subsequently exploit quantum entanglement in order to gain advantage over classical computers. This property of superposition, where the quantum state of a qubit can be described in terms of complex amplitudes $\Psi = a\,|0\rangle + b\,|1\rangle$ rather than a single whole number is the fundamental difference between quantum and classical computers [11].

In the near term, the focus and applications of quantum computing will likely land in the realm of quantum simulation, wherein which these programmable machines will have the ability to take on and model different quantum mechanical systems in a more efficient manner than what can be achieved classically [12]. In this sense, quantum computers will be built for solving more specific problems, that are still very much tied to the hardware that is built to solve them. The challenges faced today in quantum information processing, which aims to enhance quantum simulation tools or eventually achieve quantum computing, revolves around identifying and mitigating experimental noise sources that cause decoherence [13]. This is made possible thanks to proof-of-principle experiments that have paved

the way forward for this technology [14, 15, 16]. Attacking issues that are limiting native gate fidelities in trapped ions, like laser intensity fluctuations [17, 18], magnetic field noise [19], and heating rates [20] is the main concern and can be done through repeated iteration of designs. At this point, the maturity of trapped ion quantum computing technology is such that major gains will not be made overnight, but that progress will be obtained through thoughtful engineering. A powerful and useful quantum simulator must consist of at least tens of ions in a single trap, if not $\sim$ 100 ions [21], in order to evolve a Hilbert space that cannot be fully constructed on classical computers.

Besides quantum simulation, another goal of these computers will be to perform quantum error correction, which as been initially demonstrated with trapped ions [22] and neutral atoms [23]. For this to be accomplished, the quantum computer must be operating in a regime where the error rates are below a specified threshold [24]. While there has been evidence that this threshold may exist at the $\approx$ 1% gate error level [25], in practicality, since the experimental apparatuses are so physically large for trapped ions, scaling to hundreds of physical qubits (with many less logical qubits) may be a significant challenge and will require that the native gate infidelities operate far below this level. Some highlights that have been accomplished in an industry setting using the trapped ion platform are state-preparation and measurement (SPAM), single qubit, and two qubit gate fidelities of $\sim$ 0.99839, 0.999975, and 0.998155, respectively [26]. This was demonstrated on a platform with 32 trapped ion qubits. Similarly, on a different trapped ion platform with 29 qubits, the reported SPAM, single qubit, and two qubit gate fidelities are $\sim$ 0.995, 0.9998, and 0.99536, respectively [27]. With enough physical qubits, these fidelities would be acceptable for building a fault-tolerant machine, but given that the hardware is still relatively large, noisy, and difficult to work with, it is quite the engineering challenge to obtain the number of required physical qubits. What can help to solve this problem is by maximizing the number of ions that can be utilized in each trap, which will require loading many ions of a specific isotope quickly.

In general, there are two main architectures that deal with scaling the trapped ion platform; the quantum charge-coupled device (QCCD) [28, 29, 30, 31] and elementary logical unit (ELU) models [32, 33]. The QCCD relies on shuttling pairs of ions between different zones designated for different operations such as measurement, entanglement, and loading. On the other hand, the ELU model connects chains of ions across many different traps (nodes), requiring the internal spin state of the ions to be entangled with a flying qubit (photon), via a measurable quantity like polarization [34]. Beyond the QCCD and ELU model, the scaling pathway can be further broken down into laser-free [35, 36] or laser-based entangling gates [37, 38]. All of these schemes have advantages and disadvantages, but what is clear is that they all relay on the assumption that loading large quantities of

ions of a specific isotope will be available on-demand.

To date, the vast majority of the most complex trapped ion machines in both industry and academia use either Yb^+ [21, 27, 26, 39] or Ca^+ [29, 40, 37] for quantum information processing. However, in the past couple of years more attention has been turning toward using Ba^+ as the processing qubit [41] and even in the cases where Ba^+ is not used as the processing qubit, it still often plays a crucial role for sympathetic cooling each Yb^+ qubit or networking between nodes [42]. In some of the most advanced trapped ion machines that exist [26], there is a demand to be able to load large numbers of Ba^+ ions efficiently, which can be more of a challenge, when compared with other alkaline-earth metals [43].

This thesis does not deal specifically with qubits, but on the construction of a Ba^+ academic testbed and solving initial issues regarding the loading of Ba^+ ions. The highlight of this thesis is the demonstration of a novel photoionization scheme for isotope-selectively loading Ba^+ ions [44]. This scheme takes advantage of the rich ionization structure of neutral barium, by utilizing an autoionizing transition to more efficiently photoionize barium, making the initial creation of these ion chains easier. Besides evaluating different photoionization schemes, there is also considerable work relating to the development of a reliable Ba^+ source for ablation loading [45]. Creating more uniform ablation targets is another key aspect of the experiment that makes loading Ba^+ more consistent, and it is of particular importance when considering the radioactive $^{133}Ba^+$ isotope. Work is also presented regarding building the necessary infrastructure to trap long chains of Ba^+ ions in a sophisticated surface trap [46] so that future experiments can probe new ways of encoding information in this exciting qubit [47] and eventually demonstrate laser-based entangling gates in Ba^+ chains for quantum simulation or information processing applications. This includes details of the construction and testing of a high optical access, ultra-high vacuum (UHV) titanium chamber for housing the ion trap as well as optical designs for photoionization and laser cooling. Finally, simulated results are outlined for eventually driving high-fidelity two-qubit gates in trapped ion chains on the aforementioned experimental apparatus. The thesis is outlined below:

- Section 1.1: Background information as it pertains to Paul traps and the atomic structure of Ba^+.
- Section 2: Experimental evaluation of trapping Ba^+ using an autoionizing resonance.
- Section 3: Atomic source development of microgram quantity salt targets for ablation loading of radioactive Ba^+.
- Section 4: Construction of vacuum and optical systems for a surface trap, supporting the trapping of long chains of Ba^+.

- Section 5: Numerical pulse-shaping Hamiltonian simulations for driving high-fidelity entangling gates in pairs of trapped ions for work with the Ba^+ qubit.

This thesis has resulted in two first-author manuscripts [44, 48]. Although not directly related, my involvement and contributions to other work while in graduate school have helped to shape this thesis as well [43, 49, 50, 51].

1.1 Background

For much of the 20$^{\text{th}}$ century, physicists worked with ensembles of particles, primarily atoms, studying their behavior as an entire collection [52, 53]. It was not until the last half of the century that the study of individually trapped particles began to take shape, due to the invention of the quadrupole mass filter originally designed and demonstrated by Nobel Laureate Wolfgang Paul in the 1950's [54]. This invention, shown in Fig. 1.1, led to what is known as the Paul trap, which is the basis for quantum information processing with trapped ions.

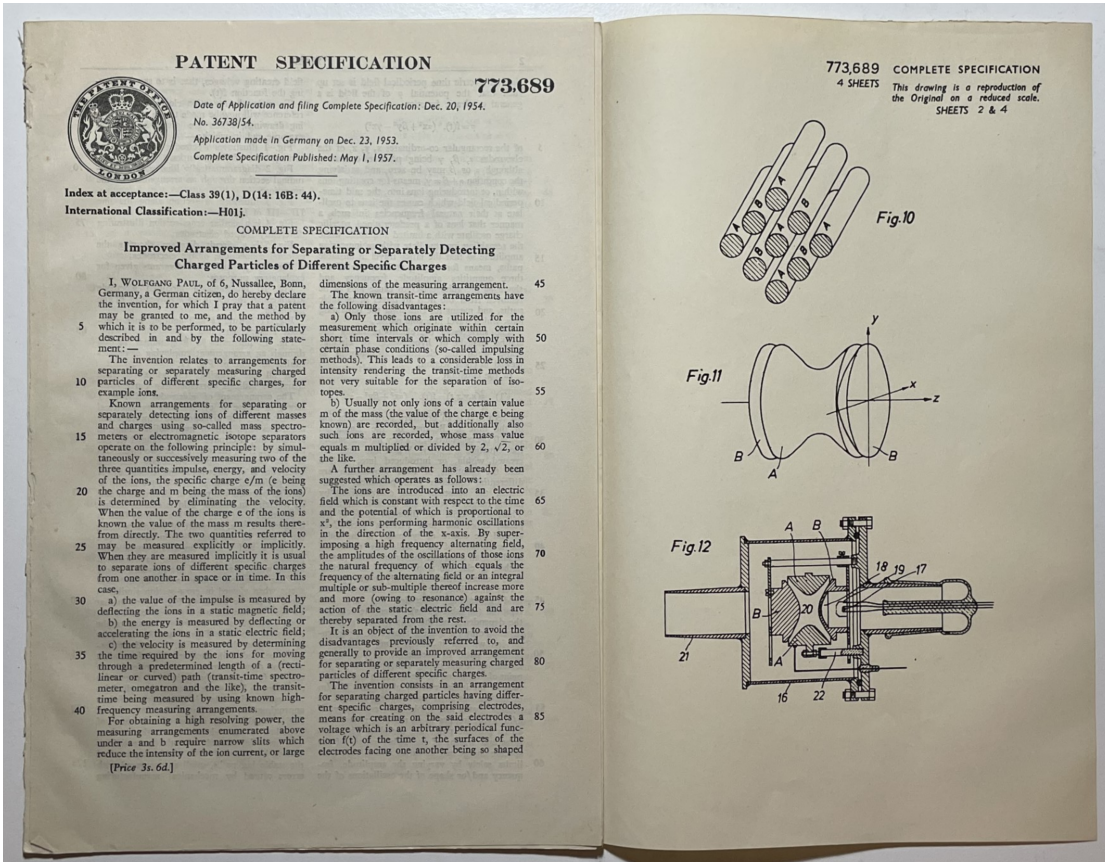
The Paul trap uses both static and time varying electric fields to create a "pseudo-potential" that will oscillate at a specific frequency, confining the ion. Considering the specific case of a quadrupole configuration with entirely positive voltages that is not time varying, then a cation starting at the center of the quadrupole configuration would follow the field lines out of the trap, between two poles. In fact it can be shown that it is not possible to trap charged particles with static electric fields [55]. However, if an opposite pair of poles in the quadrupole configuration originates with negative voltages and this voltage oscillates to become positive, while at the same time the other pair oscillates inversely, individually charged particles can become trapped. By adjusting the parameters of the device such as the quadrupole dimensions (distance between the poles), the peak voltages, or the frequency of the time varying field, an ion of a specific mass m can be trapped in a stable manner with additional axial confinement [56].

The frequency of the ions motion in a Paul trap can be simply described by the Eq. 1.1 [57], where e is the elementary charge, V is the peak voltage, Ω_{trap} is the frequency of the voltage oscillations, and r is the distance of the ion from the electrode.

$$\omega_s = \frac{eV}{\sqrt{2}m\Omega_{trap}r^2} \tag{1.1}$$

There are two different traps discussed in this thesis, a four-rod Paul trap and a microfabricated trap. A four-rod Paul trap is depicted in Fig. 1.2, which was fabricated with

the intent of exploring a metastable state in $^{137}Ba^{+}$ for the purposes of encoding more information in the atomic structure as a qudit [58]. In this thesis, a photoionization experiment was conducted on this trap, demonstrating more efficient loading of Ba^{+} ions. This trap most closely resembles original Paul traps, with end cap needles for confining the ions axially. Another trap, discussed in Section 4 is a surface or chip trap, which is microfabricated. Due to the consistency of fabrication and complexity of the device, giving more precise control over the ions motion, microfabricated traps are believed to be the only viable path to scale this technology [59, 60, 61, 62, 63].



PATENT SPECIFICATION

773,689

Date of Application and filing Complete Specification: Dec. 20, 1954.
No. 36738/54.
Application made in Germany on Dec. 23, 1953.
Complete Specification Published: May 1, 1957.

Index at acceptance:—Class 39(1), D(14: 16B: 44).
International Classification:—H01j.

COMPLETE SPECIFICATION

Improved Arrangements for Separating or Separately Detecting Charged Particles of Different Specific Charges

I, WOLFGANG PAUL, of 6, Nussallee, Bonn, Germany, a German citizen, do hereby declare the invention, for which I pray that a patent may be granted to me, and the method by which it is to be performed, to be particularly described in and by the following statement:—

The invention relates to arrangements for separating or separately measuring charged particles of different specific charges, for example ions.

Known arrangements for separating or separately detecting ions of different masses and charges using so-called mass spectrometers or electromagnetic isotope separators operate on the following principle: by simultaneously or successively measuring two of the three quantities impulse, energy, and velocity of the ions, the specific charge e/m (e being the charge and m being the mass of the ions) is determined by eliminating the velocity. When the value of the charge e of the ions is known the value of the mass m results therefrom directly. The two quantities referred to may be measured explicitly or implicitly. When they are measured implicitly it is usual to separate ions of different specific charges from one another in space or in time. In this case,

a) the value of the impulse is measured by deflecting the ions in a static magnetic field;
b) the energy is measured by deflecting or accelerating the ions in a static electric field;
c) the velocity is measured by determining the time required by the ions for moving through a predetermined length of a (rectilinear or curved) path (transit-time spectrometer, omegatron and the like), the transit-time being measured by using known high-frequency measuring arrangements.

For obtaining a high resolving power, the measuring arrangements enumerated above under a and b require narrow slits which reduce the intensity of the ion current, or large

[Price 3s. 6d.]

dimensions of the measuring arrangement.

The known transit-time arrangements have the following disadvantages:

a) Only those ions are utilized for the measurement which originate within certain short time intervals or which comply with certain phase conditions (so-called impulsing methods). This leads to a considerable loss in intensity rendering the transit-time methods not very suitable for the separation of isotopes.

b) Usually not only ions of a certain value m of the mass (the value of the charge e being known) are recorded, but additionally also such ions are recorded, whose mass value equals m multiplied or divided by 2, $\sqrt{2}$, or the like.

A further arrangement has already been suggested which operates as follows:

The ions are introduced into an electric field which is constant with respect to the time and the potential of which is proportional to x^2, the ions performing harmonic oscillations in the direction of the x-axis. By superimposing a high frequency alternating field, the amplitudes of the oscillations of those ions the natural frequency of which equals the frequency of the alternating field or an integral multiple or sub-multiple thereof increase more and more (owing to resonance) against the action of the static electric field and are thereby separated from the rest.

It is an object of the invention to avoid the disadvantages previously referred to, and generally to provide an improved arrangement for separating or separately measuring charged particles of different specific charges.

The invention consists in an arrangement for separating charged particles having different specific charges, comprising electrodes, means for creating on the said electrodes a voltage which is an arbitrary periodical function f(t) of the time t, the surfaces of the electrodes facing one another being so shaped

773,689 COMPLETE SPECIFICATION
4 SHEETS
This drawing is a reproduction of the Original on a reduced scale.
SHEETS 2 & 4

Fig.10

Fig.11

Fig.12

Figure 1.1: Image of a patent from the U.K. detailing the mass spectrometer apparatus invented by Wolfgang Paul [54]. This invention lead to the modern day Paul trap. The Paul trap is widely used in trapped ion quantum information processing.

Quantum information can be encoded in many different electronic states of a trapped ion. Consider the specific case of barium trapped ions. Information can be stored as an

optical qubit, such as is the case with Ba^+ by utilizing the $6\,S_{1/2} \rightarrow 5\,D_{5/2}$ transition, where one state is used in the $6\,S_{1/2}$ manifold and another state is used in the $5\,D_{5/2}$ manifold [64]. Information can also be stored entirely in the metastable $5\,d\ ^2D_{5/2}$ state [65]. The final encoding scheme is the ground state qubit or "hyperfine qubit", where information is stored in the clock transition of the $6\,S_{1/2}$ ground state. Using the clock transition for storing information is beneficial because the hyperfine states are not first-order sensitive to magnetic field fluctuations, but leakage can occur from off-resonant scattering to other hyperfine levels during two-photon transitions between the clock states [66]. The schemes that have been described here are commonly referred to as the optical, metastable, ground-state (OMG) architecture [47]. The metastable encoding architecture is easily realized with Ba^+ ions because of the $\sim$ 35 s lifetime of the $5\,d\ ^2D_{5/2}$ state. This is over an order of magnitude longer when compared with the metastable state liftimes in Yb^+ ($\sim$ 55 ms) [67] and Ca^+ ($\sim$ 1 s) [68].

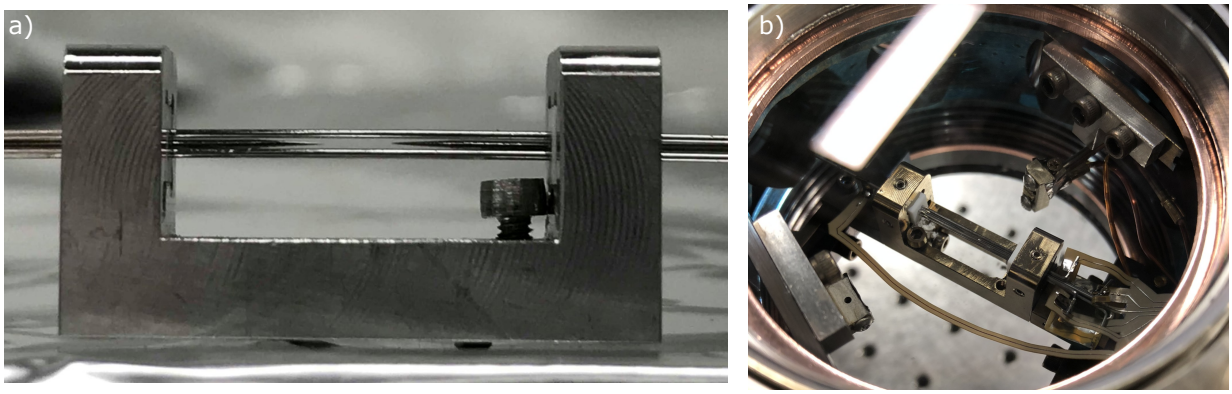


Figure 1.2: a) Image of a four-rod Paul trap which was made from tungsten rods for barium qudit experiments that was fabricated during my first year as a graduate student [49]. b) The trap is installed in an ultra-high vacuum chamber, which is the basis for the photoionization experiments described in Section 2. The trap electrodes are connected to a feed-through with a flexible printed circuit. The trap is loaded via laser ablation of a barium salt.

1.1.1 $^{133}Ba^+$ Atomic Structure

Barium trapped ions for quantum information processing has grown as a field in the last decade or so, spurred on by the record breaking experimental SPAM fidelities achieved with $^{133}Ba^+$ [69, 70]. Much of the work in this thesis is motivated by the goal of reliably trapping the $^{133}Ba^+$ isotope so that long chains of these ions can more easily be used for

quantum information processing experiments. The atomic structure for $^{133}Ba^{+}$ ($I = 1/2$) is presented in Fig. 1.3.

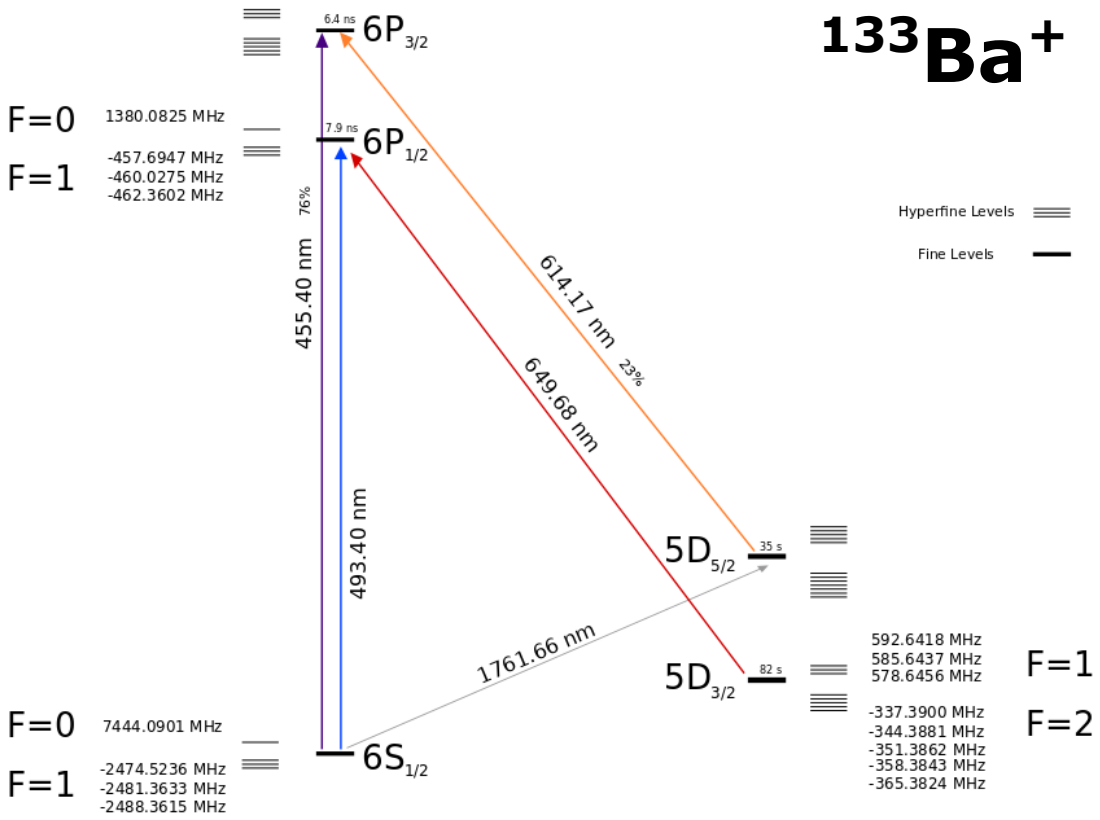


Figure 1.3: Atomic structure of $^{133}Ba^{+}$ with relevant transition wavelengths and branching ratios [71]. The Zeeman levels for the $6\,S_{1/2}$, $6\,P_{1/2}$, and $5\,D_{3/2}$ states are explicitly written assuming a ~ 5 Gauss magnetic field. The majority of the wavelengths are visible, which is advantageous from an optical engineering standpoint, making individual addressing of ions [72] and photoionic networking easier [73].

Barium has been successfully loaded for years into traps [74, 75], but in order to push trapped ion technology forward, every aspect of these machines must continue to grow to be more reliable; including the loading of long chains of barium ions. This is of particular importance when using room temperature vacuum systems where chain lifetimes are on the order of minutes [76]. Assuming ion chain lifetimes scale as $1/N$ [77], a chain of 20

ions, which is the target for the machine described in Section 4, would have an average lifetime of $\sim$ 13 minutes. If chains need to be reloaded roughly four times every hour in a room temperature UHV system, then it is important to minimize the time it takes to complete this process.

Barium is challenging to load into ion traps because it is a rather reactive element. In atmosphere, barium will react in a matter of minutes meaning metallic barium is not found in nature, and is commonly manufactured from $BaCl_2$, BaO, and $BaCO_3$. These salts and oxides have too high of a melting point to utilize conventional oven loading [78], so laser ablation is often used instead [78, 79, 80, 43, 81]. Conventional barium ovens have been employed in trapped ion experiments but have been shown to fail, likely due to oxidation, as is the case with the oven installed in Fig. 1.2 [43]. For this reason, photoionization methods and heat-treatment of ablation targets are investigated as possible avenues to increase the rate and consistency of ablation loading Ba^+ ions in the following chapters.

Chapter 2

Exploiting an Autoionizing Resonance to Trap Ba^+

There are many ways to load an ion trap, such as the use of ovens [82], laser ablation [83], magneto-optical traps [84, 85], and electron bombardment [86]. This is not an exhaustive list and there is no "right way" to load ions into a trap since it depends on the specifics of the experimental apparatus, but the main considerations are to maximize the likelihood of trapping, in the shortest time amount of time possible, while reducing the amount of atomic flux impingement on the surface and also reducing the chances of inadvertently electrically charging the trap. Ovens have an advantage in that they produce a relatively large amount of slow moving neutral atoms compared with laser ablation, but they can be relatively slow to switch on and off. Magneto-optical traps can also be used to capture a large cloud of neutral atoms, which will increase the probability of loading [85, 26], but there are technical challenges associated with cooling neutral barium because it requires many repumping transitions to be driven [84]. Electron bombardment is not isotope-selective, unless the source is entirely pure, so this was not considered for our work. For these reasons, the focus of this work is on maximizing the loading rate of barium to quickly generate long chains of ions for quantum information processing utilizing laser ablation. This chapter details the first demonstration of a two-step photoionization process ending in an autoionizing transition to trap Ba^+, drastically increasing the probability of trapping ions in a four-rod Paul trap.

2.1 Motivation and Context

As quantum computing technologies are scaled to include hundreds of trapped ions, representing many logical qubits, it will be necessary to make fundamental processes such as loading chains of trapped ions as efficient as possible. Furthermore, many of the leading trapped ion candidates, such as $^{133}Ba^+$ and $^{171}Yb^+$ ions, are rare isotopes that are either not found in nature at all (i.e. synthetic) or have relatively low natural abundance ($\sim 14\%$ for $^{171}Yb^+$ [87]), making these isotopes inherently more difficult to trap. In this respect, it is well motivated to examine all of the possible routes to increasing the consistency and rate at which trapped ions are loaded. We start first by carefully considering different plausible multi-step photoionization processes that can be used to generate Ba^+ from a neutral barium atom.

The technique known as resonance-enhanced multi-photon ionization (REMPI) is a standard process for loading an ion in an isotope-selective manner [88]. Generally, this involves a resonant "first step", which drives a transition in the neutral atom, before using a "second step" to drive one electron directly into the continuum. The first step in this process is the isotope-selective step, where the frequency of the laser light is varied up to ~ 1 GHz (in the case of barium) in order to excite only the target isotope [43]. For this first step, a laser with a linewidth $\Delta\nu \approx 100$ kHz is used to drive the transition in an effort to reduce off-resonant excitation of other isotopes.

Consider the possible first steps that could be used in ionizing neutral barium. This includes the use of a quadruple transition near 413 nm as well as a strong dipole transition at 554 nm [79]. One of the first demonstrations of a two-step isotope-selective photoionization process for loading barium even utilized a dipole transition at 791 nm [78]. These three possible first steps have been used to load crystals of hundreds and even thousands of trapped barium ions, but by examining the properties of the transitions it is clear that the 554 nm transition has a couple of advantages over the other first steps. These popular and demonstrated first steps are shown in Fig. 2.1.

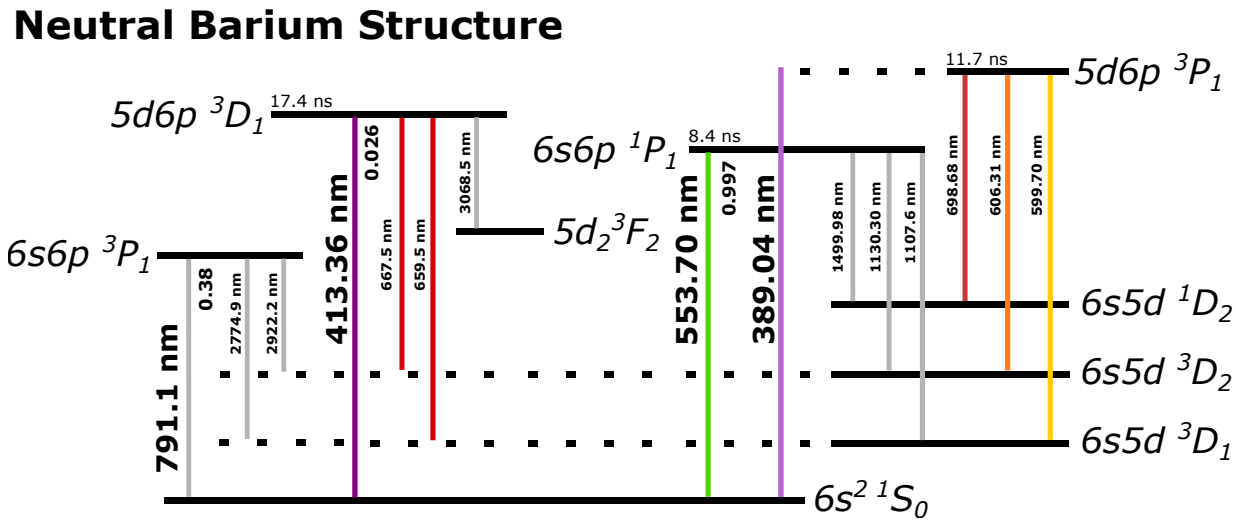


Figure 2.1: Relevant neutral barium atomic structure [89, 90, 91, 92]. The most commonly used steps for isotope-selective photoionization include 791 , 413, and 554 nm, with branching ratios of 0.38, 0.026, and 0.997 back down to the $6\,s^2\ {}^1S_0$ state, respectively. The $6\,s^2\ {}^1S_0 \rightarrow 5\,d\,6\,p\ {}^3P_1$ transition has yet to be demonstrated for trapping Ba^+ ions, but it could be used to isotope-selectively load with a two-photon process. Note that this is not an exhaustive structure diagram.

One advantage is that the 554 nm transition has the highest oscillator strength of any dipole transition in neutral barium. The oscillator strength of a transition is a quantity that defines the probability of absorption. This also means that significantly lower intensities are required to saturate the transition driven at 554 nm. The second advantage is that the branching ratio from the $6\,s\,6\,p\ {}^1P_1$ state to the $6\,s^2\ {}^1S_0$ ground state is almost unity (~ 0.997). The reason why the branching ratio could play an important part in increasing the probability of loading barium ions can be explained with a brief example.

Take the simple case of a neutral barium atom, produced from ablation, traveling at ≤ 636 m/s, which is the highest velocity atom that can be trapped in this four-rod system using the trap door method [43]. The time-of-flight of the atom in a typical ionization volume with a 70 μm beam diameter will be at least $70\,\mu m/636\,m\,s^{-1} \approx 110$ ns. Since the lifetime of the $6\,s\,6\,p\ {}^1P_1$ state is ~ 8.4 ns, this means that it is possible for this transition to be driven $\sim$ 13 times as the neutral atom flies through the photoionization beams. Considering the relatively weak branching ratios for the 791 and 413 nm transitions back down to the $6\,s^2\ {}^1S_0$ state, it is clearly advantageous to use 554 nm in order to avoid population loss without using repumping lasers. The $6\,s^2\ {}^1S_0 \rightarrow 6\,s\,6\,p\ {}^1P_1$ transition at 554 nm has the highest branching ratio of any transition from the $6\,s^2\ {}^1S_0$ state. The

parameters for these first step transitions are shown in Table 2.1.

λ (nm)	Intermediate State	Linewidth (MHz)	$6\,s^2\ {}^1S_0$ Branching Ratio
413	$5\,d\,6\,p\ {}^3D_1$	9.15 ± 0.26 [89]	0.026(13) [89]
554	$6\,s\,6\,p\ {}^1P_1$	19.02 ± 0.19 [89]	0.9966(0.2) [89]
791	$6\,s\,6\,p\ {}^3P_1$	0.820 ± 0.050 [93]	0.38 [94]

Table 2.1: Popular "first steps" for isotope-selective loading of Ba^+ and their characteristics. An ideal first step has a strong branching ratio back down to the ground state ($6\,s^2\ {}^1S_0$ in this case), in order to avoid population loss without repumping lasers. The linewidth of the first step must also be more narrow than the isotope shifts in neutral barium, since varying the frequency of the first step is how specific isotopes are selectively excited and subsequently ionized [43].

Now that the argument has been made for using 554 nm as the first step in this REMPI scheme, attention can be turned to the second step. In this situation, the goal is to search for a second step that accesses a large photoionization cross-section for barium (i.e. ending in an autoionizing transition). Luckily, these resonances in barium have already been measured decades ago [95, 96, 97]. Specifically, we will deal with the class of resonances that are accessed from the intermediate $6\,s\,6\,p\ {}^1P_1$ state.

Autoionizing resonances were first modeled by Ugo Fano in the 1960's, when he derived the solution for a discrete state interfering with a continuum of states [98]. This interference effect produces a lineshape in the measured photoionization cross-section now commonly referred to as "Fano" profiles. Theoretically, these resonances are the result of interactions between two or more valence electrons such that their wave-functions become correlated [99, 100]. Predicting the location and size of these resonances in the photoionization cross-section can be done so with multi-channel quantum defect theory analysis [101, 102, 103] or the eigenchannel R-matrix method [104, 105]. Many of these methods originated in nuclear physics in order to describe nuclear reactions and scattering events [106]. While theoretical calculations have been successful in the past, they usually rely on parameters obtained from experimentally measured photoionization cross-sections [96, 95, 97]. The results in this chapter are focused on exploiting already known resonances, so these theoretical frameworks are not outlined in detail as it is beyond the scope of this work.

A common description of the autoionizing process, in which a single valence electron from the outer shell is removed is provided below. Both valence electrons for neutral barium are assumed to start in the 6s orbital such that the total state of both electrons is

$6\,s^2\ {}^1S_0$. One electron is initially excited out of the 6s orbital with a laser at ~ 554 nm such that the total state evolves to $6\,s\,6\,p\ {}^1P_1$. In this situation the first valence electron has been excited to a 6p orbital, but the second electron still remains in its initial 6s orbital. The second step in the two-step autoionizing process is to use a laser near ~ 390 nm to excite both electrons to the $5\,d_{3/2}\,9\,d$ (J = 1) autoionizing state [107]. The wave-functions of both electrons briefly become correlated before the originally excited electron is ejected [100].

The probability of trapping an ion for a given ablation pulse is difficult to calculate because it depends on many empirical factors, but in most cases the probability of ionization (also the probability of trapping) is proportional to the photoionization cross-section $P_i \propto \sigma_P$ [108]. So by drastically scaling up the photoionization cross-section an experimentalist can similarly scale their probability of trapping. Past methods of trapping barium have always used a non-resonant photoionization scheme (*i.e.* not ending in an autoionizing transition), which ionizes a single electron directly into the continuum [43, 109]. This is in comparison to driving to an autoionizing state, which can provide up to or more than an order of magnitude increase in the photoionization cross-section [95, 96, 97]. While this is the first demonstration of loading Ba^+ using an autoionizing resonance, it should be noted that autoionizing resonances are commonly used in Sr^+ experiments [86, 110, 111].

Driving to an autoionizing transition from an intermediate state with photon energy $\hbar\omega$ yields a doubly excited quasi-bound state Ba^{**} where the sum of the energy of both the electrons is above the ionization threshold,

$$\hbar\omega + \mathrm{Ba}(6\,s\,6\,p\ {}^1P_1) \rightarrow \mathrm{Ba}^{**} \rightarrow \mathrm{Ba}^+ + e^- \tag{2.1}$$

In order to evaluate the effectiveness of using an autoionizing transition for loading Ba^+, two different photoionization schemes are compared. One scheme ends in an autoionizing transition and the other is non-resonant, meaning it does not access an autoionizing state in the ionization continuum. The first steps in each scheme are the same, so only the second step in the two-step process is compared. The first step uses 554 nm light to drive a strong dipole transition between the $6\,s^2\ {}^1S_0 \leftrightarrow 6\,s\,6\,p\ {}^1P_1$ states. The utilized second step for ionization is either 405 nm or ~ 390 nm light which drives either a non-resonant photoionization scheme with 405 nm light, or an autoionizing scheme with light near 390 nm. The 405 nm source is a cheap diode and it has been used by a multitude of academic groups since the cost is low [43, 109]. The 390 nm source is an extended cavity diode laser from MOGLabs, which when used in conjunction with 554 nm, gives access to the largest experimentally measured photoionization cross-section for barium [95]. There are an infinite number of possible photoionization schemes that can be used to trap barium. A

few of these popular two-step schemes are presented in Fig. 2.2. Both $^{137}Ba^{+}$ and $^{138}Ba^{+}$ ions were loaded in these experiments, but the majority of the experiments were done with the $^{138}Ba^{+}$ isotope because it is the most naturally abundant.

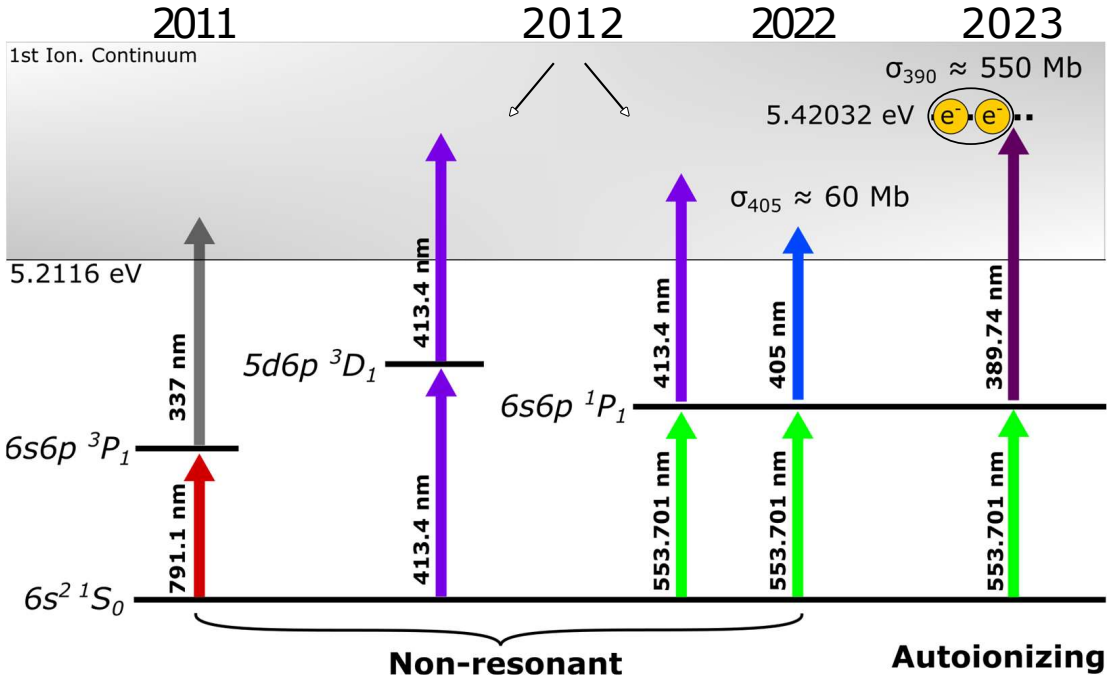


Figure 2.2: Previously demonstrated isotope-selective loading schemes of Ba^{+} have all been non-resonant, ending arbitrarily in the ionization continuum, generally dictated by the most convenient second step laser source that can be acquired [43, 44, 78, 79]. Use of a 554 and 390 nm laser is the only demonstrated isotope-selective loading scheme for trapping Ba^{+} that targets a specific autoionizing transition.

2.2 Experimental Overview

The following section is dedicated to documenting the experimental apparatus, nuances, and systemic process by which this study was conducted. The comparative study of the two different photoionization schemes were conducted on a four-rod Paul trap using IonControl software [112] in an isotope-selective manner [43]. The beam orientations are described as are the relevant details of the optics used for trapping. There is discussion between the two different second step lasers used for photoionization before ending the section with a description of the typical event sequence used for carrying out these experiments.

The loading of the ions was always done using laser ablation from a naturally abundant $BaCl_2$ target. The primary motivation for using a salt target is to gain experience using this type of atomic source since there is interest in future work involving the $^{133}Ba^+$ isotope, which can only be sourced as a salt. In order to confine the ions in the axial direction, V_{DC} = 7-9 volts are applied to end cap needles on the four-rod Paul trap. Radial confinement is achieved by applying $|V_{RF}| \approx 230$ volts to the rods of the trap, at $\Omega_{RF} = 2\pi \times 20.772$ MHz. The radio-frequency is delivered by a helical resonator, which acts as a filter and transformer [113]. The estimated secular radial frequencies for $\omega_{x,y}$ are $\approx 2\pi \times 1.2$ MHz and $2\pi \times 1.4$ MHz, respectively, and the axial frequency ω_z is $\approx 2\pi \times 100$ kHz. The dimensions of the four-rod Paul trap are depicted in Fig. 2.3a and Fig. 2.3b.

A total of three beam paths are used for conducting the ablation loading experiments, as shown in Fig. 2.3. One beam path is simply the nanosecond pulsed ablation laser at 532 nm. This light is focused onto the salt target containing $\sim$ 40 mg worth of material with a beam waist of $\sim$ 98 μm. The laser itself can deliver a maximum of 10 mJ of pulse energy, however, these experiments were conducted with $\sim$ 138 μJ unless otherwise stated. Ablation of the salt target sublimates the crystals on the surface, producing both charge-neutral atoms and ions, which travel $\sim$ 14.6 mm from the target to the center of the trapping region. The generated plume is relatively fast, with most probable velocities typically in the 1000-3000 m/s range [43], in comparison with ablation of metal targets.

Once the ablation pulse is triggered, trappable neutral atoms begin to arrive at the center of the trap roughly $\sim$ 42 μs later. At this point, these atoms travel through two beams, which are orientated orthogonal to each other in order to reduce the ionization volume so that only atoms near the radio-frequency null are photoionized. The first beam contains 554 nm to excite the $6\,s\,6\,p\ ^1P_1$ state in neutral barium, as well as subsequent frequencies at 493 and 650 nm to Doppler cool the ions once they are isotope-selectively generated. The combined beam is linearly polarized with a beam waist of $\sim$ 31, 35, 41 μm ($1/e^2$ radius), for the 493, 554, and 650 nm light, respectively. The laser powers are usually well above the saturation power with 110 ± 3, 15 ± 1, and 210 ± 6 μW for the 493, 554, and 650 nm beams, respectively.

The final beam path is again linearly polarized light, but it contains the second step photoionization beam as well as another repumping beam for ionized barium at 614 nm. The second step photoionization beam is either 405 nm or light near 390 nm, and these two frequencies are swapped depending on the specific photoionization scheme being investigated. If using 554 and $\sim$ 390 nm light to photoionize neutral barium, the 390 nm light can populate the $5\,d\ ^2D_{5/2}$ state in Ba^+ after a couple of seconds of exposure to the Doppler cooling beams. This is due to the fact that 390 nm is detuned by < 1 nm from the $6\,p\ ^2P_{1/2} \rightarrow 6\,d\ ^2D_{3/2}$ transition. This off-resonant pumping eventually leads to popu-

lation becoming stuck in the $5\,\mathrm{d}\,{}^2\mathrm{D}_{5/2}$ state. This can be avoided by either using 614 nm or simply shuttering the 390 nm beam shortly after the loading process is complete. The power carried by the second step photoionization beam is at least 150 μW, otherwise at lower powers the probability of trapping is quite low. The 614 nm has enough power to saturate the transition, typically carrying 7 ± 1 μW.

The 405 nm laser is a fiber pigtailed Cobolt focused to a beam of $\sim$ 35 μm. The 390 nm laser is a Littrow laser from MOGLabs with an estimated beam waist of $\sim$ 34 μm. These lasers were not frequency-locked during the course of this experiment. Given that the autoionizing transition is so broad, it was found not to be necessary to lock the laser in order to excite the transition. The 554 nm laser is frequency-doubled from 1107 nm using a cateye MOGLabs laser. This laser must be locked using a HighFinesse WS7 and the frequency can be tuned to determine which isotope to trap based on previous work [43]. In order to trap $^{138}\mathrm{Ba}^+$, the 554 nm laser is locked to 541.43304 THz. The 493 nm, 614 nm, and 650 nm lasers are locked to 607.42599 THz, 487.98967 THz, and 461.31212 THz, respectively using the WS7. Based on the frequency of the first step and previously measured photoionization cross-sections [107], where the autoionizing resonance occurs 5.42032 eV above the $6\,\mathrm{s}^2\,{}^1\mathrm{S}_0$ state, the theoretical optimal target frequency for the 390 nm laser is calculated to be $\nu_{390} = 769.19388$ THz. The linewidth of the autoionizing resonance far exceeds the mode-hop free tuning range of the 390 nm laser, so the loading rate as a function of frequency was not investigated. In practice, it is not necessary to use such a narrow linewidth laser as the one used to produce these results. The steps for ablation loading of the trap are outlined below:

1. Since the slowest process is to set the laser frequencies, which take on the order of seconds, this is the first step. The frequencies are set on the wavemeter for photoionizing and Doppler cooling the target barium isotope (in most cases this is $^{138}\mathrm{Ba}^+$).

2. The RF and DC trap voltages are turned on. This is done before the ablation pulse is triggered, since photoionization occurs within the trapping region.

3. The ablation laser fires a pulse at the salt target with photoionization taking place shortly afterwards, once the atomic plume has reached the center of the trap.

4. The 493 nm frequency is red-detuned 100-500 MHz, which is $5 - 25 \times \gamma_{493}$ the natural linewidth of the transition, before sweeping back up to a frequency near the atomic resonance. This is done in order to crystallize and Doppler cool any ions. This is done with 3-5 sweeps.

5. Counts from ions are monitored on a PMT and Steps 2-3 are repeated until an ion is trapped.

The light from both neutrals and ions is collected on a 0.26 NA objective constructed from Thorlabs lenses. The light can either be directed to a photo-multiplier tube (PMT, H10682-210) or a charge-coupled device (CCD, BFLY-PGE-05S2M-CS) using a flip mirror. An image of a chain of ions trapped with a single ablation pulse using the autoionizing scheme is shown in Fig. 2.3c.

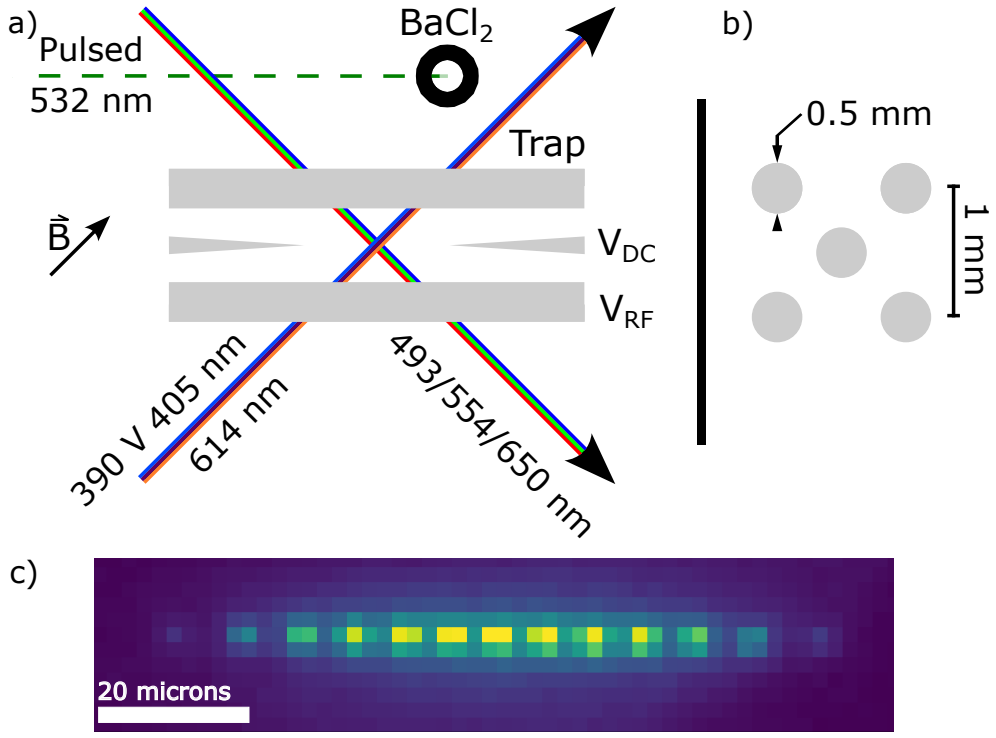


Figure 2.3: a) A top-down diagram of the four-rod trap and beam orientation used to trap Ba^+ in an isotope-selective manner. Either the 390 nm or the 405 nm (the second step photoionization laser) is used, but never both. The 554 nm laser is perpendicular to the $BaCl_2$ ablation target surface norm. The 532 nm ablation laser enters through the top viewport, focused down onto the ablation target with a beam waist of ~ 98 μm. The 493 and 650 nm beams are used for Doppler cooling and the 614 nm beam is used for repumping. More details on these beams can be found in the text. b) A cross-sectional view of the four-rod trap. Each rod is spaced ~ 1 mm from the others. c) A CCD image of a chain of thirteen $^{138}Ba^+$ ions trapped with a single ablation pulse using the autoionizing scheme.

2.3 Saturation of the Loading Rate

In order to compare the two different photoionization schemes discussed in the previous section, the loading rate (ions/pulse) is measured as a function of intensity in the second step photoionization beam. The intensity of the *first* step in the photoionization beam and the ablation pulse energy is kept constant throughout these experiments. Following the steps outlined in Section 2.2, a single ablation pulse is sent and the number of ions trapped is counted by imaging them on a CCD. A python script analyzes the images captured after a trapping attempt to count the number of ions, which is then later verified manually by viewing the image.

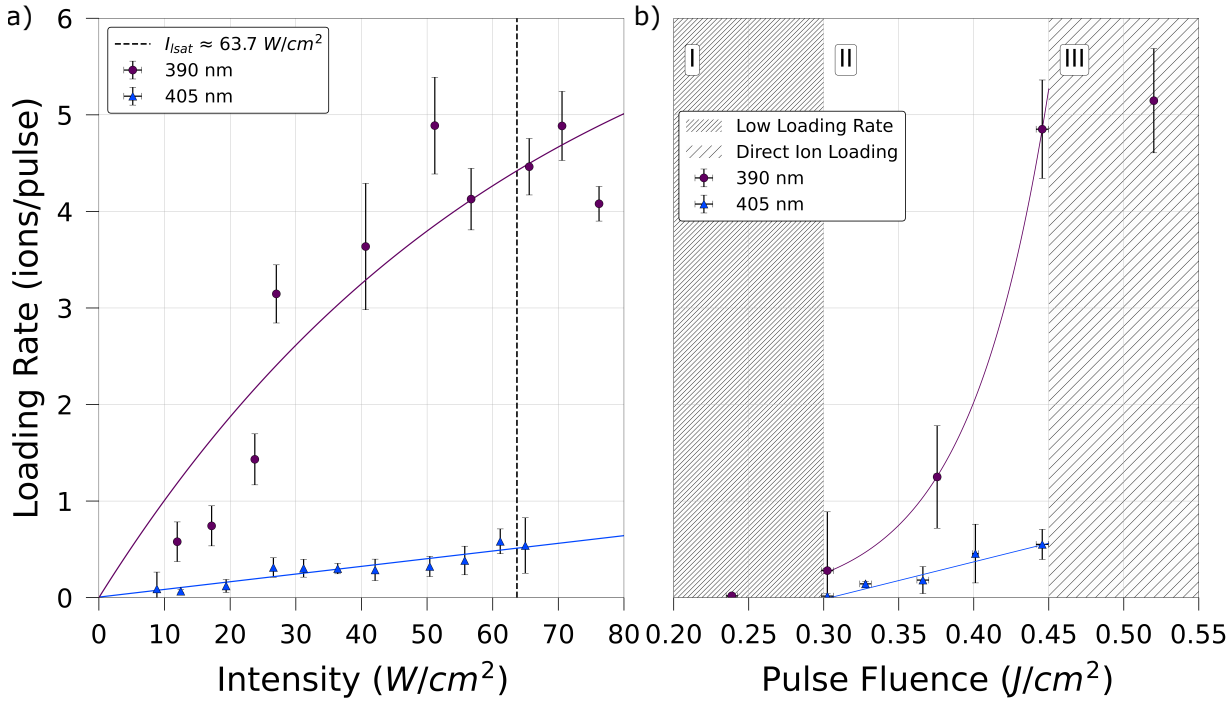


Figure 2.4: a) Loading rate as a function of intensity of the second step beam. The power was varied in order to change the intensity. The autoionizing scheme outperforms the non-resonant scheme for all intensities. The autoionizing scheme is fitted with an exponential dependence where $f(x) = a(1-e^{-b\cdot x})$, $a \approx 7.097$ ions/pulse and $b \approx 0.015\,\mathrm{cm}^2/\mathrm{W}$ are fitted constants and x is intensity in $\mathrm{W/cm}^2$ [96]. The fit $f(1/b) \approx 4.5$, agrees with the calculated loading saturation parameter $f(I_{sat}) \approx 4.4$. For this dataset the 390 nm laser frequency was measured to be $769.19326 \pm 0.006\,91$ THz. The error bars are the standard error of the mean. b) The loading rate as a function of ablation fluence, where the pulse energy was changed and not the beam size. The intensity of the second step photoionization beam was $\sim 53.5\,\mathrm{W\,cm}^{-2}$ for this dataset. The lines in this case are not fits, but act simply as visual guides.

The loading rates of $^{138}\mathrm{Ba}^+$ as a function of intensity in the second step laser is presented in Fig. 2.4a. What was found is that the autoionizing scheme out performs that of the non-resonant scheme at all measured intensities. At higher intensities, $30 - 80\,\mathrm{W/cm}^2$, the loading rate can be enhanced up to an order of magnitude. The calculated I_{sat} of the autoionizing transition is denoted by the dashed line, which agrees well with the linewidth of the resonance measured in previous work [95]. The calculation of the saturation intensity of the loading rate I_{sat} is straight forward and presented below, using the Fano linewidth

parameter $\Gamma \approx 60.4 \pm 1\,\mathrm{GHz}$ [95],

$$I_{sat} = \frac{\hbar\omega^3\Gamma}{4\pi c^2} \approx 63.7\,\mathrm{W\,cm^{-2}} \tag{2.2}$$

where c is the speed of light and $\omega = 2\pi \cdot 769.193\,\mathrm{THz}$ is the measured angular frequency of the light. This result is plotted in Fig. 2.4a, where the ablation laser pulse fluence was kept constant throughout the loading saturation experiments at $0.45 \pm 0.01\,\mathrm{J\,cm^{-2}}$.

It is assumed that below $10\,\mathrm{W\,cm^{-2}}$ the autoionizing and non-resonant photoionization schemes converge to a loading rate of zero as the intensities also approach zero. However, at high intensities, the loading rate appears to saturate when on resonance with the autoionizing transition. Based on the exponential function fit, saturation of the loading rate using the autoionizing transition is roughly 5 ions/pulse. The non-resonant scheme would require an intensity of $\sim 630\,\mathrm{W\,cm^{-2}}$ to achieve a similar loading rate, based on the linear fit. In this regime, if the second-step frequency is not resonant with an autoionizing transition, the photoionization cross-section is so small that the loading rate scales linearly with second-step laser intensity.

Ablation fluence experiments were also conducted similarly to the loading saturation experiments, except instead of varying the intensity of the second step photoionization beam, the ablation fluence was varied. This is depicted in Fig. 2.4b. showing the loading rate of the $^{138}Ba^{+}$ as a function of ablation laser fluence. The average intensity of the second step photoionization beams for the 405 and 390 nm beams were $\sim 53 \pm 3\,\mathrm{W\,cm^{-2}}$ and $\sim 66 \pm 2\,\mathrm{W\,cm^{-2}}$.

As the laser fluence increases, the amount of neutral atoms and ions produced also increases. Depending on the laser fluence, the ratio of neutral to ions produced fluctuates [43]. At low fluence ($< 0.3\,\mathrm{J\,cm^{-2}}$), the neutral-ion ratio is higher, however, fewer neutrals are produced which makes trapping more difficult. In this region, trapping was demonstrated with the autoionizing scheme on one occasion, but the non-resonant scheme was not able to trap after 100 attempts. This shows another advantage of using the autoionizing scheme, which is that ions can be loaded with a lower ablation fluence, which minimizes trap contamination. At a high fluence ($> 0.45\,\mathrm{J\,cm^{-2}}$), the loading rate does not significantly increase, but the isotope-selectivity decreases substantially because ions are loaded directly into the trap. The best ablation fluence range was found to be in the $0.3 - 0.45\,\mathrm{J\,cm^{-2}}$ range, where isotope-selectivity is not reduced, but neutral barium atoms are being consistently produced. These limits or regions may vary depending on the exact trap setup, but in general the same principle applies that there is an ideal operating ablation fluence region.

2.4 Loading Rate Comparison

2.4.1 $^{138}Ba^{+}$ Loading Rates

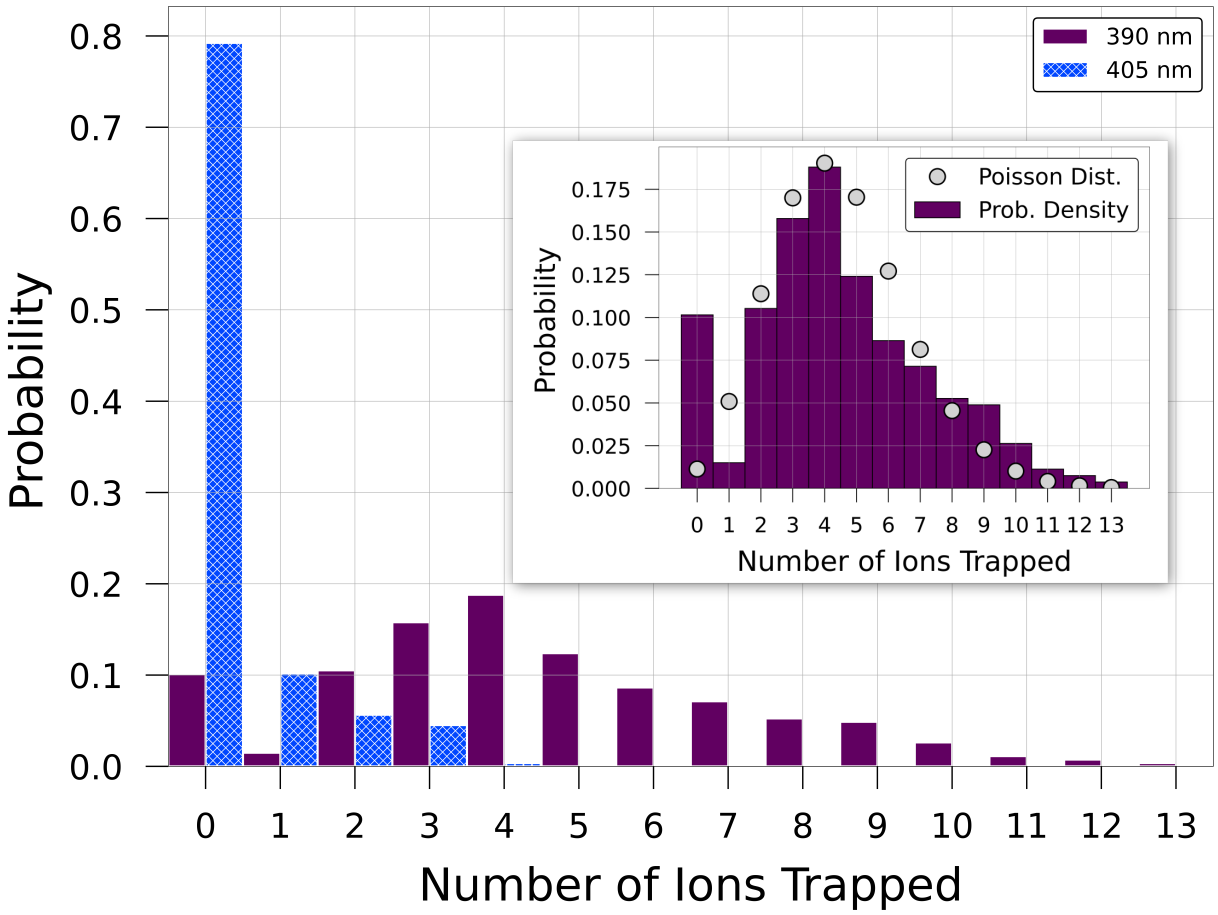


Figure 2.5: Histogram of the probability of trapping $^{138}Ba^{+}$ based on the two outlined photoionization schemes. The solid purple bars represent the probability of loading a specific number of ions using the autoionizing scheme and the hatched blue bars correspond to the non-resonant scheme. There were 265 and 266 trapping attempts for the non-resonant and autoionizing scheme, respectively. The inset shows a histogram of the probability of trapping $^{138}Ba^{+}$ using the autoionizing scheme, fitted with a Poisson distribution. The deviation from an ideal Poisson distribution is discussed in more detail in the text.

The loading rates of the two different photoionization schemes are compared in this section when the second step lasers have intensities $I > 50\,\mathrm{W\,cm^{-2}}$. The intensity is limited by the fiber-coupling of the 405 nm diode in this case, as the power emitted has been decreasing as the diode degrades. The ablation fluence is not changed over the course of the experiment, but set to $\sim 0.45\,\mathrm{J\,cm^{-2}}$.

Immediately, it is clear from Fig. 2.5 that the probability of trapping long chains is increased when using the autoionizing scheme. The median ions trapped per pulse using this scheme was 4 ions, compared with 0 ions when using the non-resonant scheme. In this dataset, the longest chain that was trapped in a single pulse was 13 $^{138}Ba^{+}$ ions using the autoionizing scheme, while the longest chain trapped using the non-resonant scheme was only 4 ions. The average loading rates using the resonant autoionizing scheme was $R_{390} = 4.48 \pm 2.75$ ions/pulse, while the non-resonant scheme had a loading rate of $R_{405} = 0.43 \pm 0.81$ ions/pulse.

The mismatch between the fitted Poisson distribution and data in the 2.5 inset could be due to a couple of factors such as inadequate locking of the 554 nm laser or mode-hopping of the 389 nm laser. If the wavemeter used to lock the 554 nm laser is not routinely calibrated (say each week), then it is possible for the reference point to drift. Mode-hopping of the 389 nm laser has also been observed, which could explain this variation as well.

During the loading experiments, fluorescence at 554 nm is recorded after each ablation laser pulse on a PMT, as a proxy for the amount of neutral barium atomic flux passing through the trapping region. On average, there were higher neutral atom flux for the experiments conducted with the autoionizing scheme than with the non-resonant scheme (a maximum of 39.5% higher fluorescence counts at 554 nm), which can be attributed to natural variations in the number of ablated atoms. The neutral atom flux is correlated to the probability of trapping [43], so a fair comparison between the ionization schemes must take this effect into consideration. Taking into account these considerations, the effective loading rate R'_{405} can be calculated,

$$\begin{aligned} R'_{405} &= R_{405} \times \frac{P_{390}}{P_{405}} \times \frac{\overline{N}_{390}}{\overline{N}_{405}} \\ &= 0.435\,\text{ions/pulse} \times \frac{1.17\,\text{mW}}{1.08\,\text{mW}} \times \frac{36.05\,\text{counts}}{25.84\,\text{counts}} \approx 0.657\,\text{ions/pulse} \end{aligned} \tag{2.3}$$

where $\overline{N}_{390}$ and $\overline{N}_{405}$ are the average neutral fluorescence counts during the 390 nm autoionizing and 405 nm non-resonant loading experiments respectively. Accounting for fluctuations in the neutral atom flux and slight differences in second step photoionization power, the loading rate with 405 nm would have been 0.657 ions/pulse, assuming that the

loading rate is proportional to both the 405 nm laser power and the neutral atom flux [43]. Thus, an estimated minimum increase in loading rate of $^{138}Ba^{+}$ using the autoionizing scheme is calculated to be a factor $R_{390}/R'_{405} \approx 6.8$. This compares well with the ratio of a previously measured photoionization cross-section, $\sigma'_{390}/\sigma'_{405} = 520 \pm 78\,\mathrm{Mb}/75\,\mathrm{Mb} \approx 6.93 \pm 1.04$ [95]. The uncorrected increase in loading rate is a factor $R_{390}/R_{405} = 4.477/0.435 \approx 10.3$.

The loading rate of an ion trap has been shown to be related to the photoionization cross-section by the trapping length l, number density N of the atoms in the intermediate level, power of the second step photoionization beam P_{390} and photon energy of the second step beam ϵ such that $\sigma = \frac{R\epsilon}{lNP_{390}}$ [114]. The intermediate level in this case with Ba^{+} would be the $6\,s\,6\,\mathrm{p}\,{}^{1}\mathrm{P}_{1}$ state. The number density was not calculated in this work because it would require extensive characterization of the imaging system, so the photoionization cross-section was not estimated.

2.4.2 $^{137}Ba^{+}$ Loading Rates

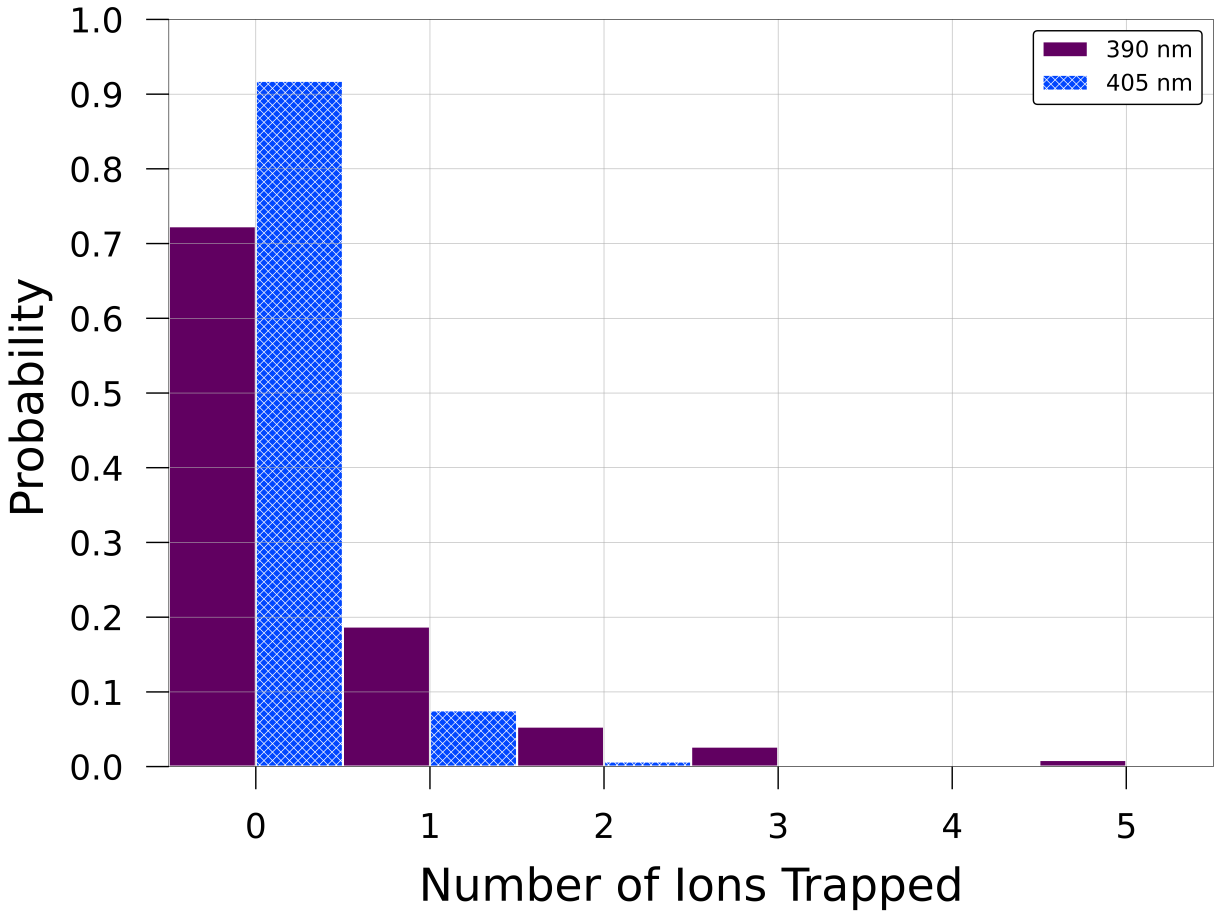


Figure 2.6: Histogram of the probability of trapping $^{137}Ba^{+}$ using the two different described isotope-selective loading schemes. The purple bars represent the use of 554 nm and 390 nm for the first and second steps, respectively. The blue bars represent the non-resonant scheme. The longest chain that was trapped in a single attempt was 5 ions using the autoionizing scheme, with an average of ~ 0.159 ions trapped per pulse. The longest chain trapped in a single attempt was 2 ions using the non-resonant scheme, with an average of ~ 0.026 ions trapped per pulse.

The $^{137}Ba^{+}$ isotope was trapped in a similar manner to how $^{138}Ba^{+}$ was trapped in the preceding Section 2.4.1. However, a key difference is that this odd isotope of barium requires the use of an electro-optical modulator (EOM) in order to efficiently Doppler

cool and trap chains of ions. More details on the exact frequencies used can be found in Brendan Bramman's Ph.D. thesis [115] and Pei Jiang Low's Ph.D. thesis [116]. The loading probability of the $^{137}Ba^{+}$ isotope for the autoionizing and non-resonant scheme are compared in Fig. 2.6.

Accounting for differences in the optical power and pulses per attempt, the increase in loading rate using the autoionizing scheme corresponds to a factor $r_{390}/r'_{405} \approx 6.4$ when loading the $^{137}Ba^{+}$ isotope. This is consistent with the factor of increase found when loading the $^{138}Ba^{+}$ isotope. There were 88 loading attempts with the autoionizing scheme and 269 loading attempts with the non-resonant scheme. This experiment differs from the previous ablation loading experiments in that there was almost always multiple ablation pulses per loading attempt, which was not the case when loading the $^{138}Ba^{+}$ isotope. Up to 10 ablation pulses were sent per loading attempt because the natural abundance of the $^{137}Ba^{+}$ isotope is only 11.2%. This specific two-step process could similarly be applied to load any of the barium isotopes.

2.5 Discussion and Outlook

Roughly a seven-fold increase in the loading rate of $^{138}Ba^{+}$ ion is demonstrated using the autoionizing scheme instead of a non-resonant scheme. The observed increase in the loading rates is consistent with the previously measured photoionization cross-sections [95, 96, 97]. The measured photoionization cross-section for ionizing into the continuum directly can range from 40-80 Mb, so in general this autoionizing scheme would outperform similarly against any non-resonant second step. The demonstrated autoionizing scheme accesses the largest photoionization resonance that has been experimentally measured for barium [95]. In this respective, there is not likely a more power efficient scheme for photoionization of barium, when considering two-step processes (a minimum of two-steps are necessary in order to isotope-selectively load). These autoionizing resonances have been shown to be able to ionize neutral atoms with almost 100% efficiency with ideal parameters [117].

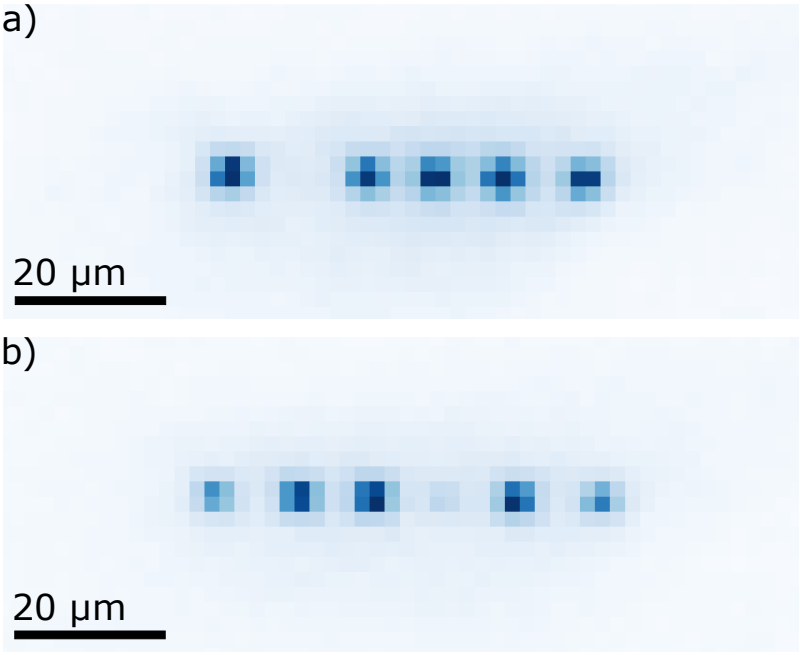


Figure 2.7: a) A CCD image showing the presence of a "dark" ion in a chain of $^{138}Ba^{+}$ ions. This is likely an odd isotope of barium. b) A CCD image showing the presence of a "dim" ion in a chain of $^{138}Ba^{+}$ ions. This is likely another even isotope of barium such as $^{136}Ba^{+}$ or $^{134}Ba^{+}$ since it is scattering photons at a lowering rate.

There is no theoretical reason why the autoionizing scheme would not be isotope-selective since it uses the exact same first step as in previous work [43], but a short study was done to ensure that this was in fact the case. A total of 478 $^{138}Ba^{+}$ ions were trapped in chains of at least two ions. The chains were analyzed for dark or dim ions in order to indicate the presence of other isotopes, with only 8 ions in 114 unique chains being other isotopes. This gives an isotope-selectivity of $\sim 98\%$, which is consistent with a previous study [43]. In order to increase isotope-selectivity for other isotopes such as $^{137}Ba^{+}$, the 554 nm power can be reduced since it was many times saturation during this study. This will reduce power broadening and increase the probability of loading only the desired isotope. Fig. 2.7 shows a chain of $^{138}Ba^{+}$ ions plagued by other isotopes that have inadvertently been trapped.

Barium, as all elements with multiple electrons, has a rich ionization structure. There are many plausible two-step processes that can be utilized to isotope-selectivity load barium. Previously measured autoionizing resonances accessible from the $6\,s\,6\,p\ ^{1}P_{1}$ state are shown in Table 2.2. In general, the longest wavelength that can be used to photoionize

Wavelength (nm)	Cross-section (Mb)	Autoion. State [107]	Energy (eV) [95]
380.75	≈ 300 [95]	$5\,d_{3/2}\,9\,d$ $(J=0)$	5.49549
384.33	≈ 290 [95]	$5\,d_{3/2}\,9\,d$ $(J=1)$	5.46516
389.74	550 [95], 520 ± 78 [97]	$5\,d_{5/2}\,8\,d$ $(J=1)$	5.42032
402.92	370 [95], 300 ± 45 [97]	$5\,d_{3/2}\,8\,d$ $(J=1)$	5.31629

Table 2.2: The $6\,s\,6\,p\ ^1P_1$ state is accessible from the $6\,s^2\ ^1S_0$ state. From the $6\,s\,6\,p\ ^1P_1$ state, there are a number of accessible autoionizing resonances as listed in the table. Other intermediate states listed in Table 2.1 can be used to drive different sets of autoionizing resonances, but the strongest measured photoionization cross-section of barium uses $6\,s\,6\,p\ ^1P_1$ as the intermediate state. The energies that are listed are referenced to the $6\,s^2\ ^1S_0$ ground state.

neutral barium from the $6\,s\,6\,p\ ^1P_1$ state is $\sim$ 417 nm, in a non-resonant manner. The longest autoionizing wavelength transition that can be used from the $6\,s\,6\,p\ ^1P_1$ state is $\sim$ 402.9 nm.

On a similar note, utilizing other first steps allows access to a slightly different ionization spectrum and other autoionizing transitions. Using 791 nm light to drive to the $6\,s\,6\,p\ ^3P_1$ intermediate state gives access to an autoionizing resonance with a measured cross-section of 102 ± 15 Mb when 340 nm is used as the second step [97]. Autoionizing resonances accessed from the $5\,d\,6\,p\ ^3D_1$ intermediate state (driven by 413 nm light) have also been relatively measured [118].

This experiment was motivated initially by the elusive and radioactive $^{133}Ba^+$ isotope that is only usually used in microgram amounts, however, there are applications for this photionization scheme in the quantum charged-coupled device architecture as well since a $^{138}Ba^+$ ion is loaded to sympathetically cool each $^{171}Yb^+$ ion [26] requiring a large number of ions to be loaded quickly. The $^{137}Ba^+$ isotope is of considerable interest as a metastable qubit [47] and with such low natural abundance, an experiment using $^{137}Ba^+$ could benefit from a more efficient photoionization scheme. Finally, if the efficiency of this photoionization scheme does not satisfy the experimentalist, other plausible routes to increasing the loading efficiency could be explored such as an optically activated oven [119], use of a magneto-optical trap, or even possibly investigating the dynamics of using shorter pulse width ablation lasers. Figure 2.8 shows a collection of ten ion chains all trapped in a single ablation pulse, demonstrating the power of utilizing an autoionizing resonance.



Figure 2.8: A CCD images of unique chains of $^{138}Ba^{+}$ ions trapped using the autoionizing scheme. Each chain of 10 ions was trapped with a single ablation pulse.

Chapter 3

Barium Chloride Ablation Targets

In this section a new method for fabricating and testing $BaCl_2$ ablation targets is presented and compared with a previous method [120]. Barium is more difficult to load into ion traps than other popular transitions metals like ytterbium because it is not found in nature as a free element. Loading ion traps with synthesized barium metal has been successful [75], however, accidental exposure of the pure metal in atmosphere during installation of the oven into the vacuum chamber can cause oxidation that can make it more difficult to use or fail all together. Working with barium salt ablation targets such as $BaCl_2$ has advantages in trapped ion experiments since it navigates the oxidation problem associated with barium. In addition, ablation loading is considerably faster than loading with an oven [82]. Finally, the synthetic isotope, $^{133}Ba^+$, can only be sourced as a salt such as $BaCl_2$ and $Ba(NO_3)_2$, so developing a recipe that maximizes the probability of loading as many Ba^+ ions as possible after each ablation pulse is of considerable interest [43, 81, 121, 122].

3.1 Motivation for Testing $BaCl_2$ Atomic Sources

Loading of barium $^{138}Ba^+$ has been previously demonstrated in surface traps before [75, 81], but loading of $^{133}Ba^+$ into a surface trap has not been reported in literature. Furthermore, in another project here at the University of Waterloo, $^{133}Ba^+$ was installed in a trapped ion experiment, but consistent loading was not successful and the isotope was only successfully trapped once. This study is motivated by this failure and the challenges that other groups have experienced when attempting to load Ba^+ ions from salt ablation targets [81].

Since the ^{133}Ba isotope is sourced as a radioactive salt, the amount of salt that can be used is limited by governing regulations. The Canadian Nuclear Safety Commission (CNSC) only allows work with up to $\sim$ 55.5 MBq with a Basic Level license [123]. The ^{133}Ba isotope has a half-life $t_{1/2} \approx 10.5$ years [81], which would mean that a maximum amount of salt that can be used a for a trapped ion experiment is roughly ~ 9 μg of $BaCl_2$ under this statute. Loading of an ion trap quickly and consistently with microgram quantities of *any* isotope is difficult and so far $^{133}Ba^+$ trapping has been reported by just a single academic group in recent years [70]. This is the only systematic study of microgram $BaCl_2$ ablation targets and a high-vacuum chamber was constructed with the sole purpose of testing different ablation targets.

The goal is to produce neutral fluorescence [45] from these ablated targets and evaluate the consistency and longevity of each ablation target type. The ablation targets are studied using characterization techniques such as scanning-electron microscopy (SEM) and energy dispersive x-ray spectroscopy (EDS) in an attempt to better understand the distribution of $BaCl_2$ on the surface of the ablation targets. The proprieties that are measured in this study are isotope-independent so the ^{138}Ba isotope is used in lieu of ^{133}Ba because ^{138}Ba is naturally abundant and nonradioactive.

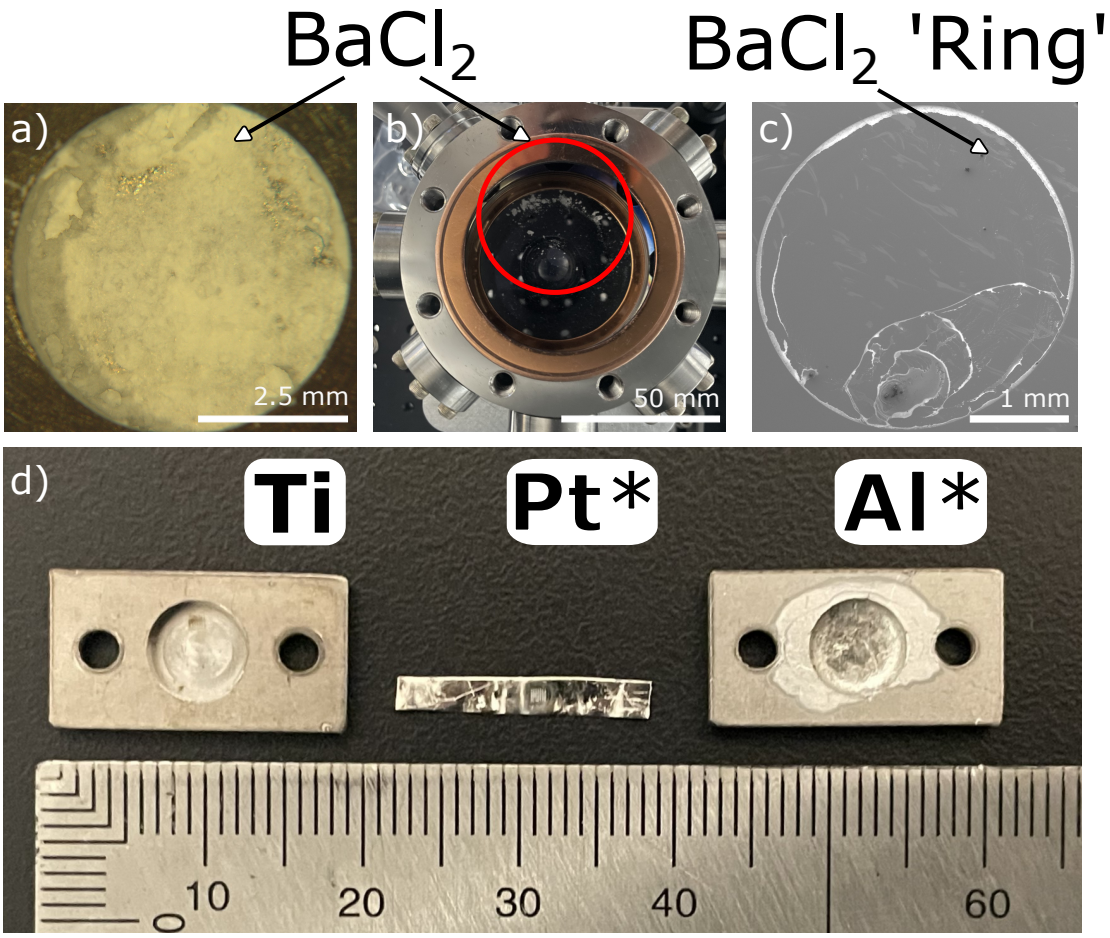


Figure 3.1: a) Macroscopic $BaCl_2$ ablation target in a titanium holder, containing $\sim$ 100 mg worth of salt. b) Residual $BaCl_2$ at the bottom of a high-vacuum testing chamber that has been fractured off of macroscopic targets after ablation. c) A ring of $BaCl_2$ containing $\sim$ 1-2 μg of the salt. d) Ablation targets with $\sim$ 5 μg of $BaCl_2$ on various heat-treated and non heat-treated substrates. Heat-treated ablation targets are denoted by an asterisk.

A significant challenge with ablating microgram quantities of salt is that often the ablation process itself removes the salt from the surface without sublimating the material. This will be referred to as "fracturing", where crystal fragments are broken or fractured off of the substrate due to the energetic ablation pulse. This is one barrier for creating efficient $BaCl_2$ ablation targets, which is highlighted in Fig. 3.1. In Fig. 3.1a, an image of a $BaCl_2$ ablation target is shown with $\sim$ 100 mg worth of salt. In Fig. 3.1b, $\sim$ 1 g worth of salt sits at the bottom of the high-vacuum chamber after thousands of ablation

pulses from multiple $BaCl_2$ targets. Fracturing is an issue for macroscopic $BaCl_2$ ablation targets ($\geq$ 0.1 mg of salt), as evident by Fig. 3.1, and we speculate that this is an issue for microgram $BaCl_2$ ablation targets ($\leq$ 10 μg of salt) as well.

Radioactive ^{133}Ba can be procured as $BaCl_2$ dissociated in a vial of weak acid [45]. In order to create an ablation target, the solution is deposited onto a substrate with a pipette one drop at a time, where the solution dries and leaves behind the salt in a 'ring' pattern. Consistent neutral barium production from *microgram* $BaCl_2$ ablation targets is hindered by the formation of these $BaCl_2$ rings. These rings form during the deposition process and causes the salt to be highly concentrated on the surface of the ablation target as pictured in Fig. 3.1c. The 'coffee ring effect' has been well studied and arises due to a difference in the evaporation rate at the edge of the drop compared with the rate at the center, which causes fluid flow [124, 125, 126].

One way to overcome these issues is to heat-treat $BaCl_2$ ablation targets. There are two recipes for manufacturing $BaCl_2$ ablation targets, which are detailed in the follow sections, but the underlying idea is that either the salt itself must be melted (MP = 960° C for $BaCl_2$), or the substrate on which the salt is deposited must be melted in order to adhere the $BaCl_2$ to the surface as well as redistribute the salt that has dried into a ring structure.

This thesis presents three different types of ablation targets, two of which are heat-treated. The first type is a platinum target, which is a essentially a strip of metal resembling a filament, in which a large amount of current has been ran through it such that the $BaCl_2$ melts on the surface of the platinum [120]. This is referred to as a Pt* ablation target. The second type of target is an aluminum target that has been heat-treated (using a stage) such that the aluminum lying below the $BaCl_2$ melts, but not the $BaCl_2$ itself. This is referred to as an Al* ablation target. The third type of target is a platinum target that has not been heat-treated referred to as the Pt ablation type target. In general, an asterisk denotes that an ablation target has been heat-treated.

Before and after ablation, $BaCl_2$ is mapped on the surface of the targets, allowing structural formations of the salt to be imaged and investigated. The uniformity of the ablation targets after heat-treatment is overwhelmingly increased and $BaCl_2$ 'rings' are entirely absent. The targets are then ablated and neutral barium fluorescence is captured from each manufactured target. The heat-treated targets, as indicated by the SEM and EDS images, are four times as likely to produce detectable ^{138}Ba atoms and when ^{138}Ba atoms are detected, they can be detected for at least three times as many ablation pulses when compared with the non heat-treated ablation targets.

3.2 Deposition of $BaCl_2$

Regardless of the specific ablation targets being fabricated, the process for depositing the $BaCl_2$ is the same. In these experiments, radioactive $BaCl_2$ is not used, but instead natural abundance $BaCl_2$ from Sigma-Aldrich (342920-10G). This is assumed to contain roughly $\sim 72\%$ ^{138}Ba [43], which is used as a proxy in these experiments for ^{133}Ba. Radioactive ^{133}Ba can be procured from the Eckert & Ziegler Group as $BaCl_2$ dissociated in a vial of weak hydrochloric acid (HCl). The amount of radioactivity in a vial of ^{133}Ba pictured in Fig 3.2 can be specified by the customer up to $\sim$ 185 MBq. For testing purposes and in order to comply with CNSC radiation limits ($\sim$ 55 MBq), the assumed vial concentration is $\sim$ 37 MBq, which is well within the regulatory statutes.

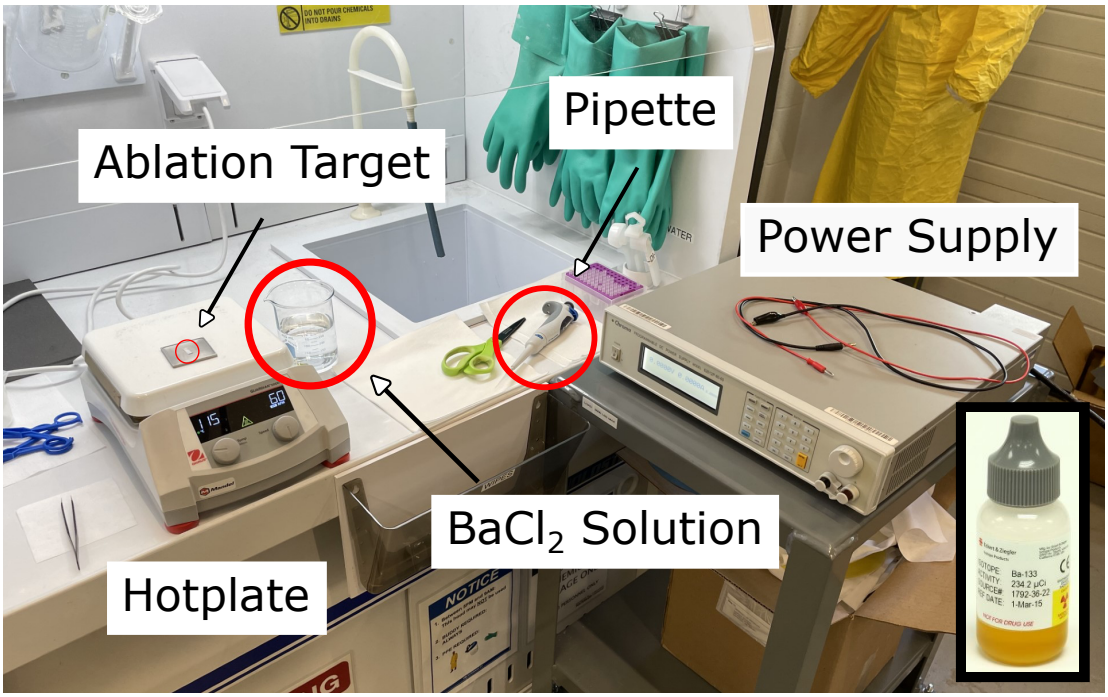


Figure 3.2: Setup for depositing $BaCl_2$ onto different substrates for ablation testing experiments. The $BaCl_2$ solution is deposited onto the ablation target with a pipette. The solution evaporated on the target, leaving behind the salt. A DC power supply is used to heat-treat the Pt* type targets after deposition. Absent from the picture is a scale used to create the $BaCl_2$ solution. The inset shows a vial of ^{133}Ba salt, however, natural abundance barium was used for testing ablation targets to prevent unnecessary radiation exposure.

The deposition presented in this section mirrors what would be done with radioactive

$BaCl_2$. Solutions of $BaCl_2$ are created with non-radioactive $BaCl_2$ and deionized water. Deionized water is used in lieu of HCl since the acid is incredibly weak with a molar concentration of 0.1M. In order to create accurate solution concentrations and deposit amounts of $BaCl_2$ that mimics what is in a vial of radioactive ^{133}Ba, the amount of salt must be calculated based on radioactivity.

The mass of ^{133}Ba salt (as $BaCl_2$) in a 37 MBq solution can be calculated from the half-life $t_{1/2}$ of ^{133}Ba, the rate at which particles are emitted A, the reaction rate constant λ, and Avogadro's number N_a [127]:

$$t_{1/2} = \frac{\ln(2)}{\lambda}, \tag{3.1}$$

$$A = \lambda N_a n. \tag{3.2}$$

The molar mass of radioactive $BaCl_2$ is assumed to be $\sim$ 203.8 g/mol [128] and the value of the other parameters used to find the number of moles n in the calculation are $t_{1/2} = 3.33 \times 10^8$ s, $A = 3.7 \times 10^7$ Bq, and $N_a = 6.022 \times 10^{23}$ mol^{-1}. This works out to be $\sim$ 6 μg of $BaCl_2$ in a radioactive vial with the assumed parameters. Non-radioactive $BaCl_2$ ablation targets are fabricated and tested with $\sim$ 5 μg of salt.

3.2.1 Deposition Process

The first step in the deposition process is to create solutions of dionized water and $BaCl_2$ which would have a similar salt concentration to a vial of ^{133}Ba. The salt concentration does not need to be exactly the same, but in order to faithfully replicate the process that would be done with ^{133}Ba, it is best to keep the salinity similar since the salinity dictates how many drops of the solution is necessary to deposit 5 μg of $BaCl_2$. A total of 25 drops are required to deposit 5 μg of salt with 10 μL drops from a solution with a salinity of 0.02 g/L. In these experiments, a liter of deionized water is combined with 20 mg of natural abundance $BaCl_2$. The exact volume of a radioactive vial (37 MBq) of ^{133}Ba can be specified by the buyer, but it is assumed the vial volume ranges from 0.25-0.5 mL with $\sim$ 5 μg of $BaCl_2$. Larger volumes have the potential downside of increased radiation exposure as the deposition process is assumed to take longer.

The dionized water and $BaCl_2$ are weighed separately on a digital scale with a 1 mg precision and then combined in a Griffin beaker. After the $BaCl_2$ and deionized water are combined, the solution is stirred with a glass rod until no more visible salt crystals remain. The dissociation process takes about five minutes. Once the solution of $BaCl_2$

is prepared, then attention can be paid to the substrates. The platinum foil for creating Pt and Pt* ablation targets is procured from Sigma-Aldrich (GF92036235). The foil is sonicated with acetone to remove any contamination and cut to size as shown in Fig. 3.1d. The Al ablation targets are cleaned in a similar manner.

After preparing the solution and cleaning the ablation targets, a hot plate is set to 115° C. At this temperature setting on the hot plate the evaporation rate of the solution is increased, but not so much so that it boils vigorously. It is unlikely that the sample itself has exceeded a temperature of 100° C. Boiling of the salt solution on the ablation targets will splatter $BaCl_2$, causing contamination as well as material loss. Evaporation of a 10 μL drop takes roughly a minute at this temperature. The ablation targets sit on a titanium plate ($\sim 50 \times 50$ mm^2) pictured in Fig. 3.2, which is placed on the hot plate in order to catch any spills that may occur.

A 10-100 μL PuroPET variable volume micropipette with 10 μL disposable pipette tips is used to deposit 10 μL of solution at a time. A single drop of solution is applied to the substrate until the desired amount of $BaCl_2$ has been applied. Care is taken not to burst the 10 μL droplet present on the substrate, since it can cause the solution to spill off the target. More details on the deposition can be find in Appendix A.1.

3.3 Heat-Treatment of Ablation Targets

There are two different heat-treatment methods presented in this section that adhere the barium salt to the given substrate, prevent crystal fracturing, and more uniformly distribute the salt. The first heat-treatment method follows the recipe [120], where a filament-like ablation target is restively heated above the melting point of $BaCl_2$. The second method utilizes an in-vacuum heating stage to re-melt an aluminum substrate with the barium salt deposited on the surface.

3.3.1 Resistive Melting of $BaCl_2$ on Platinum

After the deposition of $BaCl_2$ on the surface of the platinum strip, the ends of the strip are attached to a Chroma 62012P-80-60 programmable direct-current source with alligator clips. Roughly $I \approx 55$ A is ran through the platinum strip in constant current mode, which provides enough power to make the center of the filament glow bright orange, indicating incandescence, as depicted in Fig. 3.3 and melt the $BaCl_2$ on the surface. The melting of $BaCl_2$ occurs at ~ 962° C assuming standard atmospheric pressure and can be confirmed visually as the salt goes through a phase transition on the surface of the platinum.

The platinum strips are cut from a foil that is ~ 0.125 mm thick, but the width and length can change slightly depending on the exact cut. The width and length are not critical parameters and can be changed to meet other experimental criteria, but the current will then also have to be adjusted slightly in order to ensure that the sample can be resistively heated to the melting point of $BaCl_2$. Most platinum ablation targets are $\sim$ 10-20 mm in length and ~ 2 mm wide.

Initially, while fabricating these ablation targets, the resistive heating of platinum with $BaCl_2$ was done in high-vacuum to prevent oxidation, but that was deemed as an unnecessary precaution and all ablated samples were heated in atmosphere. Platinum will oxidize in atmosphere when heated to high temperatures, but not in any detrimental fashion, although this is not the case for all substrates. For example, titanium should not be heated to this high of a temperature in atmosphere as it can create thick oxide layers that flake off, which can remove deposited $BaCl_2$.

3.3.2 High-Vacuum Heating of Aluminium with $BaCl_2$

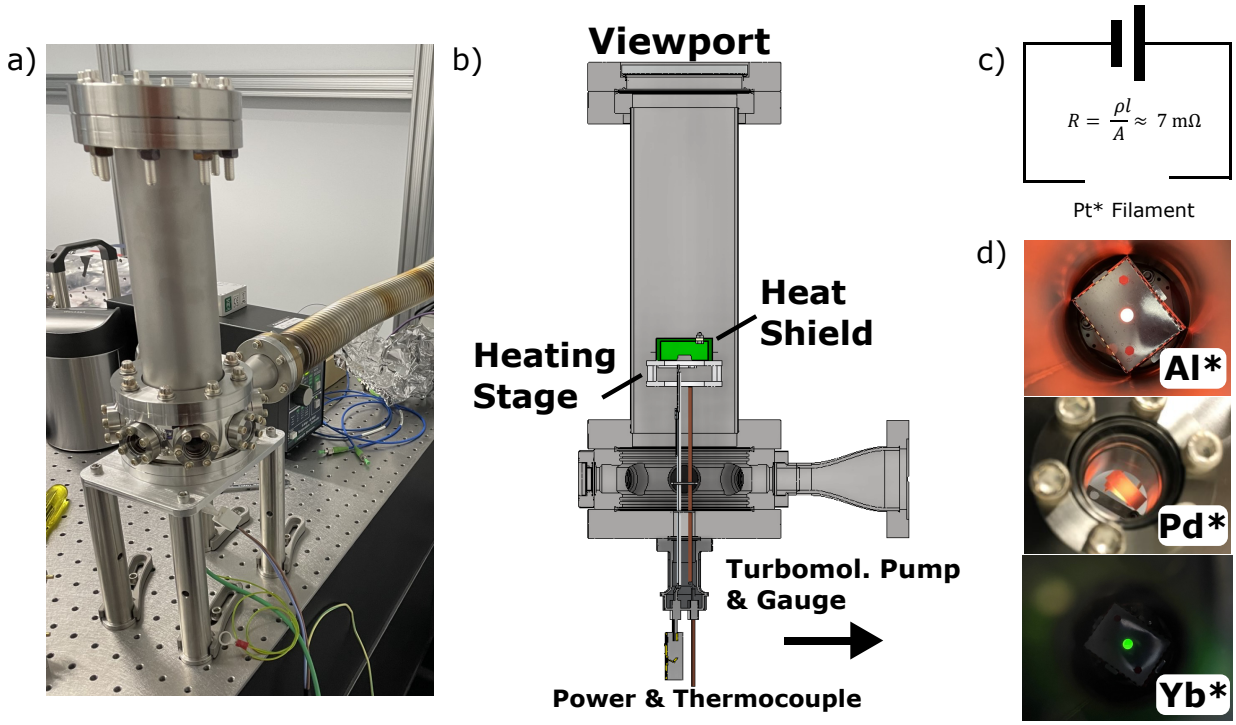


Figure 3.3: a) High-vacuum chamber ($< 1 \times 10^{-4}$ mbar) equipped with a 1 ″ heating stage capable of reaching 1200° C. b) Cross-sectional view of the high-vacuum chamber showing the internal components. The heat shield is always installed to prevent the viewport from exceeding ambient temperatures. c) Resistive heating diagram of a platinum ablation target ($\rho = 10.6 \times 10^{-8}$ Ω·m, $l \approx .0165$ m and $A \approx 0.000125 \times 0.002$ m^2) d) Examples of $BaCl_2$ being heated in high-vacuum with other elements such aluminum, palladium, and ytterbium. However, the focus of this work is on platinum and aluminum $BaCl_2$ targets.

Another method for fabricating $BaCl_2$ ablation targets is to melt the underlying substrate instead of the salt. The motivation for this type of target is to create a recipe for a "bulk" target, where the salt is dispersed throughout a volume, in comparison to the Pt/Pt* type targets where the salt is sitting on a surface. In this case, aluminum-$BaCl_2$ ablation targets are made by melting aluminum, at temperatures below the melting point of $BaCl_2$. The heat-treatment method uses a high-vacuum pyrolytic boron nitride heating stage from Tectra GmbH. This stage is able to reach 1200° C in principle, but samples placed on the stage can take up to an hour to come to equilibrium at this high of a temperature.

The high-vacuum environment is important in this process because the aluminum is initially melted in a machined titanium holder pictured in Fig. 3.1d before the $BaCl_2$ is deposited. Evacuation of the chamber is done with a turbo-molecular pump until the pressure reaches $< 1 \times 10^{-4}$ mbar. This ensures that the titanium ablation target holder does not oxidize and it improves the lifetime of the stage heating element.

Initially, the stage is brought to $\sim$ 300° C to remove H_2O and after five minutes the temperature is increased to 760° C to melt the aluminium (MP = 660° C) placed inside the titanium holder. Generally, 5-10 mg of aluminum foil from Kurt J. Lesker (FOILA24) is placed inside the holder and melted after a few minutes at 760° C. A controller with optimized PID parameters heats the stage within a couple of minutes to the desired temperature. The melting of aluminum under high-vacuum is difficult to estimate since it depends on the exact volume and shape of the pieces, so we find visual confirmation to be the best method. The sample is visible through a viewport, so the phase transition can be confirmed. The stage is switched off after the aluminum has melted and venting occurs once the stage temperature reaches $< 100°$ C. After this first heat-treatment, $BaCl_2$ is deposited onto the melted aluminum and then heated again to 760° C. A brief summary of the described steps are listed below.

1. Approximately 5-10 mg of aluminum foil is folded and placed inside the machined titanium ablation holders depicted in Fig. 3.1d.

2. The aluminum is melted into the holder in high-vacuum to prevent oxidation of the titanium holder.

3. $BaCl_2$ is deposited onto the melted aluminum as described in Section 3.2.

4. The ablation target is placed back on the high-vacuum heating stage and heated to $\sim$ 760° C in order to diffuse the salt.

3.4 Energy Dispersive X-Ray Spectroscopy

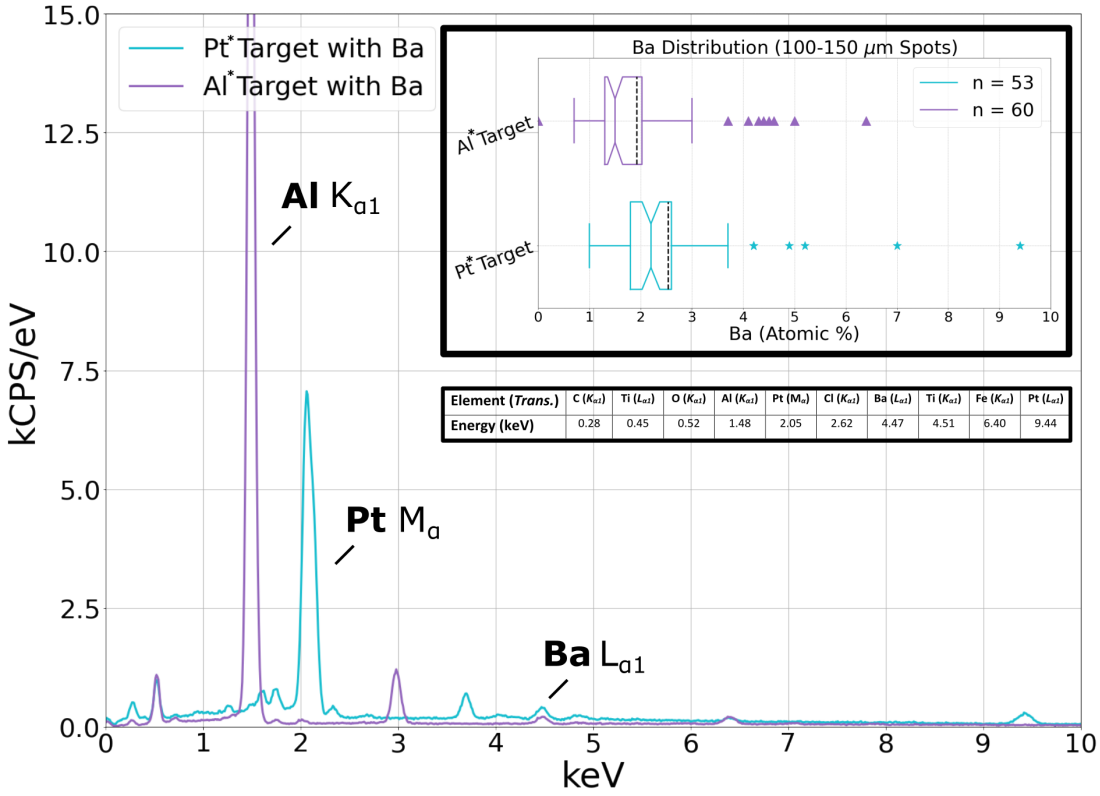


Figure 3.4: Overlaid energy spectrum of 5 μg Pt* and Al* ablation targets from EDS measurements. Each element has a unique spectrum and can be identified by prominent electronic transitions from outer shells to vacancies in inner shells such as the $K_{\alpha 1}$, M_{α}, or L_{α_1} lines. The spectrum allows confirmation of $BaCl_2$ and relative measurements of the atomic composition on the surface of the ablation target. The inset shows a systematic sampling of the amount of barium at n different spots on the ablation targets. This is a box plot, with the mean donated by the dashed line, the median denoted by the solid center line and outliers denoted by either triangles or stars depending on the dataset. These measurements were taken after deposition and heat-treatment, but before ablation.

EDS is a common technique for probing the elemental composition of the surface of a sample [129]. To the naked eye, 5 μg of $BaCl_2$ is not typically visible on the surface of the ablation targets. After fabrication and ablation of sample targets, EDS is used to confirm the presence of $BaCl_2$ on the surface and quantify the uniformity. An EDS detector is

usually part of an SEM. The basic process is to bombard the sample with an electron beam (from the SEM), which will subsequently remove electrons from the inner shells of the atoms. The vacancy of the inner shells will be filled by electrons decaying from outer shells, releasing discrete amounts of energy (on the order of keV) which creates a distinct spectrum for different elements as shown in Fig. 3.4. Resolution of EDS is on the order of 1 μm and the mapped areas are 100-150 μm corresponding to the spot size of the ablation laser focused on the ablation target. The sampled spots on the heat-treated Pt* and Al* ablation targets typically have 1-3% barium by weight on the surface, with an average of 2.5% and 1.9%. The coefficient of variation of the measured barium on the surface of the sampled spots for the Pt* and Al* targets are similar at 0.58 and 0.62, respectively. Using EDS after sample fabrication allows us to confirm the presence of $BaCl_2$ on the surface of the targets before ablation testing. A total of 53 and 60 spots on the Pt* and Al* ablation targets were sampled, respectively. Every sampled spot, save one, had measurable amounts of barium.

3.4.1 Post-Deposition Spectroscopy of $BaCl_2$ Ablation Targets

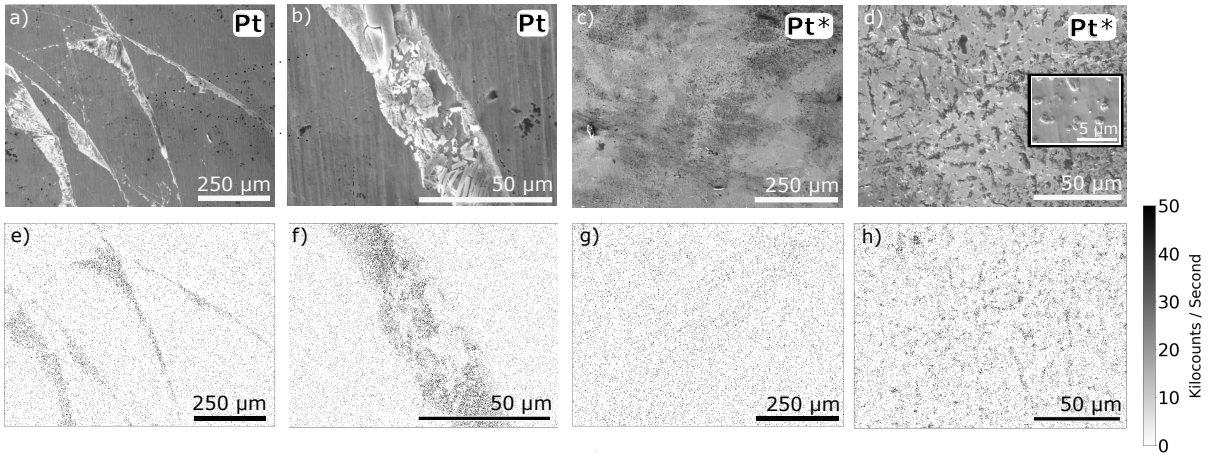


Figure 3.5: a) SEM image of a Pt ablation target with 5 μg of $BaCl_2$. The 'coffee ring effect' is evident on the surface, with multiple sections of the rings being visible. b) SEM image of a ring, with $BaCl_2$ crystals starting to fracture and separate on the surface of the platinum. c-d) SEM images of a Pt* ablation target with 5 μg of $BaCl_2$. The $BaCl_2$ crystals are spread out more uniformly on the surface. e-h) Corresponding EDS mappings of the SEM images confirming the presence of $BaCl_2$ on the surface.

Fig. 3.5 shows EDS measurements before ablation of Pt and Pt* targets. After melting the $BaCl_2$ on the surface, the Pt* targets are more uniform when compared with the Pt targets. The $BaCl_2$ crystals of the Pt* ablation targets are also spread out over the surface individually, limiting fracturing of large crystal chunks. While fracturing may still occur with Pt* ablation targets, it will be limited to only a few crystals at a time, increasing the lifetime of the ablation target and the total number of ablation pulses that produce measurable amounts of neutral barium atoms.

3.5 Neutral Fluorescence Collection

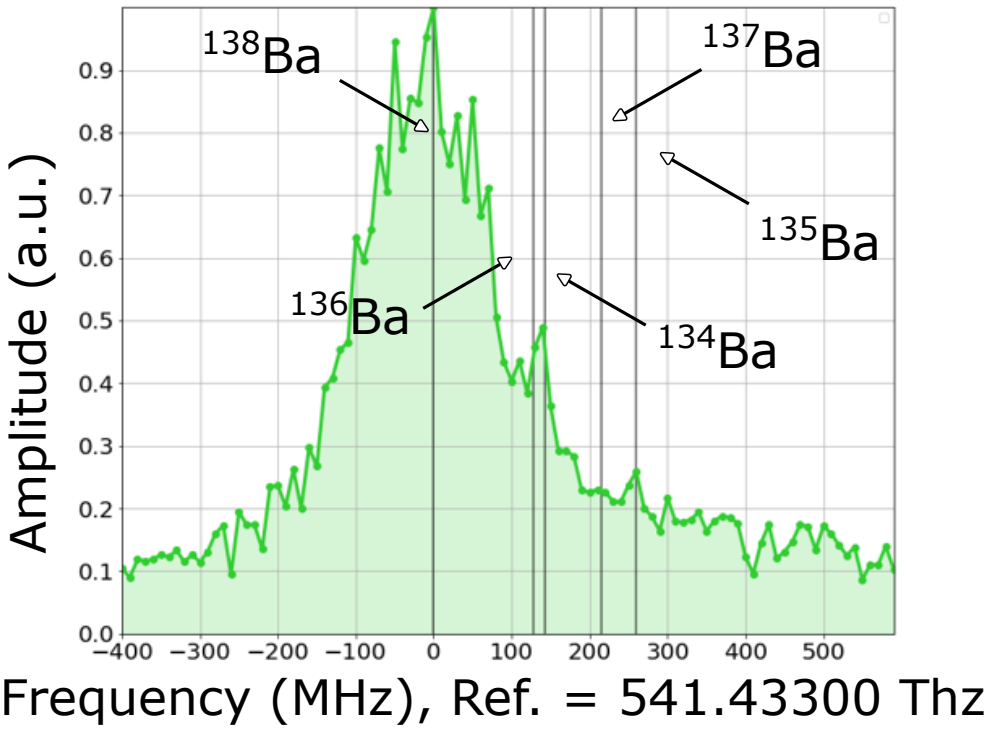


Figure 3.6: Counts collected on a PMT as a function of frequency after ablation of a macroscopic $BaCl_2$ target. The most abundant isotope is ^{138}Ba, but the presence of other isotopes is evident. Broadening of the $\sim$ 20 MHz linewidth is likely due to Doppler effects. While scanning the frequency, every other ablation pulse collects counts c_o at 541.433000 THz. The counts collected at a specific frequency c_ν are then normalized by the counts collected at 541.433000 THz such that c_ν/c_o.

Ablation targets are evaluated by collecting neutral fluorescence on a PMT from ^{138}Ba atoms, typically $\sim$ 10 μs after ablation with a collection window of $\sim$ 20 μs. This can be correlated to the probability of loading ions [43], so collection of many counts will indicate that an ablation target is reliable for trapping. Neutral counts from Pt, Pt*, and Al* ablation targets are collected at only two frequencies. The ideal frequency ν_{on} = 541.433000 THz and also an off-resonant frequency ν_{off} = 541.432000 THz. Comparison of the collected counts every-other ablation pulse allows criteria to be established that decides when a particular ablation spot is no longer yielding appreciable fluorescence. A running average of the counts collected after ablation when the laser frequency is set to ν_{on}, compared to when it is set to ν_{off} allows counts from ^{138}Ba atoms to be distinguished from background.

3.5.1 Experimental Setup

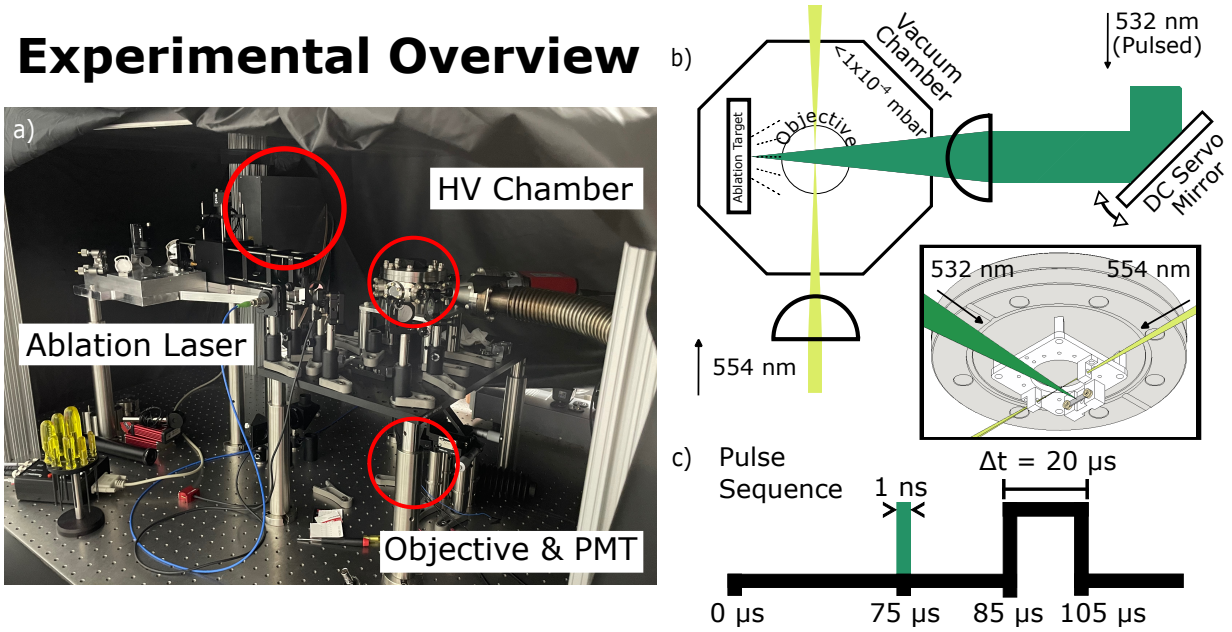


Figure 3.7: a) Experimental setup used to evaluate Pt, Pt*, and Al* ablation targets. There are two main beampaths, one for the 554 nm laser which drives a dipole-transition in neutral barium, and another beampath for the 532 nm ablation laser. The ablation targets are evaluated in high-vacuum. b) Diagram of the experimental setup, showing the beam orientations. The inset shows a CAD rendering of the ablation holder where the targets are mounted. c) Pulse sequence for collecting neutral fluorescence from the $BaCl_2$ ablation targets. The ablation pulse arrives ~ 75 μs after the start of the experiment. The pulse width is < 1 ns and photons are collected ~ 10 μs after the ablation pulse for 20 μs.

The experimental setup for collecting fluorescence is depicted in Fig. 3.7a. The ablation target is mounted 12 mm from the center of the chamber as shown in the inset of Fig. 3.7b. There are two beams that enter the high-vacuum chamber. The 554 nm laser drives the $6\,s^2\ {}^1S_0 \leftrightarrow 6\,s\,6\,p\ {}^1P_1$ transition and is positioned orthogonal to the surface norm of the ablation target to reduce Doppler broadening. Another green laser at 532 nm (Nd:YAG, nanosecond pulsed, solid-state) from RPMC Lasers Inc. (WEDGE-HB 532) is used to ablate the $BaCl_2$ targets. Typical pulses energies from the ablation laser are normally distributed around 0.303 mJ and the spot sizes are roughly ~ 300 μm in diameter as measured by an optical profilometer after ablation of a microfabricated gold wafer. This

gives a pulse fluence of $\sim 0.42 \pm 0.02$ J/cm^2, which is comparable to other trapped ion ablation experiments [43, 130]. Photons are collected on a Hamamatsu (H10682-210) PMT after every ablation pulse using a 1 inch diameter objective (NA = 0.26, WD = 43 mm). More information on the measurements of the ablation spot size can be found in Appendix A.1 with additional details of the optical infrastructure outlined in Appendix A.2.

The pulse sequence for the neutral fluorescence experiments is depicted in Fig. 3.7c. Given that the 2 kHz maximum repetition rate of the ablation laser is well below the timescale of any plasma-ion dynamics, only a single ablation pulse is sent at a time. The 554 nm laser is locked with a HighFinesse wavemeter (WS8-2), which takes roughly one second. The frequency is detuned 1 GHz off-resonance every other pulse as mentioned in Section 3.5. This allows background counts to be compared with counts collected from ^{138}Ba atoms. The ablation test chamber is from Kimball Physics (53-180000), which is the same chamber used in barium ablation experiments of a four-rod. The collection objective is also identical, which allows counts to be correlated to loading rates [43].

3.5.2 Spot Lifetimes of 5 μg $BaCl_2$ Ablation Targets

After fabrication and characterization of the Pt, Pt*, and Al* targets, the samples are installed in the high-vacuum test chamber and ablated. The center of the targets are scanned systematically, eventually forming a grid as shown in Fig. 3.8. Each spot is ablated until counts from neutral atoms are not distinguishable from background counts being produced before moving onto the next spot. The spots are spaced ~ 150 μm apart to ensure that no residual $BaCl_2$ is left in between each ablation spot. The ablation beam is moved using a motorized mirror mount from Thorlabs (KS1-Z8). The more neutral fluorescence produced from a particular spot, the longer the spot lifetime and the higher probability of trapping.

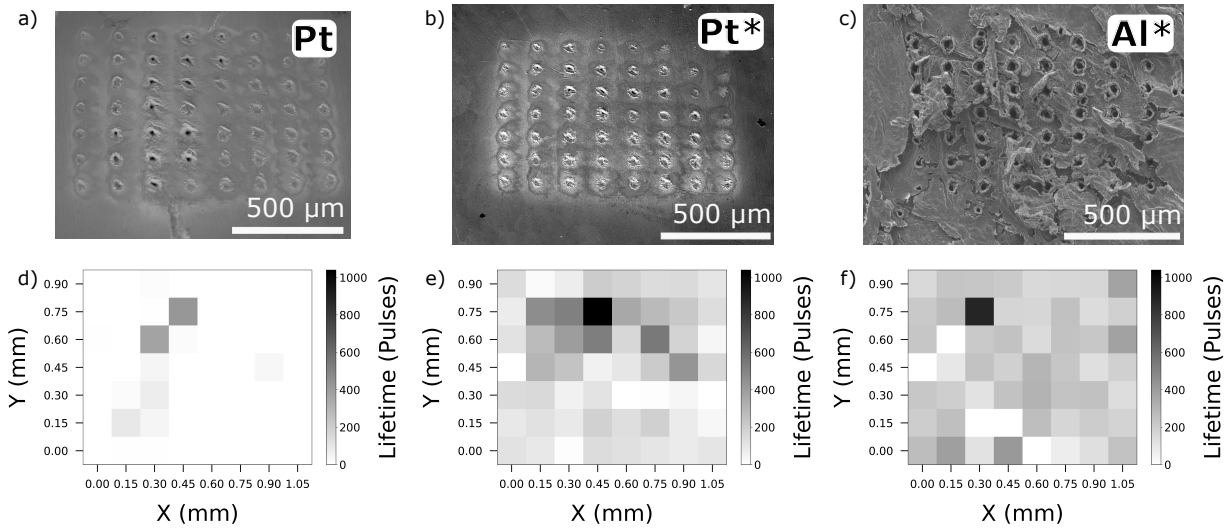


Figure 3.8: a) SEM image of 56 ablation spots on a Pt target. A section of a $BaCl_2$ ring is evident at the bottom of the image, traveling primarily through the third column. A mere 17/56 ablation spots on this target produced measurable neutral fluorescence meeting the σ_1 criteria. This was the best performing non heat-treated ablation target. b) SEM image of a heat-treated Pt* ablation target, with 55/56 ablation spots producing enough neutral fluorescence to meet the σ_1 criteria. c) SEM image of a heat-treated Al* ablation target with 51/56 spots producing enough neutral fluorescence to meet the σ_1 criteria. d-f) Corresponding heatmaps of the ablation spots, clearly showing enhanced longevity and uniformity with the heat-treated targets. Lifetime is measured by the number of ablation pulses at each spot before counts on-resonant cannot be distinguished from counts off-resonance according to the criteria in Eq. 3.3.

The lifetime of an ablation spot can be calculated a number of different ways, but given the stochastic nature of laser-ablation, a running average of the last 50 ablation pulses are used to determine if a spot is 'dead' (i.e. counts collected while the 554 nm laser is on-resonance cannot be distinguished from counts collected while the 554 nm laser is off-resonance). This means that each spot is ablated at least 50 times. Of the minimum 50 ablation pulses at each spot, 25 pulses are on-resonance and 25 pulses are off-resonance. The running average of the last 25 pulses on-resonance c_R and 25 off-resonance c_O are used to calculate whether there is appreciable ^{138}Ba neutral atoms being produced (50 total pulses N). The script is terminated if the counts collected on-resonance fall within $n = 1$ one standard deviation σ_1 or $n = 2$ standard deviations σ_2 of the background counts,

$$c_R \leq c_O + \sigma_n \tag{3.3}$$

Typically, the standard deviation of the 554 nm laser frequency is < 2 MHz over the course of the experiments. The saturation parameter is generally $s > 100$ for driving the $6\,\mathrm{s}^2\ {}^1\mathrm{S}_0 \leftrightarrow 6\,s\,6\,\mathrm{p}\ {}^1\mathrm{P}_1$ transition.

Target	c_1 (Pulses)	σ_1 Criteria	c_2 (Pulses)	σ_2 Criteria
Pt 5 μg	36	43 / 79$^\dagger \approx 0.54$	32	10 / 79$^\dagger \approx 0.13$
Pt* 5 μg	158	142 / 168 ≈ 0.85	91	95 / 168 ≈ 0.57
Al* 5 μg	184	134 / 175 ≈ 0.77	123	93 / 175 ≈ 0.53

†: Only 79/448 total spots from the Pt ablation targets hit a $BaCl_2$ ring, so only these ablation spots are used in these average lifetime calculations. Otherwise only $43/448 \approx 0.10$ spots would satisfy the σ_1 criteria and $10/448 \approx 0.02$ spots would satisfy the σ_2 criteria.

Table 3.1: Mean lifetime c_1 of all ablation spots on each target type that satisfies the σ_1 criteria in Section 3.5.2. The Pt* and Al* ablation targets have a uniform distribution of $BaCl_2$ on the surface so all spots on these targets are considered in the average lifetime calculations. Mean lifetime c_2 of only the spots that produced enough neutral counts to satisfy the σ_2 criteria.

Three Pt* and Al* ablation targets were tested. Four Pt type ablation targets were tested. A minimum of 55 ablation spots were sampled from each of these targets. The Pt* and Al* targets significantly out performed the Pt ablation targets, as shown by the number of spots that met the σ_1 and σ_2 criteria in Table 3.1. Considering the σ_2 criteria, the fraction of spots that produced significant neutral fluorescence is roughly a factor of ~ 4 higher when comparing the heat-treated targets against the non heat-treated targets. Using the same criteria, the heat-treated targets lasted at least a factor of ~ 3 longer than the non heat-treated targets. If all of the ablation spots on the non heat-treated Pt targets are considered ($10/448 \approx 0.02$ spots meet the σ_2 criteria), then the fraction of spots that produce significant neutral fluorescence on the heat-treated targets is roughly two orders of magnitude higher (a factor of ~ 24) then the fraction of spots that produce neutral fluorescence on the non heat-treated targets. The difficulty with ablating microgram salt targets that have not been heat-treated is that the salt is hard to find to begin with, and when it is found, often times it will be ablated off in just a few pulses. These results are consistent with the increase in uniformity evident by the EDS and SEM images.

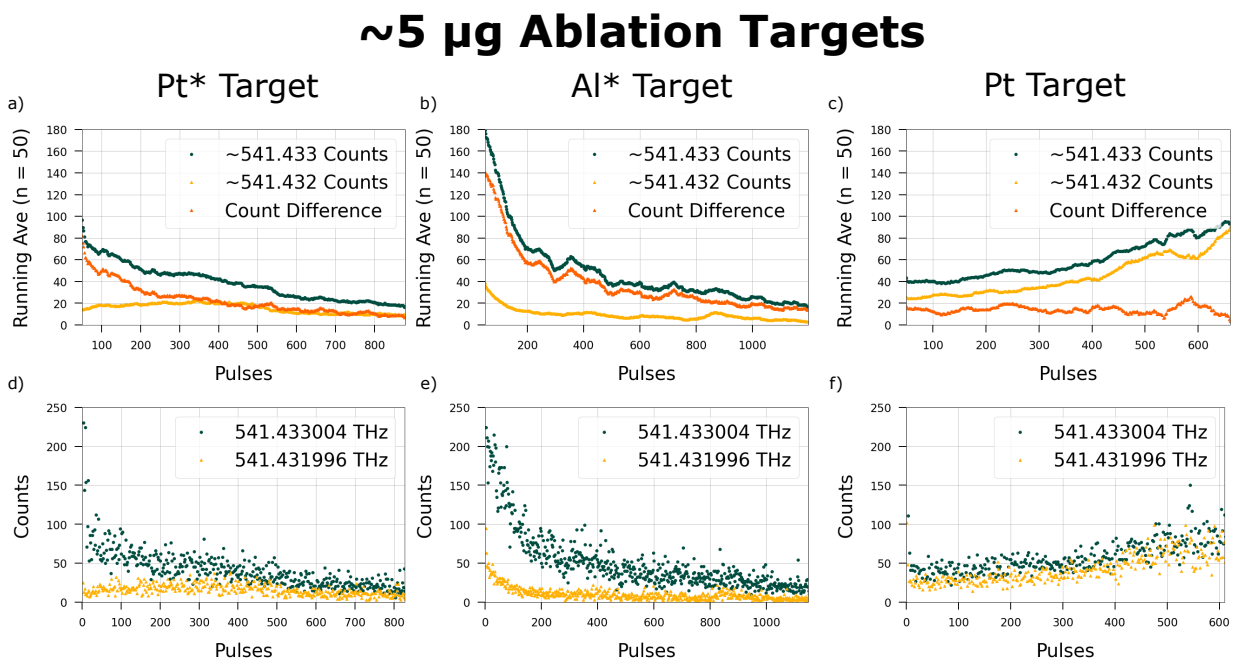


Figure 3.9: a-c) The best performing spots of the Pt*, Al*, and Pt type ablation targets. Green circles correspond to when the 554 nm laser is on-resonance with the $6\,s^2\ {}^1S_0 \leftrightarrow 6\,s\,6\,p\ {}^1P_1$ transition of ^{138}Ba. Gold triangles correspond to counts collected after the ablation pulse when the 554 nm laser was tuned off-resonance. The orange triangles are the difference between the running averages. The difference in collected counts when the 554 nm is tuned on-resonance is clearly visible when ablating the heat-treated targets. d-f) Neutral counts collected from the best performing spots after each ablation pulse.

Ablation spot lifetime graphs are presented in Fig. 3.9. These are the best performing ablation spots from each type of tested target, which reinforce the findings in Section 3.5.2. For the Pt* and Al* type ablation targets there is a clear distinction in the on-resonance counts and the off-resonance counts shot-to-shot, for at least a few hundred pulses. This is in contrast to Fig. 3.9f, where the counts on-resonance are not easily distinguishable above the background counts for the duration of the entire pulse sequence. Likely in the case of the Pt type targets, the majority of the salt is removed after a couple of ablation pulses. These spot lifetime plots can vary depending on the presence of $BaCl_2$ on the surface of the target, but the majority of the spots on the heat-treated ablation targets produce counts on-resonance that are immediately obvious to be above the background. The targets presented here had ≤ 5 μg of $BaCl_2$ over the entire surface ($\sim 20\,mm^2$).

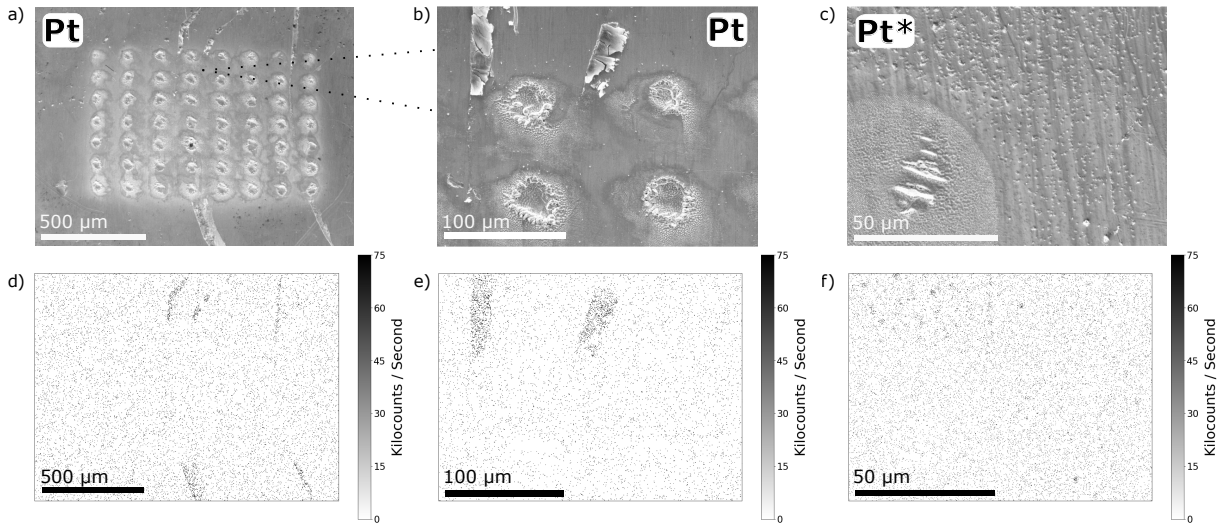


Figure 3.10: a-b) SEM images after ablation of a $BaCl_2$ ring. An estimated 14 spots hit this ring, but only a single spot produced enough neutral fluorescence satisfy the σ_1 criteria. c) SEM image of an ablation spot and individual $BaCl_2$ crystals on a heat-treated Pt* target. d-f) Corresponding EDS images of the above SEM scans, confirming the removal of $BaCl_2$ after ablation.

The targets were characterized using SEM and EDS after ablation, as shown in Fig. 3.10. These images show that the $BaCl_2$ is in fact being removed after ablation and that no detectable amount of barium remains on the surface where the ablation beam was focused, further validating the criteria outlined by Eq. 3.3. In the case of the Pt target in Fig. 3.10a and Fig. 3.10b, the rings have been removed, but only a single ablation spot produced a detectable amount of neutral barium atoms.

3.6 Testing Macroscopic Ablation Targets

In this section, macroscopic ablation targets (> 100 μg $BaCl_2$) are tested and neutral fluorescence is collected in the same manner as described for the 5 μg ablation targets. These targets are tested as a potential atomic source for ablation loading of ^{137}Ba and ^{138}Ba, as well as other isotopes, for use with surface traps. The advantage of using a $BaCl_2$ ablation target for loading ^{137}Ba and ^{138}Ba is that it is faster than conventional ovens and eliminates any risk of oxidation associated with metallic barium atomic sources. These macroscopic target tests were originally motivated by trap contamination found on a

surface trap after ablation loading attempts. The surface trap was installed in an ultra-high vacuum (UHV) system for base pressure and ablation testing. A non heat-treated natural abundance $BaCl_2$ target was ablated and neutral fluorescence from ^{138}Ba was collected above the trap. $BaCl_2$ crystals were discovered on the surface of this surface trap after it was removed, sparking a brief investigation into the the potential for contaminates ($BaCl_2$ crystals in this case) to accumulate on the surface of the trap. In order to investigate if heat treatment could play a role in eliminating contamination, macroscopic $BaCl_2$ ablation targets were fabricated with ~ 0.2, 2, and > 20 mg worth of material in the same manner as previously described in Section 3.

3.6.1 Trap Contamination

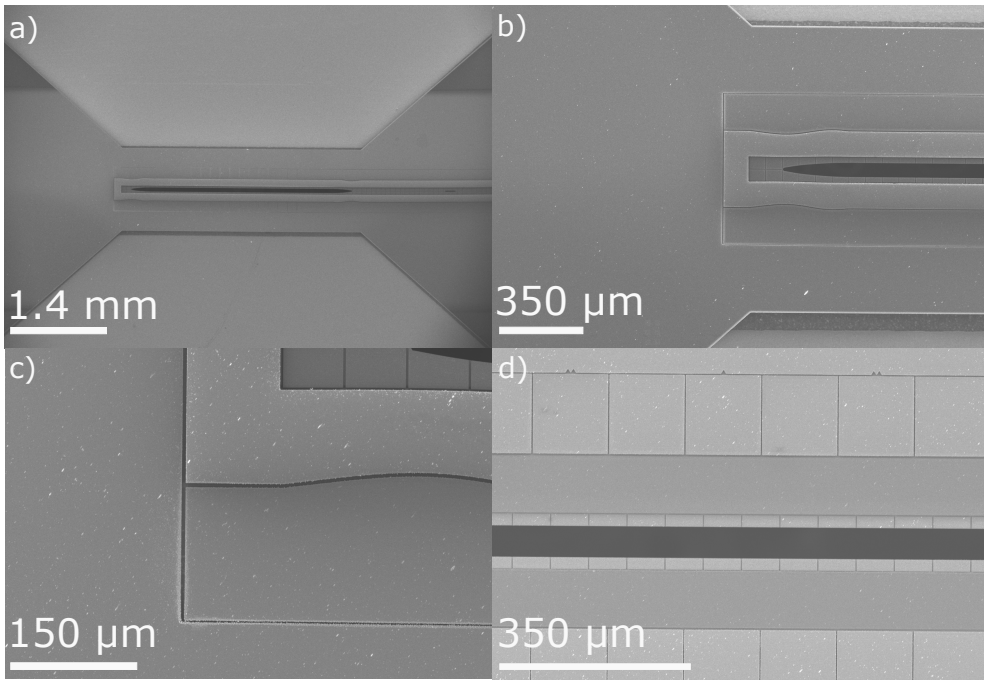


Figure 3.11: a-d) SEM images of a chip trap from Sandia National Laboratories [46] with $BaCl_2$ contaminating the surface after $>$ 50,000 ablation pulses. The ablation target was placed $\sim$ 15 mm away from the surface of the trap in an ultra-high vacuum chamber. It is unlikely that heat-treatment of ablation targets will eliminate contamination entirely. Thanks to Dr. Akbar Jahangiri Jozani for the taking these SEM images.

Trapping attempts were conducted with a defected test trap from Sandia National Laboratories [46] and subsequent contamination was found after the defected trap was removed from the UHV chamber ($\sim 4.4 \times 10^{-11}$ mbar). In contrast to the testing in previous sections utilizing ~ 5 μg of $BaCl_2$, an ablation target was installed with ~ 40 mg worth of salt about 15 mm away from the center of the trap. Neutral fluorescence was collected from ^{138}Ba as the target was ablated with similar fluences discussed in previous sections, confirming the presence of neutral barium atoms at the trapping region via fluorescence based measurements.

Trap contamination was found and imaged using an SEM, as shown in Fig. 3.11. It is unlikely that this contamination would cause shorting of electrodes since $BaCl_2$ is a dielectric, but surface contaminates on microfabricated traps can drastically increase anomalous heating rates for trapped ions [131]. The study of ion motional heating is an active area of research [132, 133, 134]. Without trapping it is not possible to quantify the impact that this contamination may have on the ions motion, but what can be assessed is if contamination is likely to end up on the surface of the trap after ablation.

3.6.2 Spot Lifetimes of Macroscopic Targets

A total of three ablation targets were tested with > 20 mg, ~ 2 mg, and ~ 0.2 mg of $BaCl_2$ on a heat-treated platinum substrate. This would correspond to a maximum surface density of ~ 500, 50, and 5 g/m^2, with the platinum strip cut to 10×2 mm^2, respectively. Unsurprisingly, the average lifetimes of the macroscopic ablation targets were unquestionably longer than that of the 5 μg targets, which are summarized in Table 3.2. Example neutral fluorescence count plots of the > 20 mg and ~ 0.2 mg targets are presented in Fig. 3.12.

Target	c_1 (Pulses)	σ_1 Criteria	c_2 (Pulses)	σ_2 Criteria
Pt* > 20 mg	3807	15 / 16 ≈ 0.94	2537	11 / 16 ≈ 0.69
Pt* 2 mg	1554	14 / 16 ≈ 0.88	661	8 / 16 $= 0.5$
Pt* 0.2 mg	4494	13 / 16 ≈ 0.81	2061	7 / 16 ≈ 0.44

Table 3.2: Mean lifetime c_1 of all ablation spots on the macroscopic target that satisfies the σ_1 criteria. Mean lifetime c_2 of only the spots that produced enough neutral counts to satisfy the σ_2 criteria.

Notably, the 0.2 mg ablation target lasted longer than the 2 mg target. It may be possible to attribute this discrepancy to areas of high and low $BaCl_2$ on the surface of

the heat-treated platinum target, as shown in Fig. 3.13, but more spots would have to be sampled to have a better representation of the entire population.

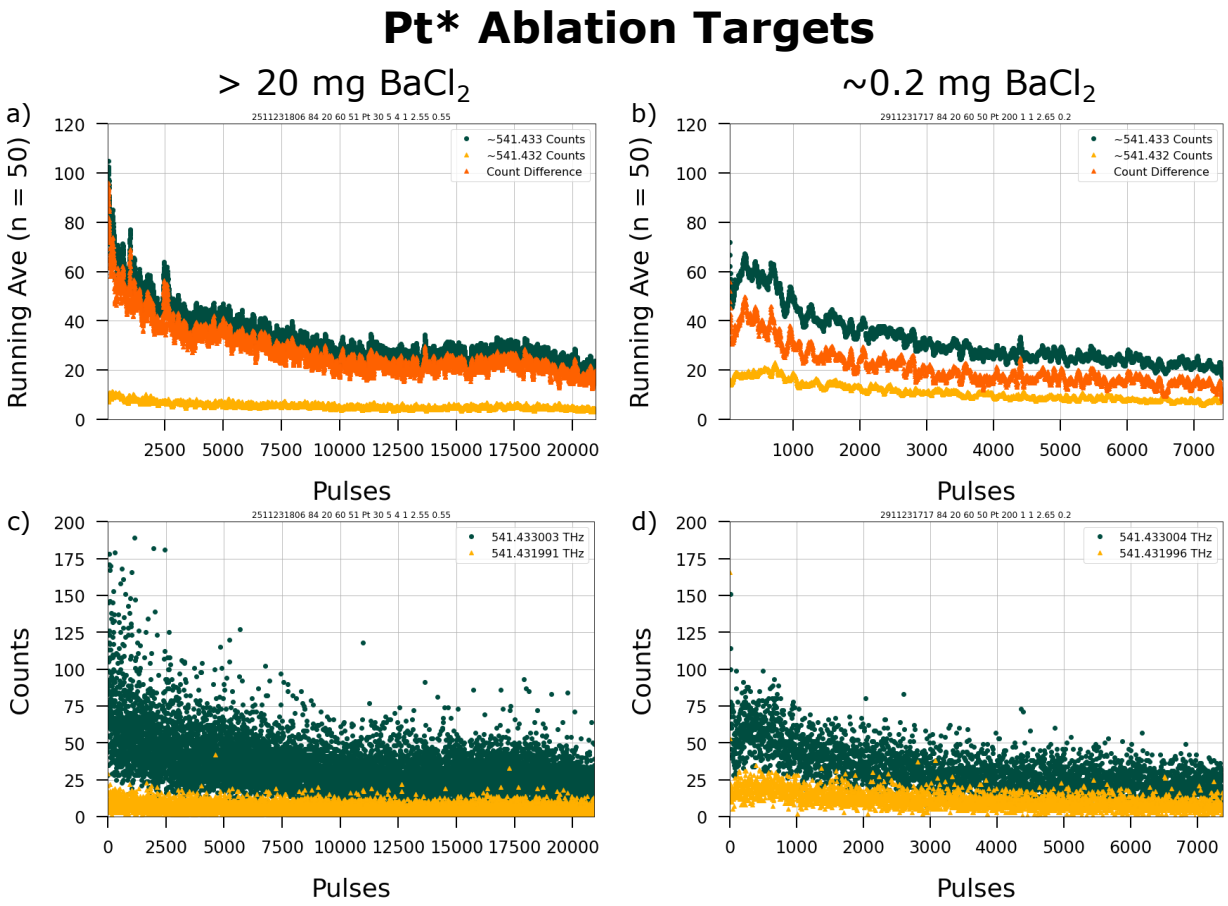


Figure 3.12: a-b) Running average ($N = 50$ total pulses) of the neutral counts collected from ^{138}Ba atoms at the best performing spot on the > 20 mg and ~ 0.2 mg macroscopic ablation targets. The green circles represent the running average of the collected counts on-resonance. The gold triangles are the running average of the counts when the 554 nm laser is tuned off-resonance. The orange triangles are the difference between the running average of the on and off resonance counts. c-d) The neutral counts collected after each ablation pulse.

The macroscopic targets (the $BaCl_2$ is visible by eye) are presented in Fig. 3.13. Fig. 3.13a shows a Pt* type ablation target with ~ 2 mg of $BaCl_2$ on the surface. The dark areas on the SEM image indicate the presence of $BaCl_2$. The ~ 0.2 mg target has

considerably less $BaCl_2$ coverage compared with the $\sim$ 2 mg target, which is to be expected. While these ablation targets contain far too much material to ever be compatible with a ^{133}Ba salt target, these can be used in lieu of metallic barium atomic sources, which oxidize in air within a matter of minutes. The surface of these macroscopic heat-treated Pt* targets is much smoother than what is typically found when the salt is not melted.

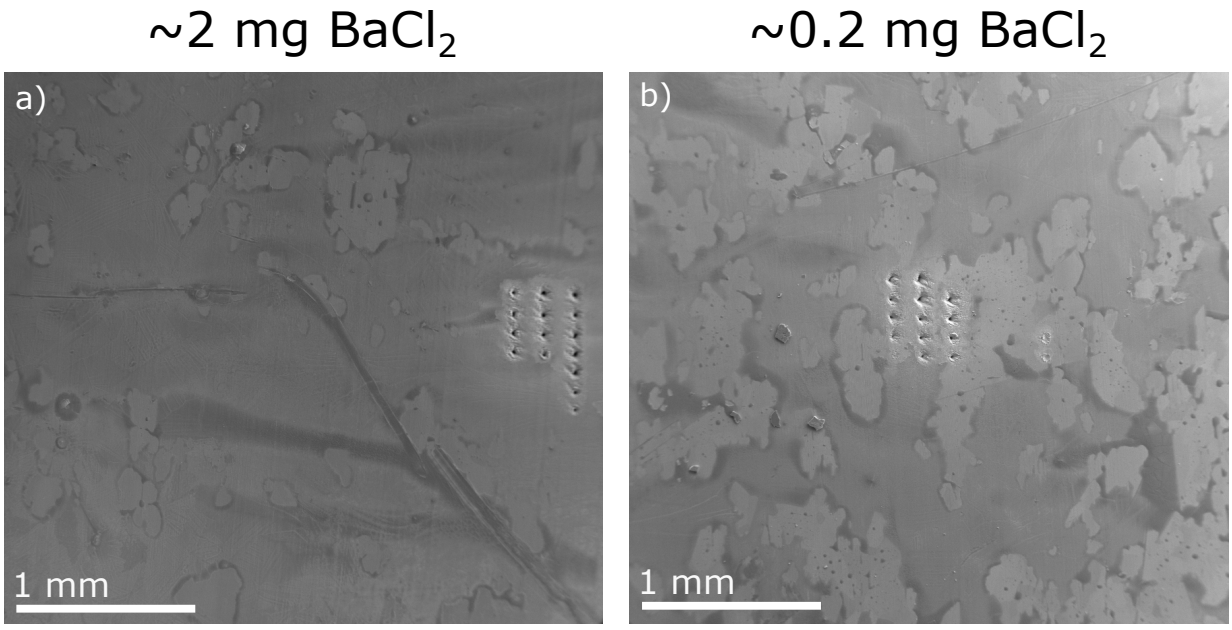


Figure 3.13: a) Large scale SEM image of an ablation target with $\sim$ 2 mg of $BaCl_2$. The dark areas are high concentration of melted $BaCl_2$, confirmed by EDS measurements. b) SEM image of a $\sim$ 0.2 mg $BaCl_2$ ablation target. Similarly to the $\sim$ 2 mg target, dark areas indicate the presence of $BaCl_2$.

Gold microfabricated chips were placed in the high-vacuum ablation test chamber at a position similar to where the surface trap had been relative to the ablation target in the ultra-high vacuum experiments. The macroscopic targets were then ablated for $>$ 1000 pulses. The gold microfabricated chips were removed and imaged, showing that regardless of heat-treatment and the amount of $BaCl_2$ originally deposited on the Pt* ablation targets that contamination is still likely to occur. More details are presented in Fig. A.5, which can be found in the appendix.

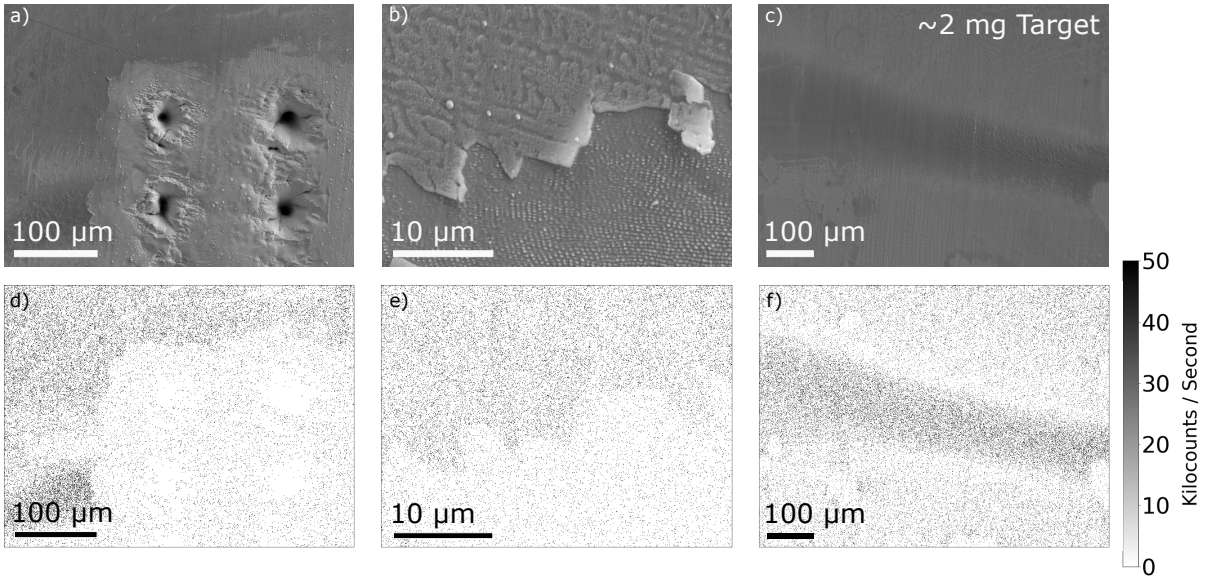


Figure 3.14: a-b) SEM images of the $\sim$ 2 mg macroscopic ablation target. A clear crust has formed on the majority of the surface as shown in Fig. 3.13. The crust is estimated to be < 2 μg thick. c) A vein of $BaCl_2$ indicated by the dark line through the center of the SEM image. d-f) Corresponding EDS measurements confirming the presence of $BaCl_2$.

SEM and EDS images of the $\sim$ 2 mg heat-treated ablation target are shown in Fig. 3.14. When the surface density of $BaCl_2$ crystals becomes greater than $> 2000\,\mu g/(10\times 2\,mm^2) \approx 100\,\mu g/mm^2$ on the surface of the platinum, then a thin crust of $BaCl_2$ forms after melting the salt. This crust is a favorable property of these ablation targets, as the formation of it makes production of neutral barium atoms more consistent.

3.7 Concluding Remarks

Two different recipes for fabricating heat-treated ablation targets with minimal amounts of $BaCl_2$ has been tested, motivated by the $^{133}Ba^+$ isotope. With both heat-treatment techniques, a more uniform distribution of the $BaCl_2$ was created on the surface of the substrate. The heat-treated targets significantly outperformed the non heat-treated ablation targets, both in terms of uniformity (factor of $\sim$ 4 higher) and spot lifetime (factor of $\sim$ 3 higher). The Pt* type ablation targets are favored due to the ease of fabrication when compared with the Al* type ablation targets. This is due to the fact that the Pt*

type targets can be fabricated in atmosphere with readily available power supplies, without the use of a high-vacuum heating stage. In the case of the Pt* type ablation target, the substrate is heated to temperatures that enable melting of the microgram quantities of $BaCl_2$. Melting of the salt disperses concentrated rings of $BaCl_2$ that form during the deposition process, removing a major obstacle when it comes to consistent neutral barium production. Characterization of barium atomic sources for trapped ion experiments has not been previously done using SEM and EDS, which has been a powerful tool, providing insight into the distribution of the salt on the surface of the targets before and after ablation. This work provides a detailed and tested recipe for generating neutral barium atoms via ablation from microgram quantities of salt, which is necessary when working with the radioactive isotope, $^{133}Ba^+$.

In an ideal situation, if an experimentalist could ensure that no oxidation would occur, a metallic $^{133}Ba^+$ source would be available for trapped ion experiments. The advantage that metallic ablation targets have over salt ablation targets is that the plume velocities are typically two orders of magnitude lower [81]. Unfortunately, it is not likely viable to create metallic barium from microgram quantities of $BaCl_2$, but regardless a recipe for creating metallic barium with aluminum is outlined in Appendix A.4 for the interested reader. There is general interest in creating $^{133}Ba^+$ atomic sources with less radioactivity and if it were possible to fabricate microgram quantity metallic $^{133}Ba^+$ source, this would increase the amount of slow-moving, trappable neutral barium atoms after each ablation pulse by at least an order of magnitude [43].

Chapter 4

Infrastructure for a Chip Trap

The project described in this section is meant to be an academic testbed for probing the $^{133}Ba^{+}$ and $^{137}Ba^{+}$ isotopes and their feasibility for encoding information in their hyperfine levels as well as demonstrating a novel individual addressing scheme using laser-written waveguides for driving single and two-qubit gates [72]. The project aims to trap the $^{133}Ba^{+}$ isotope in a sophisticated surface trap and utilize this isotope as a ground state hyperfine qubit (using the $6\,S_{1/2}$ state) [47], while also exploring the nuances and techniques necessary for encoding information in the $5\,D_{5/2}$ state [58]. This is one of the first academic projects designed to work with such long chains of Ba^{+} ions (16 qubits, 20 total ions) for quantum information processing or simulation.

The necessary vacuum infrastructure for housing the ion trap from Sandia National Laboratories [46], as well as many of the optics needed to perform basic trapping functions such as photoionization and Doppler cooling are detailed from conception. The beam orientation over the trap and a computer-aided design (CAD) rendering of the trap package is shown in Fig. 4.1. There are two main zones for working with ions. The first zone is for trapping, where the necessary photoionization beams are focused in order to build a reservoir of ions for faster reloading. The second zone is in the center of the trap, where quantum operations take place. In the quantum zone, Doppler cooling is still required, but so are individual addressing beams that will eventually be used to drive entangling gates. The future work regarding this project is to eventually implement two-qubit entangling gates using Raman transitions. The industry standard laser-driven gate scheme couples the internal spin states of different ions via the common motional modes and has been demonstrated on ion chains with more than 30 $^{171}Yb^{+}$ ions [27].

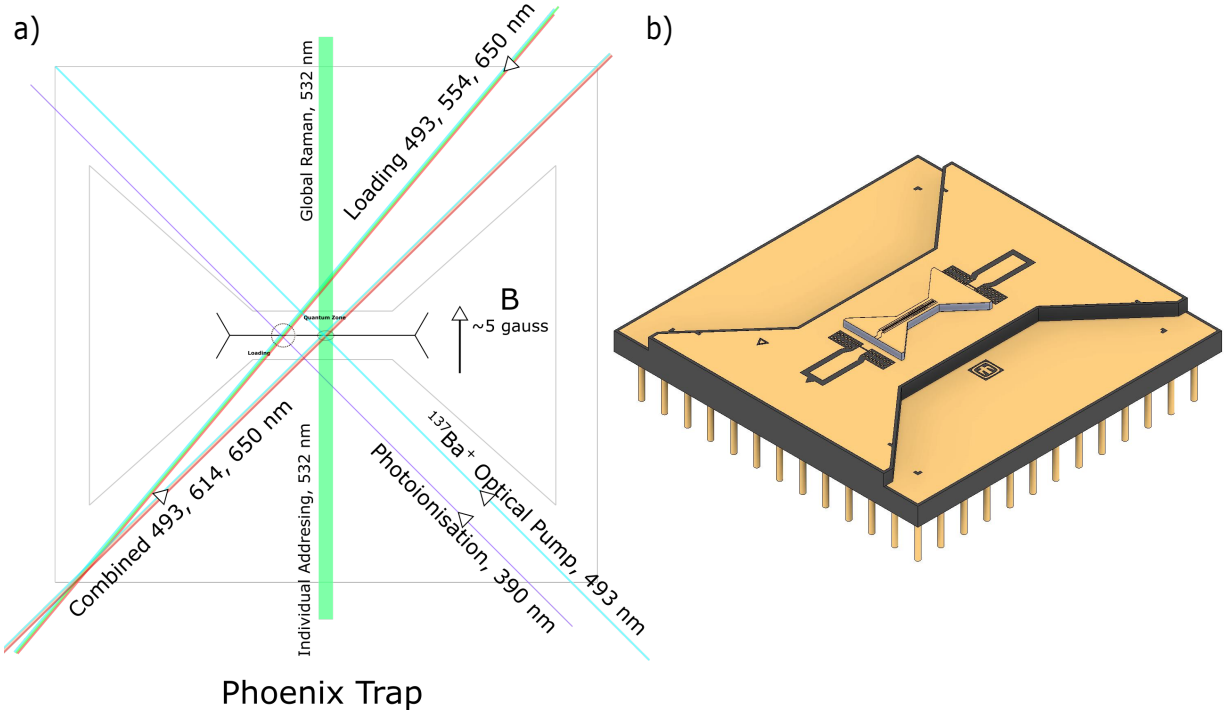


Figure 4.1: a) Top-down view of the beam orientation for addressing chains of trapped Ba^+ ions. The beams provide photoionization, Doppler cooling, repumping, and state preparation as well as measurement of the ions. Initial designs are to trap at one zone and perform gate operations in another zone, with optical infrastructure supporting both $^{133}Ba^+$ and $^{137}Ba^+$ state preparation. b) CAD rendering of the Phoenix trap package from Sandia National Laboratories [46]. The trap package consists of the trap itself, bonded to a ceramic grid pin array, which can then be mated into a zero-insertion force socket. The package is designed in a bow-tie shape for high optical access.

This project was conceptualized before the COVID-19 pandemic, however, the design and subsequent building did not take place until a couple of years after the fact. The lab space was renovated in 2021 and we moved into the space in 2022 as shown in the timeline image, in Fig. 4.2. There are two main enclosures that encase two separate optics tables. These enclosures have attached air-handling units (AHUs) that prevent temperature and humidity fluctuations by providing a constant flow of controlled air dispersed into the rooms. One enclosure is used for the main experiment with the surface trap and another is used as an area for testing optics. Without these enclosures, it would not be possible to lock lasers, stabilize high-power beam paths, or conduct any future qubit experiments reliably.

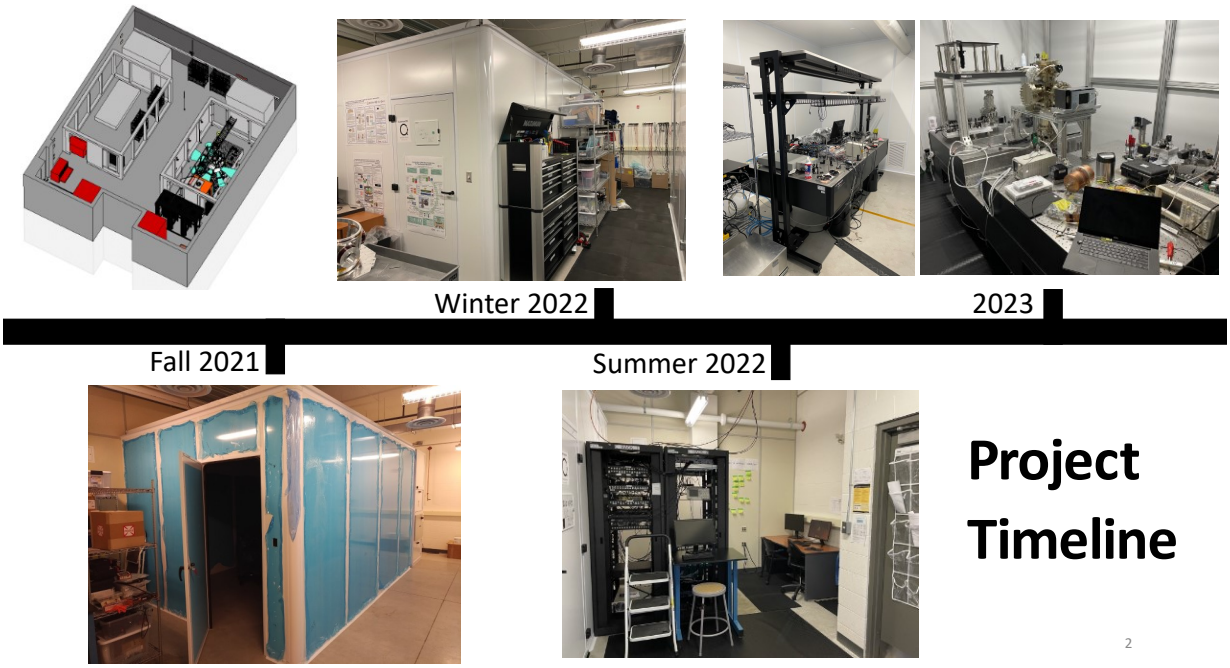


Figure 4.2: Brief timeline of the project from initial laboratory design up to installing and aligning lasers into the vacuum chamber. The room was laid out in CAD software and enclosures were built from these designs. The optical tables were installed before the enclosures were built.

4.1 Vacuum Overview

A vacuum system for an ion trap ideally provides as low of a pressure as possible, while still prioritizing optical access. The standard ultra-high vacuum pressure that is obtained for room temperature systems is at the 10^{-11} mbar level [71]. The goal of the design of this vacuum chamber is to reduce the collision rate of the ions with background gases, while maintaining enough optical access to drive high fidelity entangling gates and globally address ions at two separate zones.

This ultra-high vacuum (UHV) chamber operates at room temperature, however, the industry standard vacuum systems are almost entirely cryogenic [27, 26, 40, 21, 135]. Cryogenic systems differ from room temperature systems in two major ways. Firstly, the collision rate between trapped ions and background gases can easily reach more than an order of magnitude lower when compared with room temperature systems [21]. Secondly, the types of gases that remain are smaller molecules such as hydrogen and helium, so they

are more likely to scatter elastically and less likely to cause a chain to melt [136]. The initial concerns with cryogenic systems were that mechanical vibrations could interfere with the secular ion motion, but this has been shown not to be a limiting factor [21]. For this academic project, a room temperature system is designed and built because it requires less technical overhead.

If there is one number that the vacuum system is designed around, it is the numerical aperture (NA) for the Raman individual addressing scheme (~ 0.37). However, during the design process, great consideration was given to the numerical imaging aperture (~ 0.60), as well as providing optical access at 45° relative to the trap axes for Doppler cooling, repumping, and photoionization. The vacuum chamber utilizes re-entrant vacuum windows in order to obtain the high numerical aperture values for the Raman and imaging objectives. This is a standard technique, however, there are other ways to obtain the desired optical access such as the use of integrated optics like with laser-written [137] or planar waveguides [138], trap packaging [139] or in-vacuum objectives [140].

The UHV chamber is mainly made out of titanium, with a few sections made from stainless steel. Titanium has an advantage in that it is significantly lighter than stainless steel, given that it is about $\sim 57\%$ less dense [141]. Furthermore, titanium has been shown to have a lower untreated outgassing rate compared with stainless steel [142], mostly due to the thick oxide layer that can form on the surface of the chamber walls. Titanium reacts immediately in the presence of oxygen, which facilitates oxide layers that are ~ 5 nm thick [143]. It should be noted that it is possible to obtain similar UHV pressures with stainless steel chambers if they are properly prebaked and heat-treated, but in this case titanium was chosen because it would lower the weight of the entire chamber significantly. The chamber weighs ~ 100 kg, but if it were built entirely out of stainless steel, it would weigh > 150 kg. The entire chamber was designed (not built) previously during my masters' thesis [71], and the base pressure was simulated in MolFlow, which is a software packaged developed by CERN [144].

In order to support the chamber, a titanium frame was designed that mounted to welded tabs on the body of the custom 5-way cross shown in Fig. 4.3. A standard 80/20 frame was built off of this structure. Moving the chamber can be done with a set of large screw-jacks, that hoist the chamber a few centimeters off the table, allowing for wheels to be mounted to adapter plates on the side of the 80/20 frame. This chamber can then be moved between buildings with a cart (Uline PN: H-2548) and placed on most tables or surfaces with a scissor lift (Uline PN: H-1784).

The vacuum system design is presented in Fig. 4.3a, with the design being comprised of three main sections. Starting from the top of the chamber, these sections are referred to as the diagnostic chamber, the pump chamber, and the experiment chamber.

The diagnostic chamber is a Kimball Physics Spherical Octagon (PN: 53-180400) mounted at the top of the structure. The main purpose of this stainless steel chamber is to provide an area of high conductance for gauges, a bake valve, residual gas analyzers, leak valves, and any other instrumentation used to assess the vacuum at low base pressures. In most configurations, just an all-metal bake valve and an extractor gauge are attached to the chamber, which provides the ability to evacuate the chamber and measure the pressure at UHV. This stainless steel piece mates to the titanium pump chamber below, on an 8.0 ″ ConFlat (CF) 150 flange with 20 bolts using a copper gasket. Since this piece was stainless steel, it was prebaked, which is described in Section 4.2.

While designing the vacuum chamber, there was considerable concern about mating two metal components, steel and titanium, with significantly different thermal expansion coefficients. In practice, standard twelve-point silver-plated stainless-steel bolts are used to mate the two components with no clear indication that any major leaks developed while baking. In order to check for major leaks, helium is directed with a small nozzle into the gap between the CF flanges and pressure increases can be read on the 10^{-13} mbar level using the extractor gauge as part of the diagnostic chamber. A residual gas analyzer could also be attached to look at partial pressure measurements to diagnose the limiting background gas, and if equipped with an electron multiplier, it can be used to measure partial pressures $< 10^{-16}$ mbar level.

The pump chamber is comprised of a custom 5-way cross manufactured by VISTA Corportation. This chamber is titanium and holds all of the necessary pumps to operate at UHV. There are five ports on the pump chamber, one for the diagnostic chamber, one for the experiment chamber, one place to attach an ion pump, one place to attach a titanium-sublimation pump (TSP), and one redundant port. The 5-way cross is designed to maximize the conductance from the experiment chamber to the pumps, which in turn maximizes the effective pumping speed. The 8.0 ″ flange helps in this regard, since the conductance c from the orifice is dependant on the diameter D such that $c \propto D^3$. More details on the effective pumping speed calculations and molecular flow can be found in my masters' thesis [71].

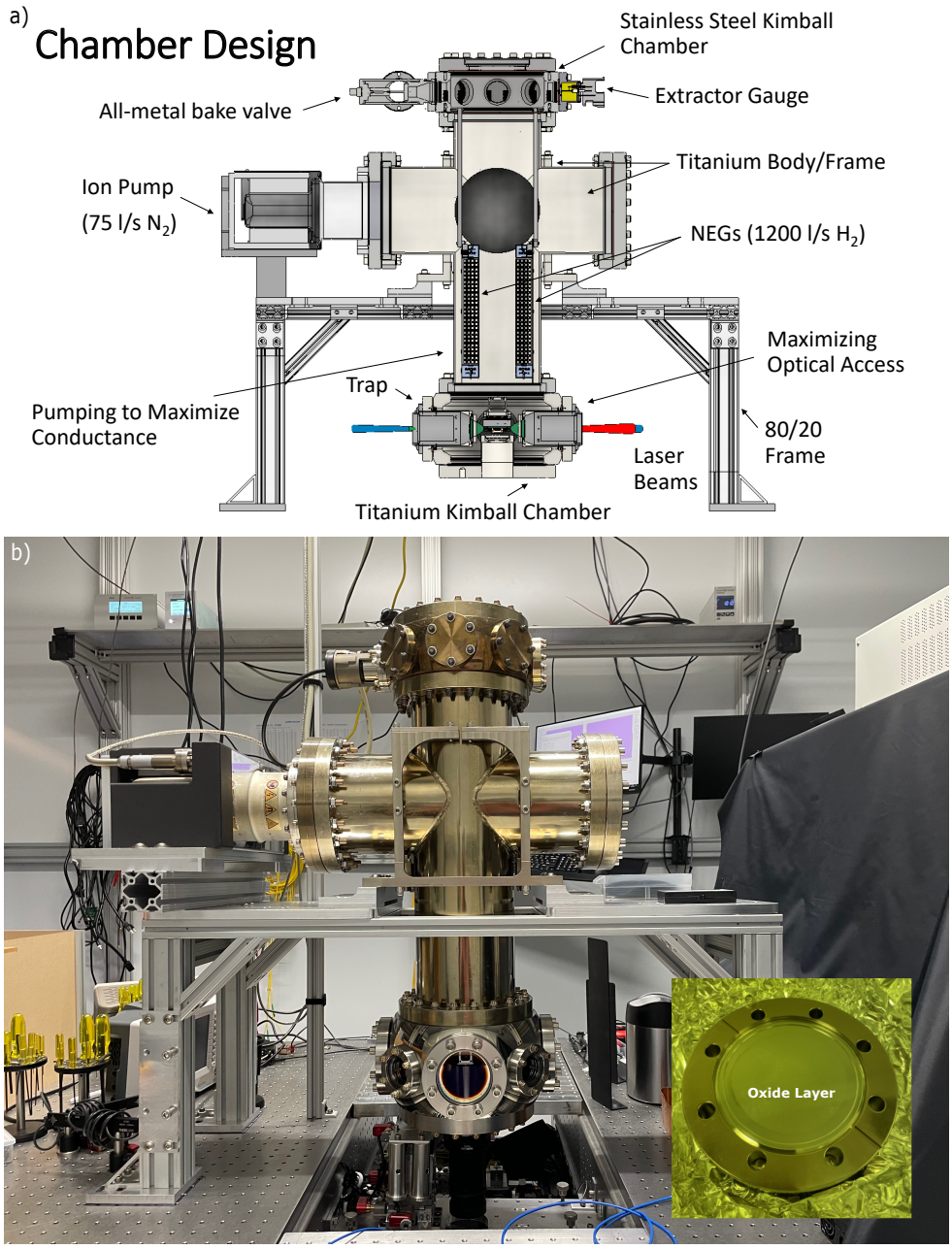


Figure 4.3: a) Internal cross-sectional description of the UHV chamber. There are three main sections of the chamber, the diagnostic chamber at the top, the pump chamber, and the experimental chamber. These sections are discussed in detail in the text. b) Photo of the UHV chamber set in the center of the optics table, directly above the imaging trench. The trap is housed at the bottom of the UHV chamber. The inset shows a titanium CF 60 blank with a visible oxide layer.

In general, to reach UHV with a vacuum chamber, there must be an ion pump to remove non-getterable gases such as hydrocarbons as well as another pump to be the main hydrogen sink. Hydrogen is usually the most prevalent gas at UHV since it is often times found in the bulk material of the chamber walls [71] and to pump this effectively one can use either a TSP or a non-evaporable getter (NEG). An NEG is a porous material with a large surface area that allows gases at UHV to stick to the surface and then be driven into the bulk of the material by running a large amount of current through the alloy [145]. The NEGs in this chamber were placed near the trap in order to maximize the effective pumping speed.

The final major part of the UHV system is the experiment chamber, where the trap is actually housed. It is here where the re-entrant viewports are attached and the electrical feedthrough provides a pathway to apply voltages to the trap. The re-entrant viewports are titanium and manufactured by MPF Products Inc, however, the coating was done by FiveNine Optics. The experimental chamber is described in more detail in the following subsection.

4.1.1 Experiment Chamber

For a trapped ion architecture based on entangling gates in long chains of ions using lasers, the NA is one of the most important factors. In order to implement this architecture, laser beams must be tightly focused onto individual ions so much so that minimal intensity is found at neighboring ions, otherwise those ions will also feel a spin-dependant force and their motion and internal spin state will also become entangled [146]. The NA can be defined by Eq. 4.1,

$$NA = n \sin\theta \simeq \frac{\lambda_o}{\pi \omega_o} \tag{4.1}$$

Where n is the index of refraction, θ is the half-angle, ω_o is the beam waist and λ_o is the wavelength of the light. Assuming a sufficiently high NA to reduce intensity cross-talk at neighboring ions is $< 10^{-4}$ level [72], than the issue becomes more fundamental in that the ions move in and out of the beams [147]. The transverse motion of the ions along the axial direction is currently considered the limiting factor in state-of-the-art machines [27].

The experimental chamber is where re-entrant viewports are mounted, which are shown in Fig. 4.4. These re-entrant viewports allow objectives to sit closer to the trap, greatly increasing the NA. The limiting factor on the Raman re-entrant viewports is not the

imaging re-entrant, but in fact the beams used for Doppler cooling the ions at the loading zone. This zone is ~ 1 mm away from the center of the trap, which is shown in Fig. 4.5.

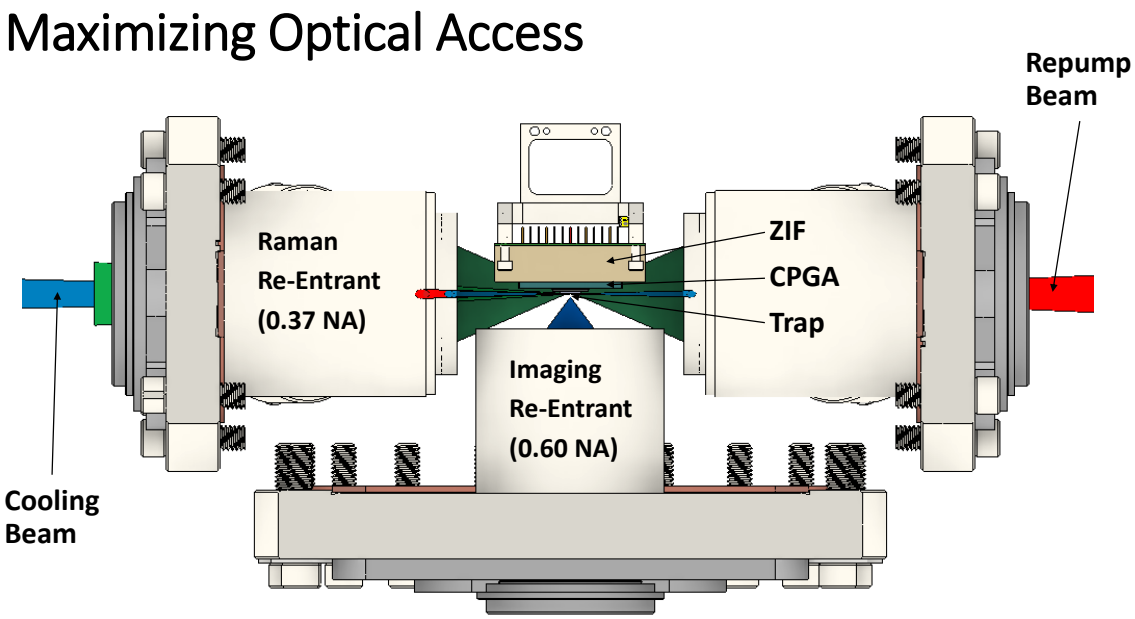


Figure 4.4: The UHV chamber was designed around the re-entrant viewports, in order to maximize the Raman and imaging numerical apertures, while still providing enough optical access for 45° beams, relative to the ion chain. There are two Raman re-entrant viewports ($\sim$ .37 NA) that allow for counter-propagating beams. The numercal aperture of these re-entrants are limited by the beams at 45° relative to the trap axis. The imaging re-entrant ($\sim$ .60 NA) is installed below the trap.

The Sandia package (trap and ceramic-pin grid array) slots into a zero-insertion force (ZIF) socket, which is soldered to a printed circuit board (PCB) using UHV solder from Accuglass (PN: 110796). The PCB material is Rogers 4350B and it is void of a solder mask, silkscreen, or any other markings. Originally, a flexible printed circuit (FPC) made from DuPont Pyralux AP was intended to bring the direct-current (DC) voltages from the outside of the chamber to the trap package, but due to the density of traces, pins could not be soldered onto the FPC without shorting [71]. The PCB is connected to an electrical feedthrough on the experimental chamber via 100 kapton-coated wires that are soldered to the PCB. These wires are attached to a PEEK 100 D-Sub Micro-D connector that plugs into the electrical feedthrough on the vacuum side.

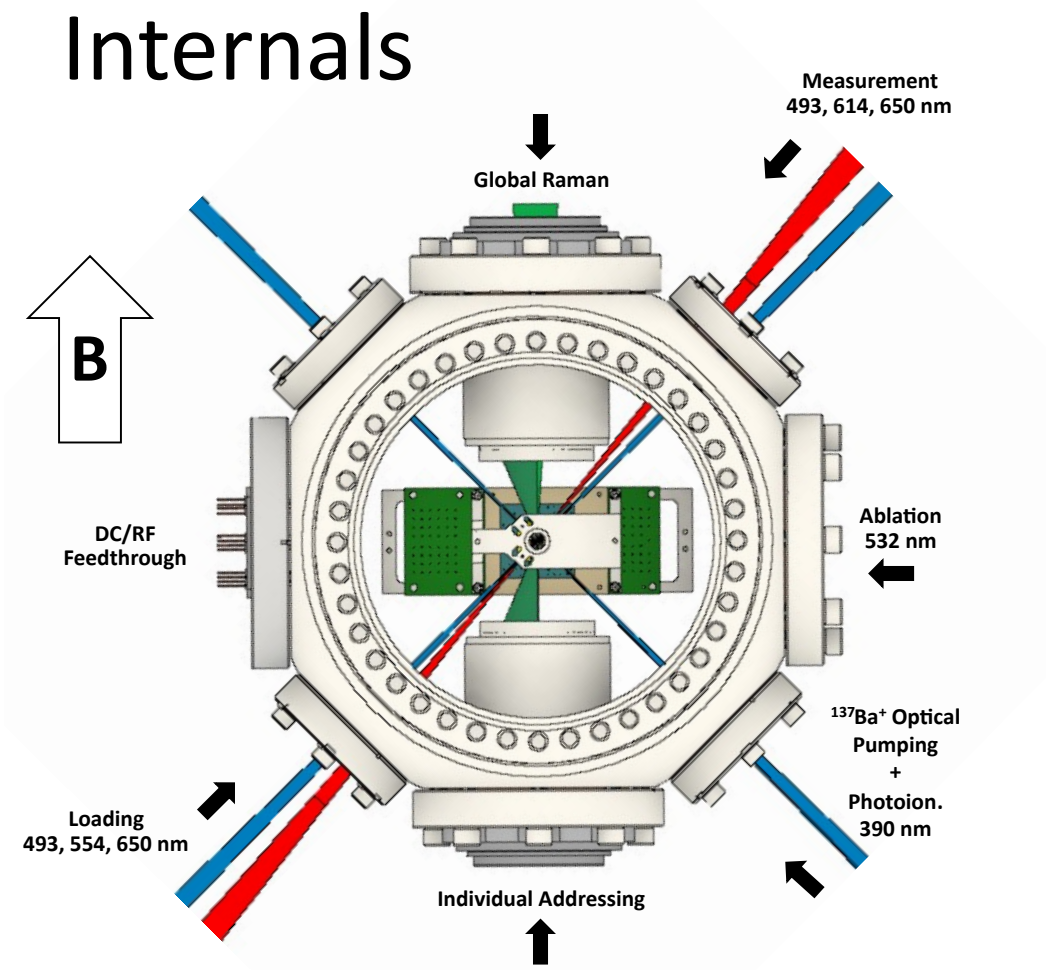


Figure 4.5: Internal components and beam orientation of the surface trap. The trap is installed in a ZIF socket, which can be soldered to wires or a PCB. The trap and ZIF are mounted to machined pieces where are held in place via groove grabbers in the center of the chamber. The internal components were machined from stainless steel. A shield ~ 5 mm away from the trap surface creates a ground plane to prevent stray electric fields from influencing the trapping potential. The shield is grounded via the chamber itself, which is connected to the optical table and a ground bar in the lab. The trap surface faces the optical table.

4.2 Initial Construction and Testing

The initial preparation and construction of the UHV system is broken down into two categories based on material; stainless steel and titanium. The stainless steel pieces were initially cleaned by sonicating them with Sparkleen™ and deionized water, followed by sonication with acetone and lastly with isopropyl alcohol. Sonication lasted at least ten minutes for each round before baking and this cleaning process was taken as a precautionary step since UHV pieces typically come precleaned from vendors.

The stainless steel diagnostic chamber was attached to a turbomolecular pump and baked at 400° C in order to remove hydrogen in the bulk of the material, as shown in Fig. 4.6a. The heating of the stainless steel is done by wrapping it with UHV foil and a set of heating tapes. After ten days, the turbomolecular pump was then shut off and the pieces are baked for another day in order to create an oxide layer on the surface of the vacuum chamber walls to prevent outgassing at UHV. Comparison between the heat-treated stainless steel and stainless steel that has not been baked can be seen in Fig 4.6b. The color of the prebaked stainless steel is relatively uniform, so there was a minimal temperature gradient on the surface of the chamber during baking.

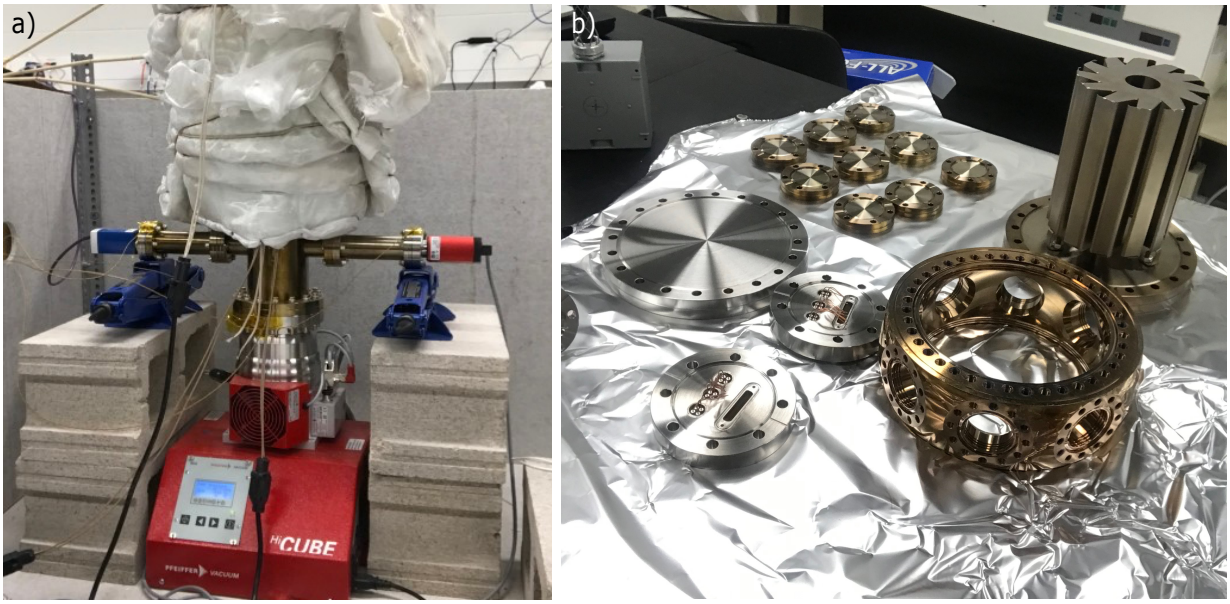


Figure 4.6: a) Picture of the diagnostic stainless steel Kimball Physics chamber being prebaked to 400° C for roughly ten days in order to remove hydrogen from the bulk material. b) A picture of the chamber after prebaking, compared with stainless steel components that have not yet been baked. The darker pieces have been prebaked, which is evident by the oxidation that has occured.

Once the stainless steel diagnostic chamber is prebaked, it can be assembled with the custom titanium 5-way cross and experiment chamber. The experiment chamber was cleaned following UHV protocol as previously described. The 5-way cross was sent from the manufacturer, doubled bagged and ready for UHV. The assembly was done in a cleanroom, class 10,000. A minimum of two people is required to assemble this chamber, as most of the pieces are relatively heavy. The first step is to attach the 5-way cross, with the custom titanium frame, to the 80/20 frame. After this, the experiment chamber which houses the trap can be attached to the bottom of the 5-way cross. The experiment chamber cannot first be attached to the 5-way cross, otherwise it will not fit onto the 80/20 frame. The prebaked diagnostic chamber is typically attached to the top of the 5-way cross after the 5-way cross is on the frame since it is made from stainless steel, making it relatively heavy.

At this point the three main sections of the vacuum chamber have been assembled and the pumps can be installed. The first UHV pump that is installed are two NEG modules. These are attached to the Kimball physics chamber via groove grabbers from both the top and bottom. They are wired in series to a feedthrough purchased from SAEs Getters,

which allows activation by running ~ 5 amps through the material. The NEGs are a Zr V Ti Al alloy, and the material must reach 550° C in order to activate after being exposed to atmosphere. Once activated by a multichannel controller from SAEs Getters, these NEG modules each provide up to 1400 l/s of hydrogen pumping speed.

The second pump that is attached permanently to the vacuum chamber is an ion pump from Agilent Technologies. This ion pump fits on a 6.0 ″ flange, so a zero length reducer is used to couple it to the 5-way cross. A custom, slightly angled bracket was machined to mate the ion pump to the 80/20 frame. This pump provides 75 l/s of nitrogen pumping speed and removes the non-getterable gases. This pump is mounted such that it is not in line of sight of the NEGs when they are activated. The 6.0 ″ and 8.0 ″ flanges are connected with twelve-point screws using a torque wrench, with a final tightening torque of 190 in-lbs.

Once the UHV pumps are installed, the chamber is moved into an environmental oven pictured in Fig. 4.7 to bake off the water at $\sim 150°$ C. The limiting factor in the final bake is the ZIF socket which claims to have a maximum operating temperature of 150° C due to the beryllium copper pins. In practice, bakes at slightly higher temperatures such as $\sim 165°$ C for weeks at a time have been implemented without any noticeable failures. The main body of the ZIF socket is PEEK, which can be baked $> 200°$ C.

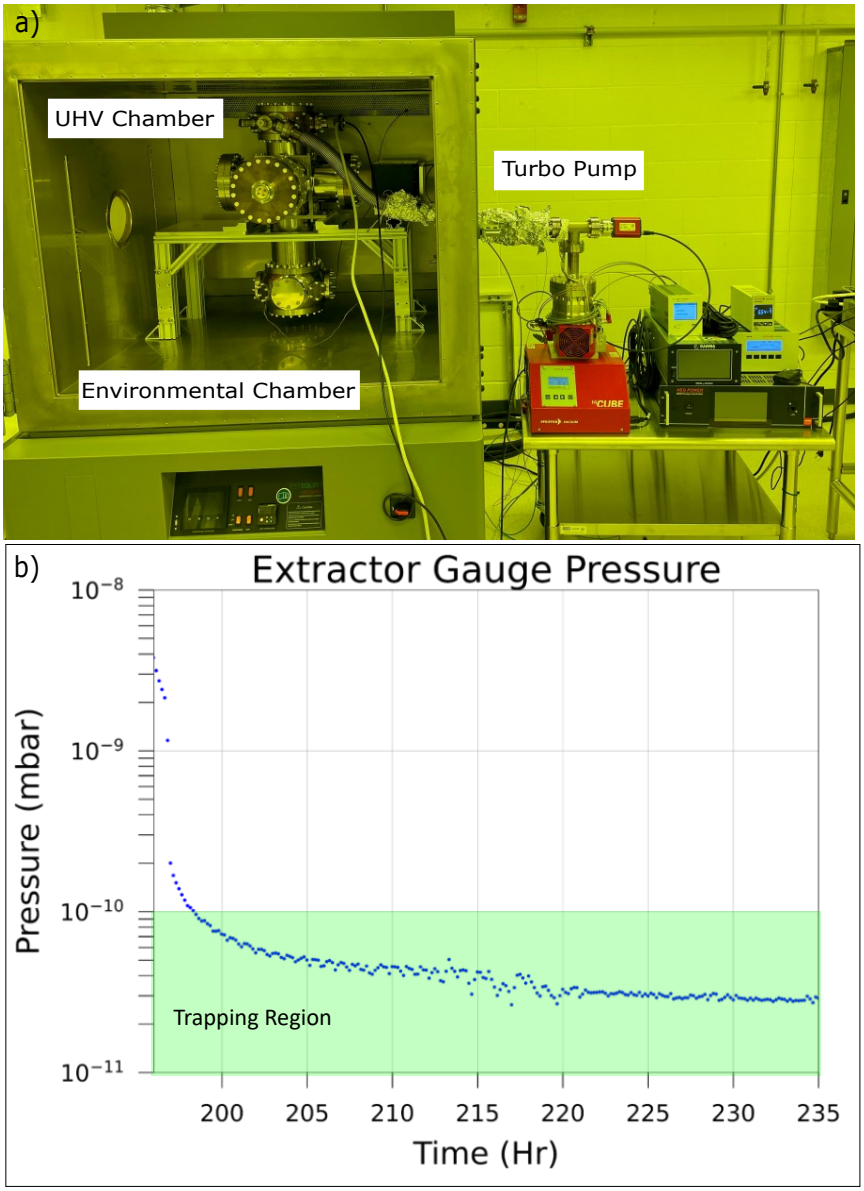


Figure 4.7: a) The assembled chamber is baked in an environmental oven in order to remove water and other surface contaminates before firing the pumps. b) Graph of the pressure taken by the extractor gauge after baking and firing the ion pump and non-evaporable getters. The pressure settled to $\sim 3 \cdot 10^{-11}$ mbar. Generally, pressures $\leq 1 \cdot 10^{-10}$ mbar is considered trappable. The custom vacuum chamber was designed such that it would fit in the environmental chamber used for baking.

Once the vacuum chamber is moved from a workbench to the inside of the environmental oven, it can be baked and UHV can be obtained. At the time of writing, this chamber has been baked and pressure tested > 5 times. What is described here is the first three bakes, proving it can obtain UHV. The first bake is a pressure test without any of the high-outgassing internal components necessary for trapping, to find the best possible base pressure. The second bake included internal components such as the ZIF, test trap package, and 100 wires for controlling the trap. The third bake included the test trap package and wires soldered directly to the ZIF with UHV solder. The following steps can be used to reach UHV:

- Install the chamber in the environmental oven, attach the thermocouple to the experimental chamber and attach the turbomolecular pump to an all-metal bake valve located on the diagnostic chamber.
- Start the turbomolecular pump and ensure the pump reaches 1000 Hz rotation speed. In most cases, the chamber is left to evacuate overnight, so that the pressure read on a gauge near the turbomolecular pump is $< 1 \cdot 10^{-7}$ mbar.
- Set the desired profile to ramp to 150° C. This is generally in 10° C increments every hour. Soak at 150° C for at least 12 hours before ramping back down to 80° C.
- Fire the NEGs using the multichannel controller, the program will run for ~ 1 hour. Keep the turbomolecular pump attached and continue evacuating the chamber.
- After the NEGs are finished firing, the chamber can be ramped back down to room temperature, at which point the turbomolecular pump will be valved off and then shut off. The ion pump can then be "flashed" by turning the pump up to -7000 volts for ~ 15 seconds in order to degas it. The ion pump is set to -3000 volts for continuous operation.

After these steps, UHV $< 5 \cdot 10^{-11}$ mbar is usually obtained as read by the extractor gauge on the diagnostic chamber, as shown in Fig. 4.7b. While constructing the vacuum chamber for the first time, a TSP was initially installed on the 5-way cross as well, but it was removed after the NEGs were found to significantly outperform the TSP by roughly an order of magnitude in achievable base pressure. The first base pressure measurement without any trap package, ZIF socket, or wires yielded $\sim 1 \cdot 10^{-11}$ mbar. The second base pressure measurement with the trap, ZIF, and wire harness yielded $\sim 3 \cdot 10^{-11}$ mbar. Finally, a third base pressure measurement with the full internal setup including 100 kapton-coated wires soldered directly to the ZIF from MDC (PN: 9921035) reached $\sim 4.4 \cdot 10^{-11}$ mbar.

4.3 Trap Alignment and Additional Infrastructure

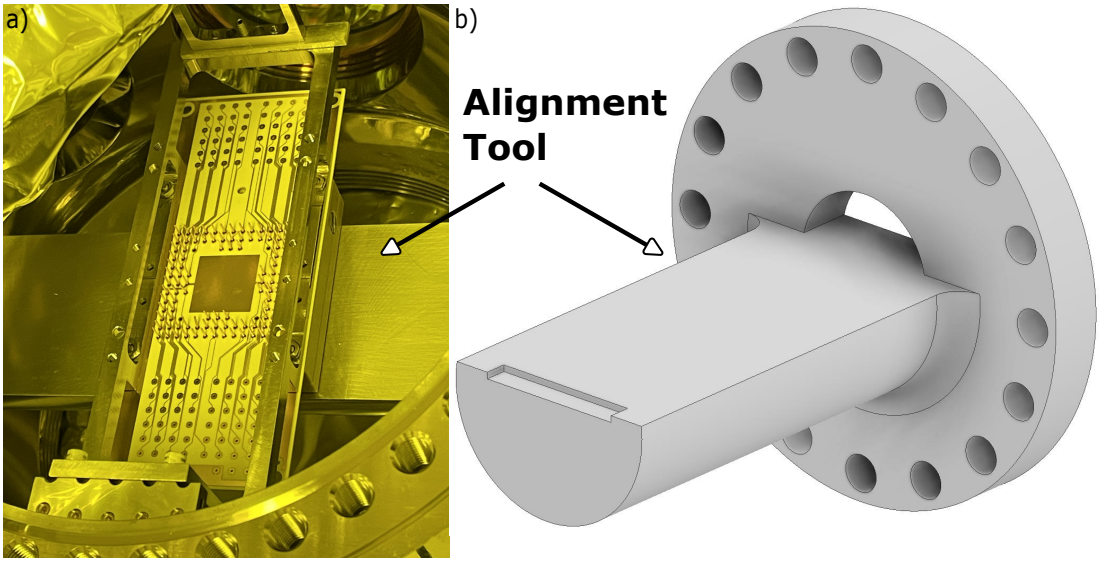


Figure 4.8: a) Test trap package with ZIF and internal machines pieces being aligned by the tool mounted onto the Kimball physics chamber (PN: 53-140500). b) CAD rendering of the alignment tool, where the trap package is meant to slot into the groove at the end. Two of these alignment tools are used to center the trap to the center of the experiment chamber.

The center of the trap is meant to sit at the center of the experiment chamber. In order to align the trap, two machined pieces were mounted at the Raman re-entrant positions, shown in Fig. 4.8. A ceramic-pin grid array (CPGA) is slotted into the ZIF and initially mounted near the center of the trap, with some of the machined mechanical pieces left loose. These pieces are adjusted so that the CPGA is slotted into the alignment tool and then the machined mechanical pieces holding the ZIF are tightened. This will fix the trap package to the center of the chamber ± 150 μm. The real trap package is incredibly fragile with wirebonds that can easily be broken, so a CPGA without the real trap is used for alignment, which can then be removed and the actual trap can be installed.

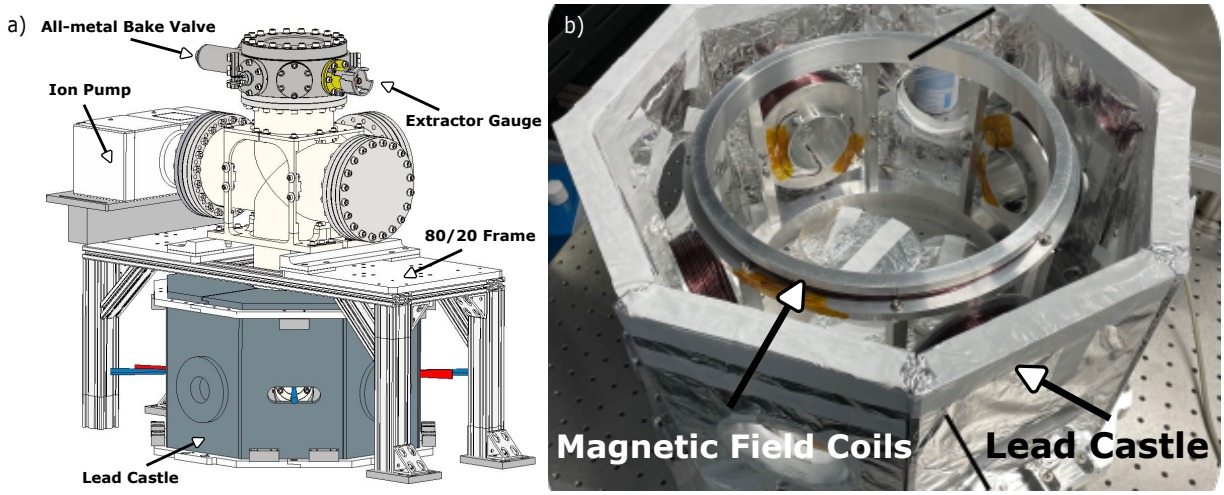


Figure 4.9: a) CAD rendering of the custom lead castle enclosing the experimental vacuum chamber, where the radioactive $^{133}Ba^{+}$ will be housed. The lead castle was designed to fit under the 80/20 frame holding the vacuum chamber. b) Picture of the assembled lead castle wrapped in aluminum foil, which is in addition to an epoxy coating. The magnetic field coils sit inside the lead castle, wrapped around an aluminum structure.

The custom lead shield from Nelco Worldwide is machined from an alloy, coated in an epoxy, and designed in an octagonal pattern in order to prevent radiation from escaping out of the chamber, where $^{133}Ba^{+}$ salt will be installed. There are apertures in the lead castle to allow for beams to enter and exit the vacuum chamber. These apertures can be plugged with another custom circular lead piece if they are not in use. The side wall bricks are 1 $''$ thick and the top layer is 0.5 $''$ thick. In general, lead shielding could be manufactured from metal casting as well, and lead shielding becomes easier if less radioactive material is used or the traps are packaged [136], reducing the footprint of the vacuum chamber.

Two 1 mL glass V-vials with 0.5 mL of 0.1 molar HCl each containing 1.85 MBq of $^{133}Ba^{+}$ salt have been obtained from Stuart Hunt & Associates Ltd. The $^{133}Ba^{+}$ was purchased without any stable isotopes added and was requested to be pulled from the master batch with the highest specific radioactivity, which should be the most concentrated batch. The planned amount of $^{133}Ba^{+}$ that will be installed is $\sim$ 3.7 MBq, which is considerably less than what was installed in a previous experiment ($\sim$ 18.5 MBq) [115, 148].

The radiation exposure of a worker outside the chamber aligning optics for a time t in hours can be calculated based on the attenuation factor k, radioactivity $A = 3.7$ MBq, distance from the radioactive sample $d \approx 0.3$ m, and measured exposure rate constant Γ:

$$\dot{X} = \frac{\Gamma A k t}{d^2} \tag{4.2}$$

The centi-value layer is 0.5 ″ of lead for the $^{133}Ba^{+}$ isotope [149], so considering the thinnest portion of the lead enclosure at the top is 0.5 ″ thick, then the attenuation factor is $k \approx 0.01$. The exposure rate constant Γ has been measured from previous experiments in terms of mCi [149]. This can be converted to more useful units,

$$30.4\,\mathrm{mSv\,cm^2/(mCi\,hr)} = 30.4 \times \frac{1}{37}\,\mathrm{mSv\,cm^2/(MBq\,hr)}$$
$$\Gamma \approx 0.822\,\mathrm{mSv\,cm^2/(MBq\,hr)}$$

Putting this together, it can be shown that the exposure rate is quite low given the amount of radioactive material and the lead shielding,

$$\dot{X} \approx 0.034\,\mu\mathrm{Sv\,/\,hr} \tag{4.3}$$

This means that a worker accumulating 2,000 hours (40 hours a week, for 50 weeks a year) within 30 cm from the chamber would only be exposed to ~ 68 μSv a year. This is roughly two orders of magnitude lower than what the average person is exposed to each year (~ 6.2 mSv) [150].

4.4 Optical Infrastructure

This section deals with the optics required for trapping. All of the continuous wave (CW) beampaths are designed in a similar fashion, allowing for the necessary optical mechanical components in order to remotely control the experiment as well as focus light along the ion chain. The telescopes used to focus light are designed to be achromatic, meaning that regardless of the transmission wavelength (455-650 nm), the focus is at relatively the same position along the optical axis. This is one of the advantages of working with barium since all relevant dipole transitions are within 200 nm of each other: $\sim$ 455, 554, 585, 614, and 650 nm.

The first task for addressing chains of ions is to design a telescope with minimal chromatic aberrations. This was done in OpticStudio, where off-the-shelf achromatic cylindrical

lenses from Thorlabs were used to reshape the x-axis and y-axis beam waists after a collimator independently such that they could be focused down by a final spherical achromatic lens at the ion chain, as shown in Fig. 4.10. The use of a final spherical lens to focus the beam at the ions prevents the x and y-axis beam waists from focusing at a different location along the optical axis. Consideration was given to designing custom achromatic cylindrical lenses, but this was abandoned as the only real gain would be a slightly more compact telescope. The desired beam waists for the x-axis $\omega_x \approx 200$ μm and y axis $\omega_y \approx 18$ μm were chosen such that there would be $> 90\%$ intensity uniform along an ion chain and $< 1 \cdot 10^{-4}$ power clipping on the trap as the beam skims along the surface [46].

The achromatic design was first simulated in OpticStudio before being built and tested by taking high dynamic range images of the beam waists [151]. The 500 mm effective focal length was chosen such that optomechanical components could be placed after the beam has started to focus into the chamber, to prevent incurring more aberrations. In general, there are two piezo controlled mirror mounts positioned after the achromatic telescopes in order to give full angular control of the beam at the ion location. There is also a motorized translation stage underneath the spherical focusing lens in order to move the focus along the optical axis. The beam is picked-off after the achromatic telescope and sent to a 2D position sensor from Thorlabs (PN: PDP90A), so that changes in the position of the focus at the ion can be mapped to the sensor in future calibration routines. The specifics of the optical and mechanical designs can be found in more detail in my masters' thesis, which is when the boards were designed, but not built [71].

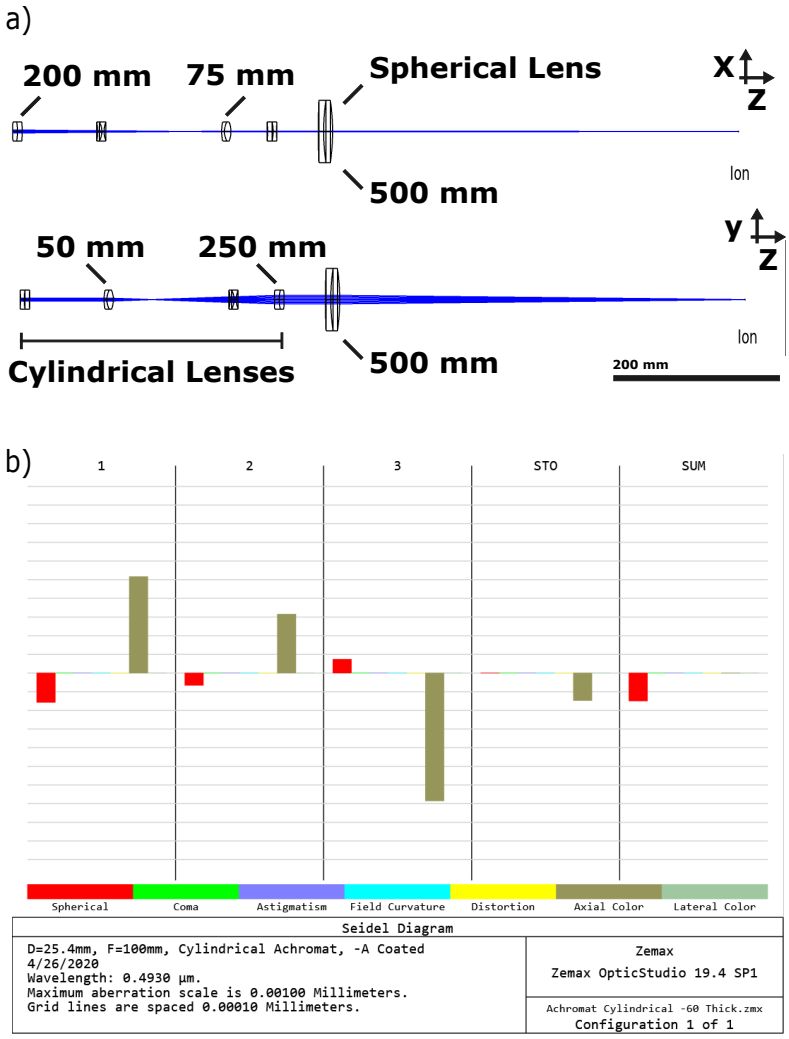


Figure 4.10: a) Ray-tracing in OpticStudio of an achromatic telescope for globally addressing chains of ions using off-the-shelf components [71]. The achromatic telescope independently reshapes the x and y-axis with cylindrical lenses before being focused down with a spherical lens. b) Seidel diagram showing the that the most common optical aberrations are spherical and axial color.

Two of the three designed CW boards for addressing global chains of ions are shown in Fig. 4.11. These boards provide photoionization and Doppler cooling capabilities for the barium ions and their modular approach makes testing as well as initial alignment to the trap easier. The boards could be made slightly more compact, but the limiting factor in this case is the achromatic telescope. In order to make this telescope more compact,

concave cylindrical lenses would have to be designed. All of the achromatic cylindrical lenses are convex, leading to a longer overall length.

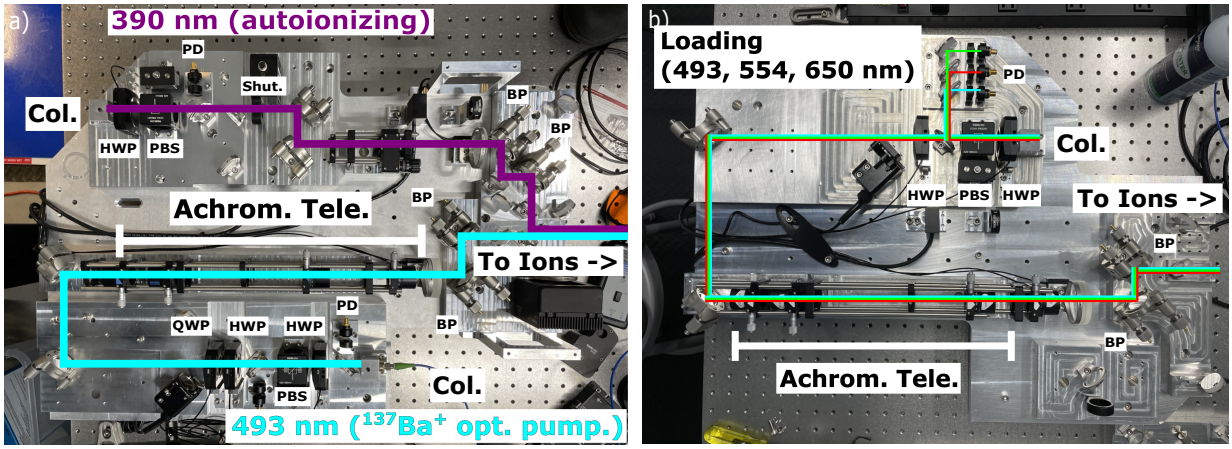


Figure 4.11: a) Assembled optical pegboard for photoionizing neutral barium and optical pumping of $^{137}Ba^{+}$. There are many components such as half-wave plates (HWP), quarter-wave plates (QWP), polarizing beam splitters (PBS), collimators (Col.), photodiodes (PD), beam pointing mirrors (BP), as well as the achromatic telescopes. The main base board is $\sim$ 1 inch thick and machined from aluminum. This is connected to the optical table with 2 inch thick posts from Thorlabs (PN: P2). Smaller boards sit ontop of the large base board, making the design more modular. The light from each laser is initially fiber coupled, modulated, and sent to the collimators on these pegboards, before entering the telescope and focusing at the ions. b) Assembled optical pegboard for providing first-step photoionization beams as well as beams for Doppler cooling and repumping Ba^{+}. More detailed optical schematics can be found here [71].

The layout of the optics table is depicted in Fig. 4.12. The photoionization board is depicted in Fig. 4.11a and the loading board is depicted in Fig. 4.11b. The cooling and repumping board has been designed and built as well as an ablation laser board which will provide a mechanism for producing neutral barium atoms. The optical system for imaging the ions has also been designed and implemented by a previous student, Ali Binai-Motlagh [151]. The Raman individual addressing system for driving gates in chains of ions has been designed and tested as well by other past students on the project, namely Ali Binai-Motlagh and Nikolay Videnov [72, 151, 152], and upgrades are being pursued.

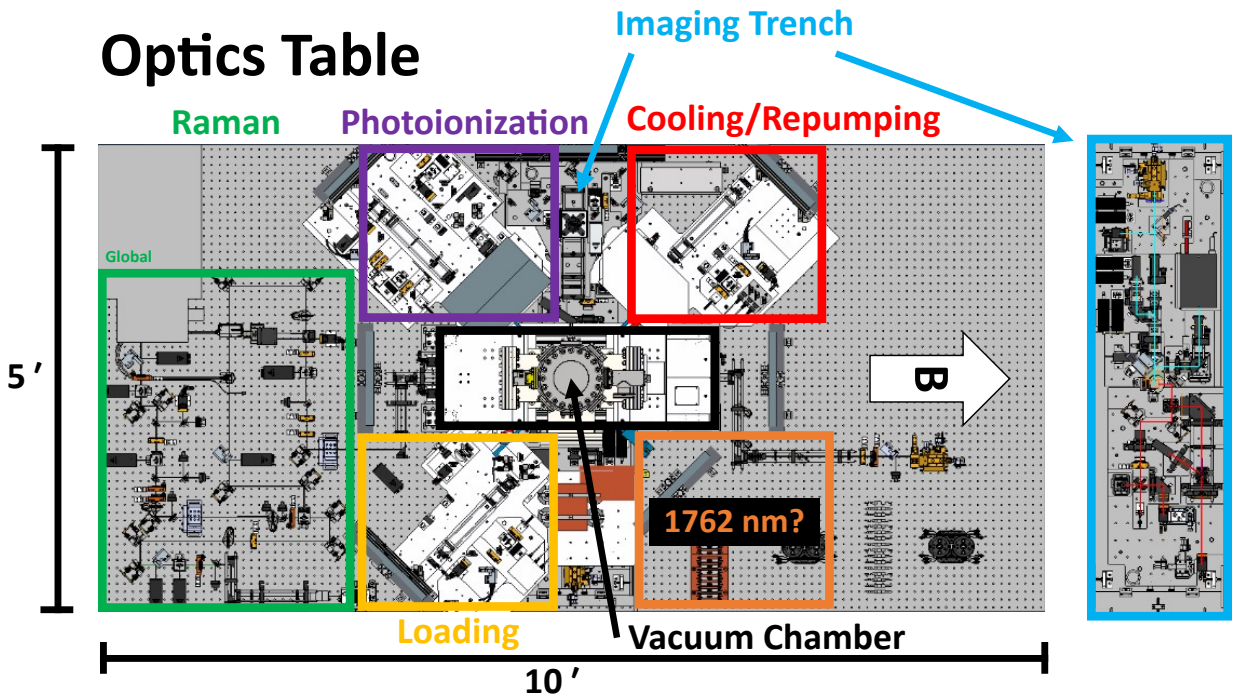


Figure 4.12: Layout of the optical table showing all of the necessary beampaths for loading, cooling, and further manipulating chains of barium ions. The optical table is comprised of different sections, each with a unique set of optics for various purposes. The photoionization board has two beam paths: one carries 493 nm light for optical pumping and another carries 390 nm light for photoionization. The cooling and repumping board carries 493, 614, and 650 nm light. The loading board carries 493, 554, and 650 nm light. These beams are necessary for basic processes such as Doppler cooling. The inset shows the imaging valley with multiple beampaths for detecting ions [151, 153].

The majority of the beam preparation design, like initial fiber coupling out of the laser head, doubling, locking, modulating (either with an acousto-optical modulator or an electro-optical modulator), beam combining and so on has all taken a fiber based approach. The upside with this, as shown in Fig. 4.13, is that it saves space and that it is easier to setup. However, there is certainly more power loss and it remains to be seen if polarization fluctuations could plague experiments. The majority of the lasers are from MOGLabs, integrated with AOSense controllers, and locked on a HighFinesse wavemeter (WS8-2). The wavemeter lock (± 2 MHz) is more than adequate for driving ~ 20 MHz wide transitions. This setup was used to run the experiments described in Section 3.

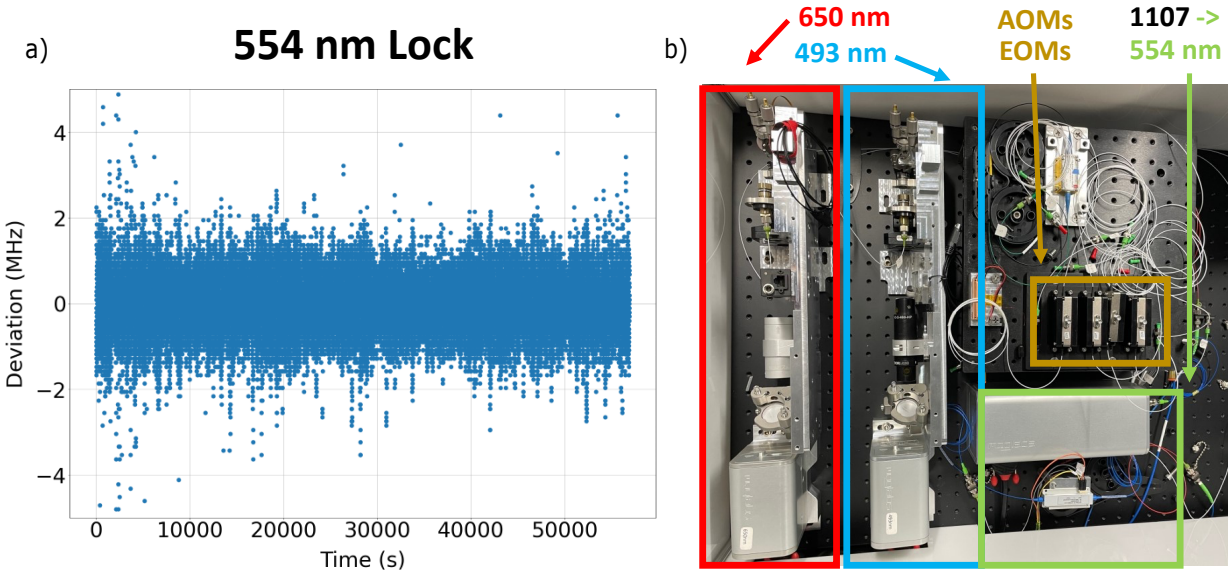


Figure 4.13: a) The first-step photoionization beam locked to $\sim$ 2 MHz using a HighFinesse WS8 wavemeter. This is necessary for driving transitions that have a linewidth of $\sim$ 20 MHz. b) Optical pegboards housing laser heads from MOGLabs and fiber coupling beampaths for sending light through fiber-based doublers, EOMS, and AOMs before being sent to the larger pegboards in Fig. 4.11. The electrical infrastructure necessary to power these devices can be found in Appendix B.

4.5 Current State

The vacuum system was originally placed on the optical table with a "test" trap in order to measure neutral fluorescence, align the imaging system, and attempt to trap. Attempts were made to load the $^{138}Ba^{+}$ isotope, however, many of the DC electrodes ($>$ 60%) were shorted internally on the trap package. This trap package from Sandia National Laboratories is a physical test sample that has failed to pass the required electrical tests. It remains unclear if this package is suitable for trapping because our RF connection also had failed at some unknown point throughout the experiment, which would clearly prevent the trapping of ions as well.

As of now the last few months have been spent making the internal wiring more robust, as the 100 wires were initially soldered directly to the ZIF. This provided no tension relief for the DC wires, causing multiple wires to break at the solder joint. A PCB is now soldered to the ZIF, which is then in turn soldered to 100 kapton coated wires. The PCB is pictured

in Fig. 4.8. This rewiring has taken the better part of five months, lead by masters students Ali Mustafa Khatai and Akimasa Ihara. At the time of writing, a new wiring harness has been completed, pressure tested, and installed in the UHV chamber. Final preparations are being made before baking and installing the radioactive $^{133}Ba^{+}$ inside the chamber.

Chapter 5

Amplitude-Modulated Entangling Gates

This section outlines computational simulations aimed at developing a similar, but variation on a previously proposed, widely accepted method for creating high-fidelity (> 0.9999) entangling gates in long chains of ions ($n > 2$) [154]. The native ion gate of choice is the Mølmer–Sørensen gate due to the fact that changes in the motional state are suppressed when driving spin-spin interactions [14] and that it can be used without having to cool to the motional ground-state [155].

5.1 Background and Motivation

The internal electronic state of an ion, often described conceptually as a spin, is the basis for quantum information processing with trapped ions. It is this spin state that is ultimately measured and it is this spin state that is manipulated over the course of computation. However, the way that the spin state is manipulated is via the motion of the ion. The motion of an ion in a trap is understood and modelled as a simple harmonic oscillator. There are many motional modes, with each mode represented by a series of Fock states $|n_{\mathbf{j}_1}, n_{\mathbf{j}_2}, ..n_{\mathbf{j}_i}...\rangle$. The Hilbert space $\mathcal{H}_s$ spanned by the spin basis and the Hilbert space $\mathcal{H}_m$ spanned by the motional basis creates a total combined system, in which the spin and motional (Fock) states can influence one another.

$$\mathcal{H}_{total} = \mathcal{H}_s \otimes \mathcal{H}_m \tag{5.1}$$

For the case of a three-ion chain, which is the minimum number of ions in a chain where modulation techniques become necessary for creating high-fidelity entangling gates using a bichromatic light field [156], the total size of the Hilbert space can be calculated based on the computational parameters,

$$\mathcal{H}_s = \begin{pmatrix} 1 & 0 \\ 0 & 0 \end{pmatrix} \otimes \begin{pmatrix} 1 & 0 \\ 0 & 0 \end{pmatrix} \otimes \begin{pmatrix} 1 & 0 \\ 0 & 0 \end{pmatrix} \tag{5.2}$$

$$\mathcal{H}_m = \begin{pmatrix} 1 & 0 \\ 0 & 0 \end{pmatrix} \otimes \begin{pmatrix} 1 & 0 & 0 & 0 & 0 & 0 \\ 0 & 0 & 0 & 0 & 0 & 0 \\ 0 & 0 & 0 & 0 & 0 & 0 \\ 0 & 0 & 0 & 0 & 0 & 0 \\ 0 & 0 & 0 & 0 & 0 & 0 \\ 0 & 0 & 0 & 0 & 0 & 0 \end{pmatrix} \otimes \begin{pmatrix} 1 & 0 & 0 & 0 & \cdots & 0 \\ 0 & 0 & 0 & 0 & \cdots & 0 \\ 0 & 0 & 0 & 0 & \cdots & 0 \\ 0 & 0 & 0 & 0 & \cdots & 0 \\ \vdots & \vdots & \vdots & \vdots & \ddots & \vdots \\ 0 & 0 & 0 & 0 & \cdots & 0 \end{pmatrix} \tag{5.3}$$

In the computations we deal only with qubits, so there are two possible spin states that represent the internal electronic states for each ion, giving $2^3 = 8$ possible basis states for this subsystem. The ion spin states are assumed to be initialized in the spin "up" position $|\chi_+\rangle = |1\rangle = |e\rangle$ with respect to the Pauli Z-basis. The number of Focks states for each motional mode can vary, but there are typically a total of 120 Fock states for the entire three-mode system. Two Fock states were used for the first motional mode, six for the second mode, and ten for the third mode, all initialized to the ground state. Together with the spin states, this gives a total of 960 basis states used in the simulations presented in Section 5.3.1, which corresponds to 921,600 matrix elements. Unfortunately in order to simulate a significantly larger Hilbert space (like with ten ions), a quantum computer would be needed. More information on the code used in these simulations can be found in Appendix C.1.

Now that we understand the Hilbert space that we are working within, we can discuss how the spin and motional states can become entangled. Namely, this is best described in terms of "spin-dependent" forces, where a bichromatic light field is incident on an ion, causing the coherent motional state to be displaced in optical phase space, picking up a phase $\chi(t)$ [157]. The amount of geometric phase accumulated is proportional to the maximum Rabi frequency Ω_o and Lamb-Dicke parameter η, and this phase is used to drive spin-spin interactions in chains of ions via the motional coupling. These laser-ion interactions fall under the Jaynes–Cummings class of Hamiltonians, where a two-level system in the presence of light is interacting with a harmonic oscillator in this case.

In terms of the grander scheme of quantum information processing, the native Mølmer Sørensen gate, which is built from taking advantage of spin-motion entanglement, can be combined with single-qubit rotations to make a controlled-not (CNOT) gate [158], as depicted in Fig. 5.1. The CNOT gate, combined with arbitrary single-qubit rotations, completes a universal gate set, which is pertinent for any discussion focused on quantum computing applications [159].

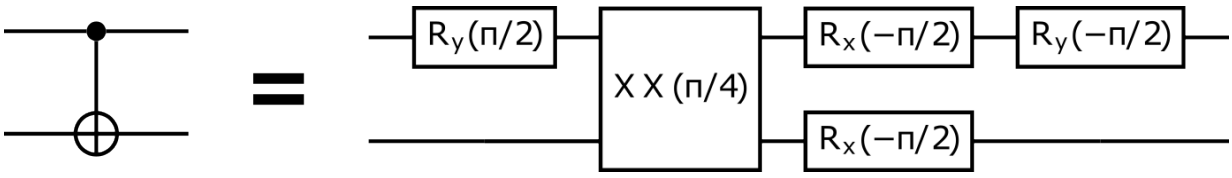


Figure 5.1: Example of a CNOT gate, commonly used in universal quantum gate sets, constructed from a series of single qubit rotations around the Bloch sphere and the native trapped ion entangling two-qubit Mølmer–Sørensen gate.

Finally, in order to actually implement Mølmer–Sørensen gates in long chains of ions, it is necessary to utilize modulation techniques. Only in the case of two-ion chains can a careful choice of parameters circumvent any type of pulse-shaping or modulation. For an ion chain with three or more ions, the Mølmer–Sørensen interaction must either have the Rabi frequency Ω [154, 160, 161], detuning parameter μ [162], or phases of the lasers sidebands, ϕ_r and ϕ_b [163], modulated over the gate time, which is typically 50-300 μs. If this is not the case, then the spin and motion of the ions will remain entangled at the end of the gate time, which will result in errors when the spin is measured and the motion is effectively traced out. The most complicated modulation techniques for driving these gates in chains of long ions utilize both amplitude modulated (AM) and frequency modulated (FM) pulse-shaping [73].

The following sections outline a set of simulations using only AM pulse-shapes, where the goal in this case is to come up with an AM scheme that will work for every possible ion pair in a specific chain. For creating a high-fidelity entangling gate that will work on arbitrary pairs of ions in a chain, there are two main criteria that must be satisfied. The first is that all spin and motion, for each ions internal state, and every motional mode, must be disentangled at the end of a gate before measurement. This is best visualized by plotting the real and imaginary parts of the coherent motional states being displaced in optical phase-space. For example, to satisfy this criteria in a five ion chain, there will be five internal states of the five ions that need to be de-coupled from each of the five motional modes. This will require that 25 phase-space trajectories be carefully calculated as the gate is applied and closed at the end of the gate. For a chain of ten ions, there will

be 100 phase-space trajectories to consider and so on. The second criteria is that the states of each ion pair acquire the correct amount of geometric phase $\chi(t)$ in order create the maximally entangled state between the ion pair of choice. This requires one to calculate the correct Rabi frequency in order to scale the phase-space trajectories accordingly, and carve out the necessary amount of geometric phase. The criteria is outlined in more detail in the following section.

In order to validate the calculated criteria for driving high-fidelity entangling gates, Hamiltonian simulations are implemented by using density matrix formalism where ρ is calculated at every time step according to the von Neumann equation [164].

$$i\hbar\frac{\mathrm{d}\,\rho}{\mathrm{d}\,t} = [H, \rho] \tag{5.4}$$

5.2 Bichromatic Laser Field Hamiltonian Simulations

Now that the basics of the underlying mechanism have been discussed, we can take a closer look at how to solve these Jaynes-Cummings type Hamiltonians to gain intuition about how these systems evolve over time when the Rabi frequency is time-varying. One of the first examples in literature detailing amplitude modulation considers the case of two ions interacting with a single mode [165]. Following an example provided in this manuscript and using the exact parameters for the Rabi frequency Ω, detuning μ, Lamb-Dicke parameter η, and motional mode ω [165], the code used in novel simulations in later chapters can be verified to an extent. Of course the best verification would be to match experimental data, but since almost all cloud-based services for trapped ion experiments do not allow access at the pulse-shaping level, this is not easily done. Pulse-shaping experiments could be done with the machine described in Section 4, since individual addressing capabilities are central a part of the design [72], but this will be for future endeavours.

In order to verify the code, the first Hamiltonian that is considered is the case of two ions in a bichromatic light field with a single motional mode, as described by Eq. 5.5,

$$\begin{aligned} H_{BC} =& \hbar\Omega(\sigma_+^1 + \sigma_+^2)(e^{i\mu t} + e^{-i\mu t})(e^{i\eta(ae^{-i\omega t} + a^\dagger e^{i\omega t})}) \\ &+ \hbar\Omega(\sigma_-^1 + \sigma_-^2)(e^{-i\mu t} + e^{i\mu t})(e^{-i\eta(a^\dagger e^{i\omega t} + ae^{-i\omega t})}) \end{aligned} \tag{5.5}$$

The raising and lower operators for the spin of the first ion are σ_+^1 and σ_-^1, while σ_+^2 and σ_-^2 denote the spin raising and lowering operators for the second ion. The creation and

annihilation operators are present for moving up and down the harmonic oscillator ladder, as $a^\dagger$ and a, respectively. This Hamiltonian is a few steps away from the Mølmer–Sørensen Hamiltonian, which requires the Lamb-Dicke as well as another rotating-wave approximation to be taken [165]. The oscillations, which are typically approximated out in the Mølmer–Sørensen Hamiltonian, can be seen in the evolution of the matrix elements over the course of the gate time τ, depicted in Fig. 5.2a. All of the presented simulations were solved using density matrix formalism.

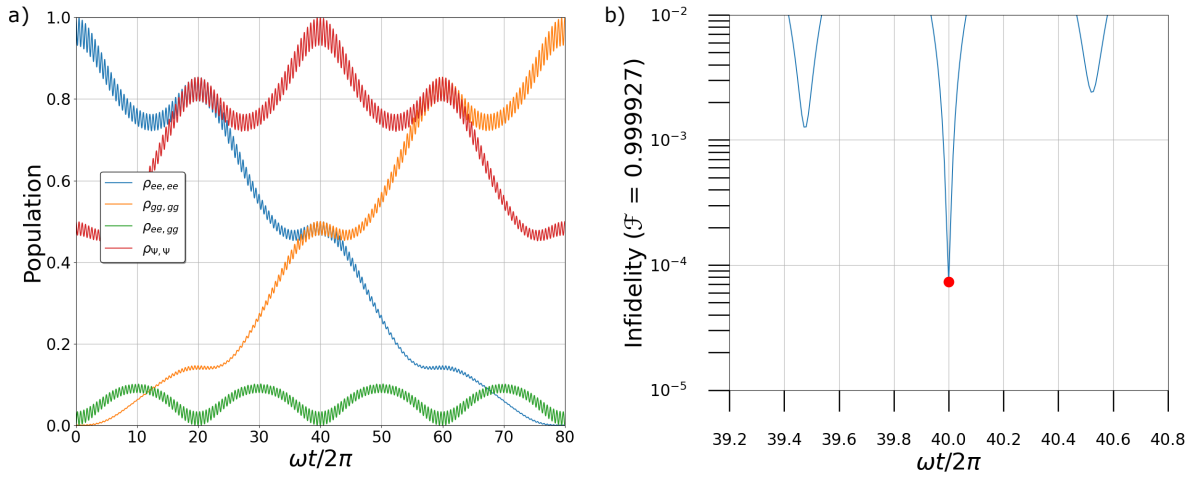


Figure 5.2: a) Simulated evolution of the matrix elements calculated for a two-ion chain, interacting with a single motional mode ($\omega = 1000000 \cdot 2\pi$ Hz) as described by Eq. 5.5. A total of 20 Fock states were used to simulate the motional modes with $\bar{n} = 0$. The parameters are presented in Table 5.1. b) Calculated Bell state infidelity, occurring at $\omega\tau/2\pi \approx 40$ during application of the Mølmer–Sørensen gate.

The evolution of the system presented in Fig. 5.2 matches qualitatively with the evolution presented in previous work [165]. A quantitative comparison of the calculated fidelities is presented in Fig. 5.3. For evaluating gate fidelities with trapped ions, it is common to consider the Bell-state fidelity [165, 162], which in this case occurs at $t = \tau \approx 40$ μs. The Bell-state fidelity for this two ion example is calculated by first finding the density matrices corresponding to the spin ρ_s and motional ρ_m subspaces. We only care about the spin states, so once the simulation is complete, the motional states are traced out and the density matrix for the motional states reduces to the identity, $\rho_m = I_m$, in order to calculate the different matrix elements for the spin states. The density matrix corresponding to the maximally entangled state for the two ions is given by

$$\rho_s = |\Psi_B\rangle \langle\Psi_B| = \frac{(|gg\rangle + i\,|ee\rangle) \otimes (\langle gg| - i\,\langle ee|)}{2} \tag{5.6}$$

The fidelity $\mathcal{F}$ can then be calculated at each time step if the total density matrix ρ is known by tracing out the motional subspace, and projecting the spin subspace onto the chosen Bell-state,

$$\mathcal{F} = \mathrm{tr}(\rho_s \otimes \rho_m \cdot \rho) \tag{5.7}$$

We want the motion to return to the original state, which is the ground state in the case, at the end of the gate, otherwise any population left in higher Fock states will directly impact the fidelity of the gate. The parameters used to calculate the evolution in Fig. 5.2 are listed in Table 5.1.

Parameter	Value
Ω	$89400 \cdot 2\pi$ Hz
ω	$1000000 \cdot 2\pi$ Hz
μ	$950000 \cdot 2\pi$ Hz
η	0.1
$\overline{n} = \phi_r = \phi_b$	0

Table 5.1: The set of parameters used in the simulations for generating Fig. 5.2. These parameters were also used for generating Fig. 5.3, except the Rabi frequency Ω was varied. A global phase was not considered.

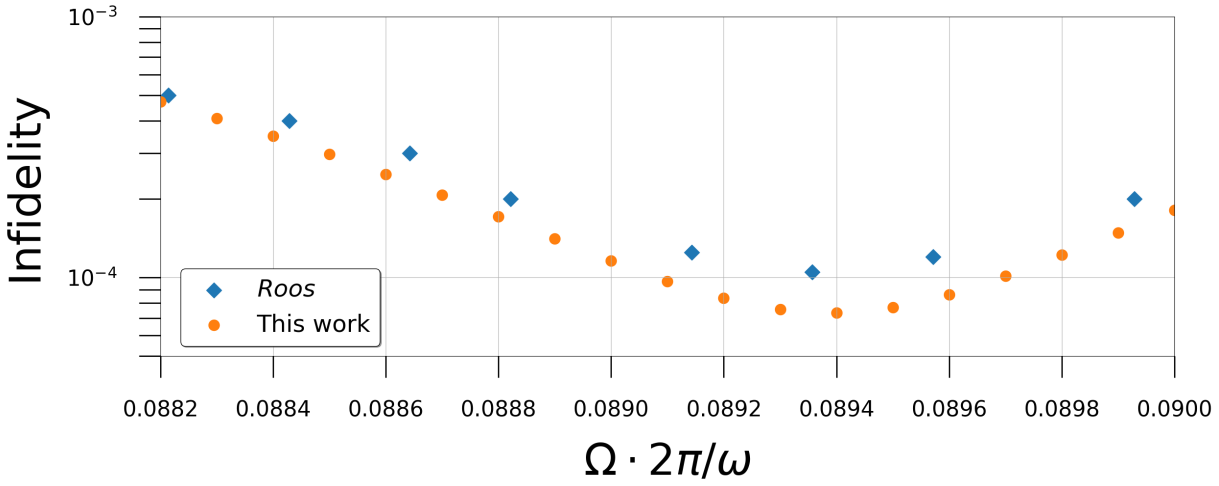


Figure 5.3: Infidelity as a function of the ratio $\Omega \cdot 2\pi/\omega$. Only a careful choice of parameters for the Rabi frequency Ω based on the single motional mode ω in this case will yield the maximum obtainable fidelity. The values in blue are estimated visually [165] and compared to the values in orange, which were calculated in this thesis. The simulations assumed $\bar{n} = 0$ for the single motional mode.

In order to make further comparisons, the infidelity was plotted as a function of the Rabi frequency to motional mode ratio in Fig. 5.3. The maximum fidelity ratio shows excellent agreement with the previous work [165]. This simple example shows there is a working piece of code that can faithfully replicate results, which gives us confidence when we want to introduce new parameters and a slightly different Hamiltonian in order to search for pulse-shaping schemes that will enable entanglement in longer chains of ions with more motional modes.

5.3 Mølmer–Sørensen Hamiltonian Simulations

The next Hamiltonian that will be considered is the well-known Mølmer–Sørensen Hamiltonian, governed by Eq. 5.9. This Hamiltonian is similar to Eq. 5.5, but the Mølmer–Sørensen Hamiltonian has more simplifying assumptions. Most importantly it assumes that the ions are in the Lamb-Dicke regime [166], meaning that changes to the internal electronic state of the ion is unlikely to excite the motional state by more than a single quanta n. The criterion that defines the Lamb-Dicke regime is:

$$\eta^2(2n+1) \ll 1 \tag{5.8}$$

To be in this regime, it is also assumed that the motion of the ion acts as a harmonic oscillator and that the vibrational states of this harmonic oscillator are spaced much farther than the energy of the laser and ion interaction. Furthermore the ions must be tightly confined such that the wavelength of the light interacting with the ions is considerably longer than the ions motion $\omega \ll \lambda/2\pi$.

Take a relatively large Lamb-Dicke parameter, say $\eta = 0.1$, for a specific ion and specific motional mode, this means that the internal spin state and the motional state are strongly coupled. The Lamb-Dicke approximation allows the Lamb-Dicke parameter η to be taken out of the exponential in Eq. 5.5. When applying the Mølmer–Sørensen gate the ion must be far within the Lamb-Dicke regime since it cannot be cooled while the gate is being applied.

Furthermore, it is assumed that we are operating in a regime where the sidebands from the ion motion can be resolved and that we are ignoring carrier transition, meaning $\Omega \ll \mu$. With this demonstration, we are considering the case of two ions and a single mode as was the case in Section 5.2, the only difference is the Hamiltonian that is being solved,

$$H_R = \sum_{i=1}^{2} \frac{\hbar\eta\Omega}{2}(e^{i(\mu-\phi_m^i)t} + e^{-i(\mu-\phi_m^i)t})(e^{-i\phi_s^i}\sigma_+ + e^{i\phi_s^i}\sigma_-)(ae^{-i\omega t} + a^\dagger e^{i\omega t}) \tag{5.9}$$

$$\phi_s = \frac{\phi_b + \phi_r}{2} \qquad \phi_m = \frac{\phi_b - \phi_r}{2} \tag{5.10}$$

Again, in this section, there is no pulse-shaping or amplitude modulation, but this section aims to build more intuition about the parameters that will be manipulated in the three chain examples. The ions are assumed to be in the motional ground state $\overline{n} = 0$ and that the motional phase $\phi_m = 0$ and the spin phases $\phi_s = 0$.

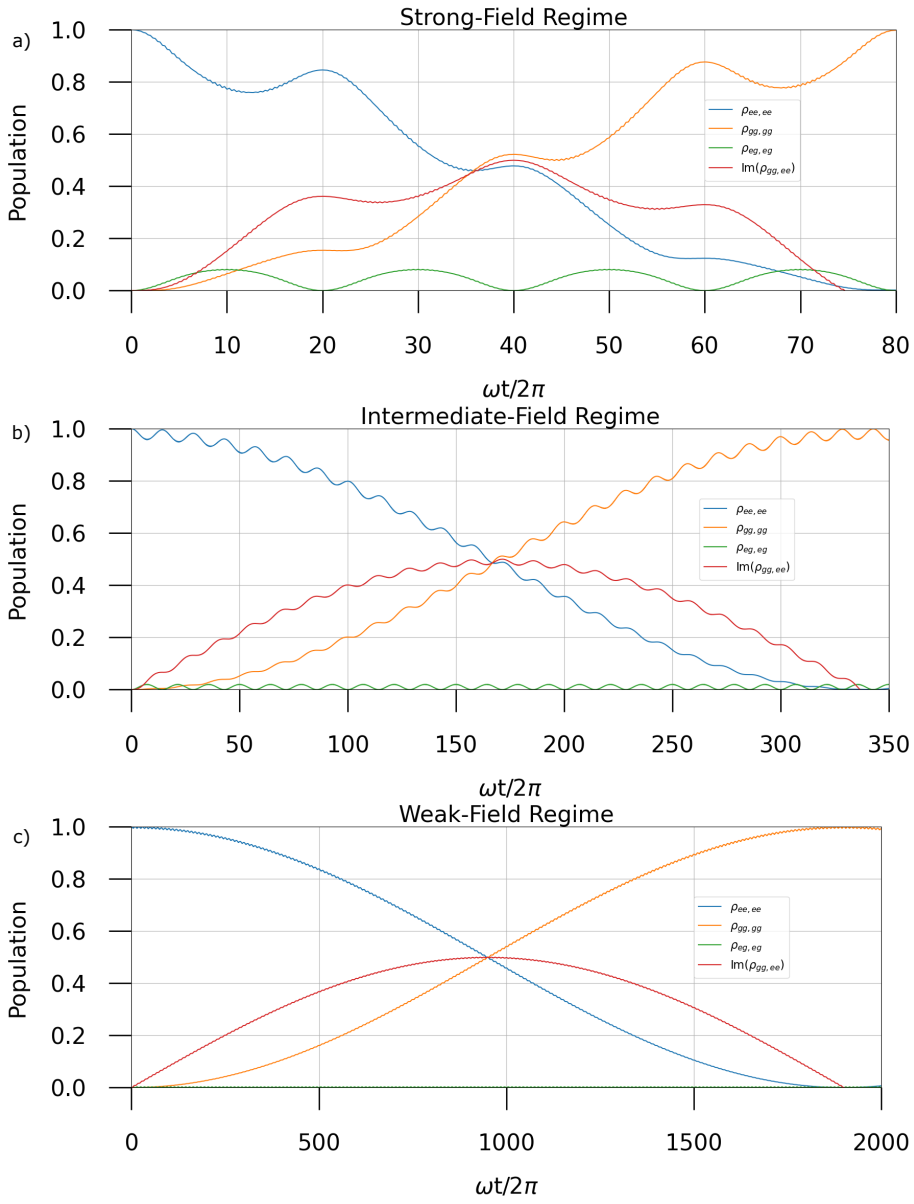


Figure 5.4: a) Time evolution of a two-spin system sharing a single motional mode ($\omega = 2000000 \cdot 2\pi$ Hz) using the Mølmer–Sørensen Hamiltonian 5.9 in a strong-field regime, where the motion is entangled with the internal spin state of the ions. b) Time evolution of a two-spin system sharing a single motional mode in an intermediate regime, where the gate is not entirely insensitive to fluctuations in the motion of the ions. c) Time evolution of a two-spin system in an insensitive weak-field regime, where $\eta\Omega \ll \omega - \mu$.

Parameter	SF Regime	IF Regime	WF Regime
Ω	$354000 \cdot 2\pi$ Hz	$200000 \cdot 2\pi$ Hz	$100000 \cdot 2\pi$ Hz
ω	$2000000 \cdot 2\pi$ Hz	$2000000 \cdot 2\pi$ Hz	$2000000 \cdot 2\pi$ Hz
μ	$1900000 \cdot 2\pi$ Hz	$1860000 \cdot 2\pi$ Hz	$1800000 \cdot 2\pi$ Hz
η	0.1	0.1	0.1
Ω/ω	0.177	0.1	0.05
μ/ω	0.95	0.93	0.9
$\eta\Omega/(\omega-\mu)$	≈ 0.354	≈ 0.143	≈ 0.050

Table 5.2: The set of parameters used in the simulations for generating Fig. 5.4. Ratios of the parameters are also presented in order to create intuition about the different regimes in which this gate can be operated.

The evolution of two spin states in different ions coupled with a single motional mode is described by Fig. 5.4, with the parameters dictating which regime that the gate is operating in. The coupling to the motional modes is evident in Fig. 5.4a, but these fluctuations became less evident as the Rabi frequency strength decreases and the detuning is set farther from the motional modes, like in Fig. 5.4c. Operating in the strong field regime has an advantage in that it allows faster gates because the amount of geometric phase between two spins to create a maximally entangled state can be acquired more quickly. However, the phase-space trajectories need to be closed in order for the the motion and spin to no longer be entangled at the end of the gate. In the weak field regime, the phase-space trajectories can be approximated as small circles about the origin and there is no real need to consider de-coupling the spin and the motion.

5.3.1 Double-Sideband Amplitude Modulation

In this section, an approach for creating amplitude-modulated pulse-shapes that can drive high-fidelity entangling gate operations in long chains of ions is presented. The rest of the simulations are done with a three ion chain, but there is no fundamental reason why this approach cannot be adapted to long chains of ions, say to chains with five or more ions. For full density matrix simulations, it is necessary to keep the Hilbert space small, which is why a three ion chain is chosen. With this many ions, modulation is necessary, but a full density matrix approach can still be utilized. The Hamiltonian simulations serve to validate the optimized amplitude modulation schemes. Optimization of these parameters are described further in the chapter, but first consider the case of three ions and three modes, described by the Mølmer–Sørensen Hamiltonian in Eq. 5.11,

$$H_{MS} = \sum_{i,j=1}^{3} \frac{\hbar\eta_{ij}\Omega(t)}{2}(e^{i(\mu-\phi_m^i)t} + e^{-i(\mu-\phi_m^i)t})(e^{-i\phi_s^i}\sigma_+^i + e^{i\phi_s^i}\sigma_-^i)(a_j e^{-i\omega_j t} + a_j^\dagger e^{i\omega_j t}) \quad (5.11)$$

The unitary evolution operator associated with this specific Hamiltonian can be described by,

$$U_{MS}(t) = e^{-iH_{MS}t/\hbar} \quad (5.12)$$

Where the exponential of the unitary can be presented using the Magnus expansion [167]. This allows the unitary to take a simpler form, giving specific parameters for which we can then optimize pulse-shapes.

$$U_{MS}(t) = e^{\zeta(t)} \quad (5.13)$$

$$\zeta(t) = \sum_{i=1}^{n} \zeta_n(t) = \zeta_1(t) + \zeta_2(t) + \ldots + \zeta_n(t) \quad (5.14)$$

We only consider the first two terms of the Magnus Expansion as the rest of the terms go to zero. Solving the first term of the expansion ζ_1 for an arbitrary number of ions n and motional modes, we can break down the term into a sum of two single integrals. For these simulations the spin ϕ_s and motional ϕ_m were set to zero. The first term, ζ_1, can be shown to be computed as [156],

$$\begin{aligned} \zeta_1(t) &= \frac{-i}{\hbar}\int_0^t H_{MS}(t_1)\,dt_1 \\ &= \sum_{i,j=1}^{n} \sigma_x^i \left[\alpha_{ij}(t)a_j^\dagger - \alpha_{ij}^*(t)a_j\right] \end{aligned} \quad (5.15)$$

Where a standard integral $\alpha_{ij}(t)$ is defined in order to simplify the expression and be utilized as a tool for tracking and optimizing the spins in phase-space.

$$\alpha_{ij}(t) = \frac{-i\eta_{ij}}{2}\int_0^\tau \Omega(t)(e^{i\mu t} - e^{-i\mu t})e^{i\omega_j t}\,dt \quad (5.16)$$

Eq. 5.16 is solved for each time step leading up to the gate time τ and the imaginary $Im(\alpha_{ij}(t))$ and real $Re(\alpha_{ij}(t))$ parts are plotted as coordinates in phase-space as shown in the following figures. In order to simplify the second term ζ_2, a similar process can be followed [156]. We start with just the commutator $[H_{MS}(t_1), H_{MS}(t_2)]$ first and again assume all phases are zero for arbitrary ions and modes. Using the relationships between operators like $[a_j, a_j^\dagger] = 1$, and common identities we can reduce the expression,

$$\begin{aligned}\zeta_2(t) &= \frac{-1}{2\hbar^2}\int_0^t dt_1 \int_0^{t_1} dt_2 \left[H_{MS}(t_1), H_{MS}(t_2)\right] \\ &= i\int_0^t dt_1 \int_0^{t_1} dt_2 \sum_{i,j,l=1}^{n} \hbar^2 \eta_{ij}\eta_{lj}\Omega(t_1)\Omega(t_2)\sigma_x^i\sigma_x^l \cos(\mu t_1)\cos(\mu t_2)\sin\big(\omega_j(t_2-t_1)\big)\end{aligned} \tag{5.17}$$

Where another useful integral is typically defined, which will be another function that will be optimized for pulse shaping,

$$\chi(t) = \int_0^\tau \int_0^{t_2} dt_2 dt_1 \Omega(t_2)\Omega(t_1)\sin\left(\left(t_2 - t_1\right)\omega_j\right)\cos\left(\mu t_2\right)\cos\left(\mu t_1\right) \tag{5.18}$$

For an arbitrary chain of ions i and motional modes j, the unitary operator describes the evolution of the system,

$$U_{MS}(t) = \exp\left[\sum_{i,j=1}^{n} \alpha_{ij}(t)a_j^\dagger - \alpha_{ij}^*(t)a_j + i\sum_{i,l=1}^{n}\sigma_x^i\sigma_x^l\chi_{i,l}(t)\right] \tag{5.19}$$

With the correct choice of pulse-shaping parameters, this unitary can reduce to the desired spin-spin interaction, as long as $\alpha_{i,j}(t) \to 0$ for all ions i and modes j and $\chi_{i,l}(t) \to \pi/4$ for all ion pairs i, l,

$$U_{MS}(t) \approx \exp\left[i\frac{\pi}{4}\sigma^1\sigma^2\right] \tag{5.20}$$

Meeting these two criteria for the $\alpha(t)$ and $\chi(t)$ integrals is the main challenge associated with pulse-shaping. In general, amplitude modulation was first outlined a decade ago [154], where the primary solutions boil down to solving an eigenvalue problem, which will give a segmented amplitude-modulated pulse shape [156]. This method has proven incredibly

successful and has been widely adopted [160, 163], however, there may be a more intuitive way to approach the problem by using continuous functions that already exist in signal processing [168]. Common functions include carrier signals modulated by one or more sidebands for the purpose of reducing power consumption and prevent frequency crowding [169]. This simplifies the optimization problem to finding just a few parameters that will work for arbitrary ion pairs in a chain, instead of finding an optimal pulse shape for each unique ion pair. To this end, we assume a double-sideband amplitude modulated functional form of the Rabi frequency $\Omega(t)$ given by,

$$\Omega(t) = \Omega_0 \sin\left(\omega_c t\pi/\tau\right) + \frac{m\Omega_0}{2}\sin\left(\left(\omega_c + \omega_s\right)t\pi/\tau + \pi\right) + \frac{m\Omega_0}{2}\sin\left(\left(\omega_c - \omega_s\right)t\pi/\tau - \pi\right) \tag{5.21}$$

The goal in this case will be to search for parameters; μ, ω_c, and ω_s, such that all phase-space trajectories close simultaneously for every spin with each mode and then find a single parameter Ω_o for each ion pair that will scale the phase-space accordingly. The carrier frequency and sideband frequency are chosen such that the wave-packet, or envelope, is an integer multiple of the gate time τ, by multiplying the frequency by a scaling factor π/τ. It will be shown, that ideally, the amplitude approaches zero at the end of the gate, so integer multiples are more desired than half-integer multiples. In the following cases, the modulation index $m = 0$. Assuming this form of Rabi frequency, α_{ij} can now be solved numerically or an analytical function is provided in Appendix C.2.

The need for modulation techniques for ion chains of at least three ions is best highlighted with a simple geometric optical phase-space argument. When spin-motion entanglement is driven by a constant pulse, where all of the experimental parameters such as Ω_o, μ, and $\phi_{r/b}$ are time independent, then the phase-space trajectory can be described as a circle. Depending on the gate time τ, the trajectory can loop a single time or many times around this circle. The area of the circle $A \propto \eta\Omega_o$ and is dependant on how close the detuning μ parameter is to the motional mode in question. If μ is tuned close to the motional mode ω than the the area drawn out in phase-space is much larger. For the case of two ions, modulation is not necessary because μ can be parked in between the two motional modes, so that all of the phase-space trajectories complete an entire rotation at the same time (albeit traced in opposite directions). If there are three motional modes, like in the case with three ions, the detuning parameter cannot be parked equally away from all three modes, dictating that modulation of some form take place. This failure to close the phase-space trajectories for the case of three ions is further highlighted in Fig. 5.5.

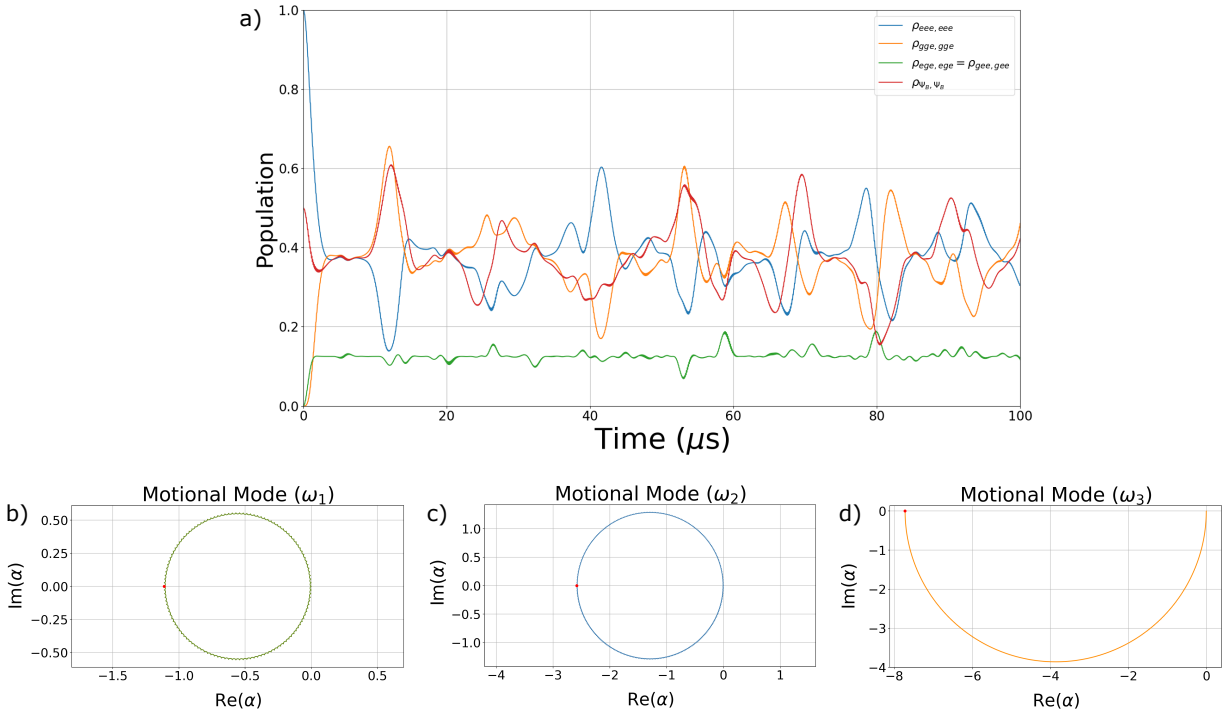


Figure 5.5: a) Matrix element evolution using assuming a constant Rabi frequency creating spin-motion entanglement in a chain of three ions. This demonstrates it is not possible to disentangle the spin from the motion without modulation of either the amplitude, frequency, or phase of the pulse. b-d) Phase-space trajectories for the three motional modes, showing that the spin and motion remain entangled at the end of the pulse.

In the following simulations, it is demonstrated that a carrier signal, modulated with two sidebands can readily be used to create high-fidelity entangling gates in a chain of three ions. The form of the Rabi frequency follows that of Eq. 5.21, in which double-sided amplitude modulation is employed (DSAM). Given that acousto-optical modulators (AOM) are typically the physical mechanism for how these amplitude modulated pulse-shaped are created, which operate at $\sim$ 200 MHz, there is no reason that this functional form could not be implemented in a laboratory with standard hardware.

The current process for finding a suitable pulse-shape is as follows:

1. Identify modulation parameters such as ω_c, ω_{sb}, and m. These parameters must be feasibly implemented. These simulation assume a relatively fast 50 μs gate.

2. Minimize α_{ij} for each ion i and mode j such that all phase-space trajectories are closed. This is done with python functions such as *scipy.optimize.minimize*.

3. Scale the maximum Rabi frequency Ω_o by numerically integrating $\chi_{i,l}(t)$ such that $\chi_{i,l}(t) \approx \pi/4$. Again, a minimization function is used in this situation.

4. Check the optimized parameters by solving the von Neumann Eq. 5.4 with the Mølmer–Sørensen Hamiltonian for three ions using density matrix formalism and find the Bell-state fidelity.

The parameters for the results presented in Fig. 5.6, Fig. 5.7, and Fig. 5.8, are listed in Table 5.3. All three of the motional modes for these three examples were the same ($\omega_1 = 4.34 \cdot 2\pi$ MHz, $\omega_2 = 4.38 \cdot 2\pi$ MHz, $\omega_3 = 4.4 \cdot 2\pi$ MHz [156]), detuning ($\mu = 4.41 \cdot 2\pi$ MHz), as were the Lamb-Dicke parameters ($\eta_{ij} = \eta = 0.1$), and the gate times $\tau = 50$ μs. The Lamb-Dicke parameters are treated as a constant in order to simplify the simulations since they just essentially scale the phase-space trajectories. The maximum Rabi frequency Ω_o was slightly modified for each example to account for differences in geometric phase accumulation due to the change in sideband frequency ω_{sb}.

Parameter	Fig. 5.6	Fig. 5.7	Fig. 5.8
Ω_o	$772050 \cdot 2\pi$ Hz	$773299 \cdot 2\pi$ Hz	$771185 \cdot 2\pi$ Hz
$\omega_{sb}\pi/\tau$	$10000 \cdot 2\pi$ Hz	$20000 \cdot 2\pi$ Hz	$40000 \cdot 2\pi$ Hz

Table 5.3: The set of parameters used in the simulations for DSAM entangling gates between pairs of ions in a three ion chain. The carrier signal frequency was kept the same at $\omega_c\pi/\tau = 375000 \cdot 2\pi$ Hz for all simulations.

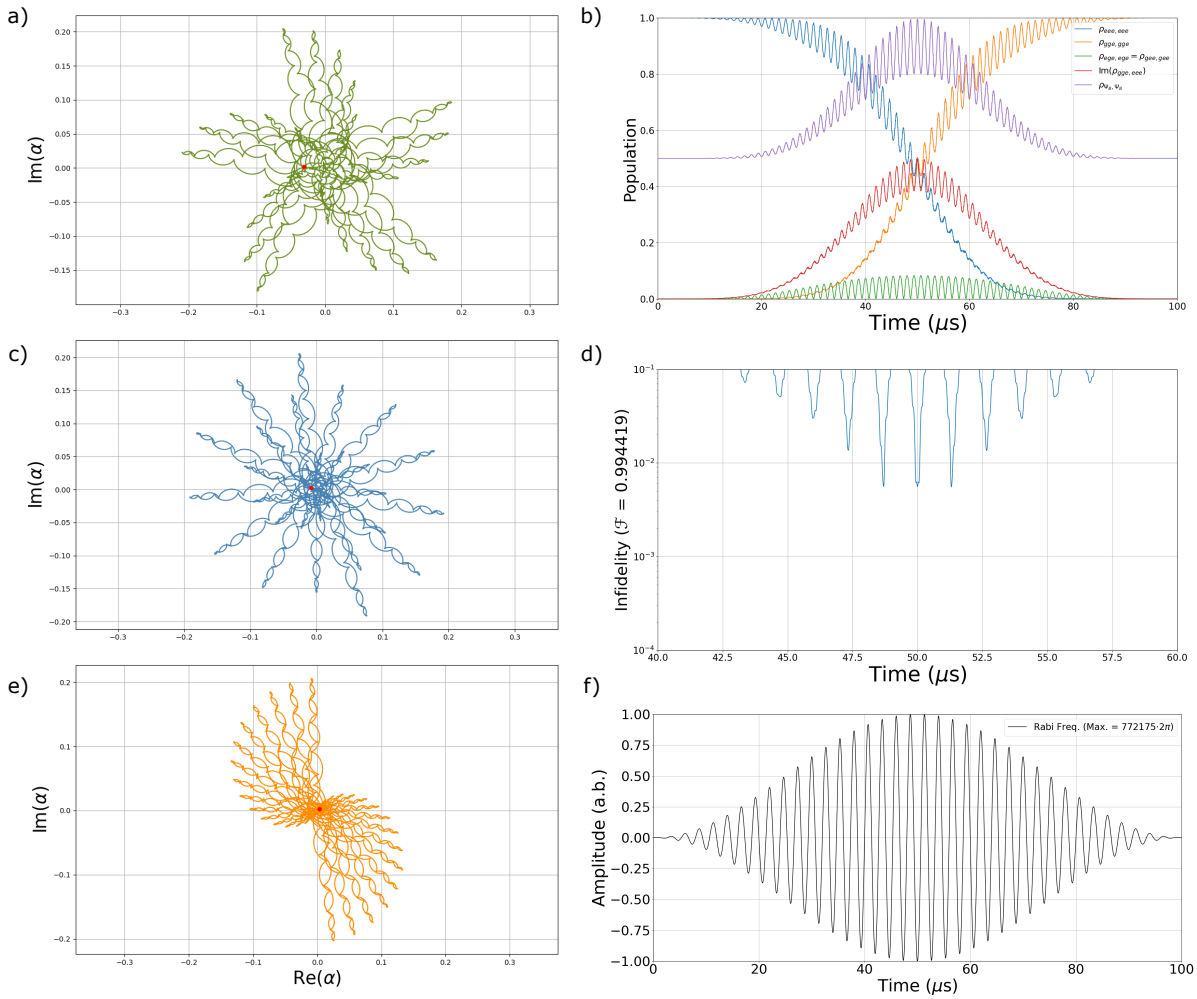


Figure 5.6: a) Phase-space trajectory of the coherent motional state α corresponding to the first motional mode, ω_1. Since the motional state has not returned to zero at the end of the gate, the spin and motion are still entangled. This shows up as errors in the Bell-state fidelity. b) Matrix element evolution as the gate is applied to the first two ions in the chain of three ions. c) Phase-space trajectory for the second motional mode, ω_2. d) Infidelity with respect to creation of a Bell-state. The fidelity is relatively low in this case because the gate ends in the middle of the pulse shape. e) Phase-space trajectory for the third motional mode, ω_3. f) Modulated Rabi frequency $\Omega(t)$ with the basic functional form described by Eq. 5.21 applied to the ions for the gate time $\tau = 50$ μs. This can be done in the lab by modulating the laser intensity with an acousto-optical modulator.

By using DSAM, the spin of the ion is increasingly pushed and pulled in phase-space over a time-averaged functional form in order to create the desired spin-spin interaction. The ion spin in phase-space is oscillating around the origin continuously so that perturbations in the Rabi frequency, detuning, or other important parameters can be averaged out if they occur on or at a faster rate than the gate time. The first example presented in Fig. 5.6 utilizes the first half of a single wave-packet to acquire geometric phase, with the gate time τ and the maximally entangled state occurring near the maximum Ω_o in the middle of the wave-packet. The phase-space trajectories in Fig. 5.6a, Fig. 5.6c, and Fig. 5.6e, clearly exhibit the imprint of the DSAM function used to drive the spin-motion entanglement, but do not fully close because the gate ends in the middle of the pulse shape. This failure to close the phase-space trajectories fully is reflected in the fidelities as well. In Fig. 5.6d, the Bell-state fidelity is plotted showing the error $\epsilon = 1 - \mathcal{F}$, where $\mathcal{F} = \langle \Psi_B | \rho | \Psi_B \rangle = (\rho_{eee,eee} + \rho_{gge,gge})/2 + Im(\rho_{gge,eee})$ [18]. This example highlights another key criteria of pulse-shaping, that $\Omega(t) \to 0$ as $t \to \tau$. In the situation, fidelities can be improved upon by ensuring that $\Omega(\tau) \approx 0$, as will be shown in the following examples. This extra criteria can be met by increasing the sideband frequency ω_{sb} by a factor of 2, as shown in Fig. 5.7.

This infidelity is improved in Fig. 5.7, where the sideband frequency is now doubled such that $\omega_{sb} = 2$. Now a single pulse (wave-packet) completes the transformation $|eee\rangle \to (|gge\rangle + i\,|eee\rangle)/2$ with a second pulse taking the final state to $|gge\rangle$ at $t = 2\tau$. With a single pulse modulating the ion spin-spin interaction over the course of the gate, high fidelity can be obtained numerically with $\epsilon \approx 3 \cdot 10^{-6}$. This is reflected in phase-space trajectories of Fig. 5.7, where closure has been successful. The ideal maximum Ω_o had to be scaled accordingly to account for differences in the phase-space trajectories using this slightly modified pulse-shape.

The example presented in Fig. 5.8 similarly shows phase-space trajectories for the three motional modes, but two wave-packets are utilized over the gate time instead of a single one by again increasing the sideband frequency such that $\omega_{sb} = 4$. An order of magnitude decrease in the Bell state fidelity is achieved when the sideband frequency is increased in this case. Again the Rabi frequency is optimized using a minimization function, but it is unclear if the order of magnitude decrease is from the increase in the sideband frequency or a lack of optimization of the Rabi frequency. The phase-space trajectories are closed and the error is $\epsilon \approx 2.3 \cdot 10^{-5}$.

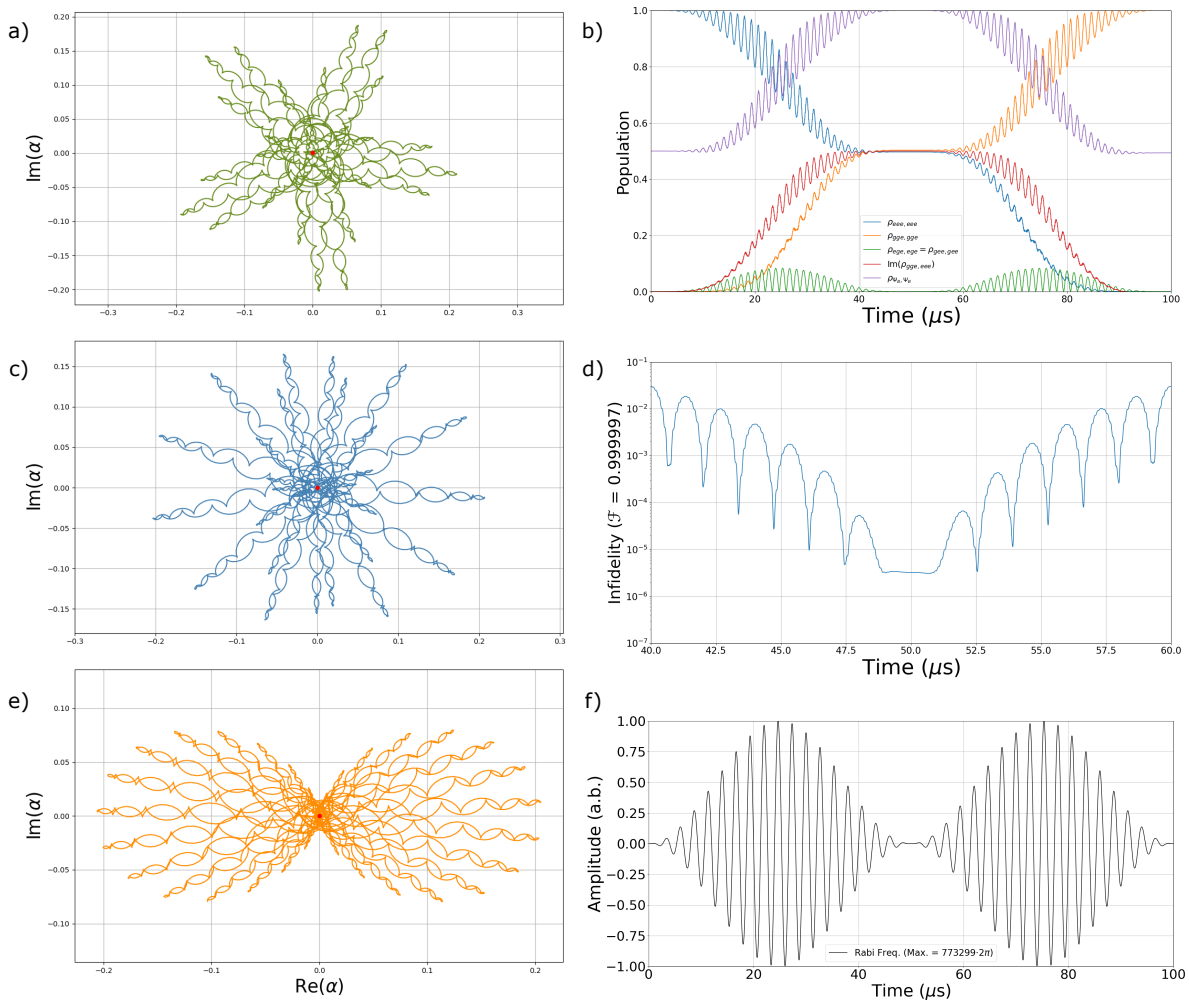


Figure 5.7: a) Phase-space trajectory of the coherent motional state corresponding to the first motional mode, ω_1. b) Matrix element evolution as the gate is applied to the first two ions in the chain of three ions. c) Phase-space trajectory for the second motional mode, ω_2. d) Infidelity with respect to creation of a Bell state. As the pulse is ramped down near $\tau \approx 50$ μs, the Bell state fidelity settles at high fidelity ~ 0.999997. e) Phase-space trajectory for the third motional mode, ω_3. f) Modulated Rabi frequency $\Omega(t)$ with the sideband frequency $\omega_s = 2$ for $t = [0, \tau]$. Two pulses are applied to complete a spin flip on the first two ions in the chain.

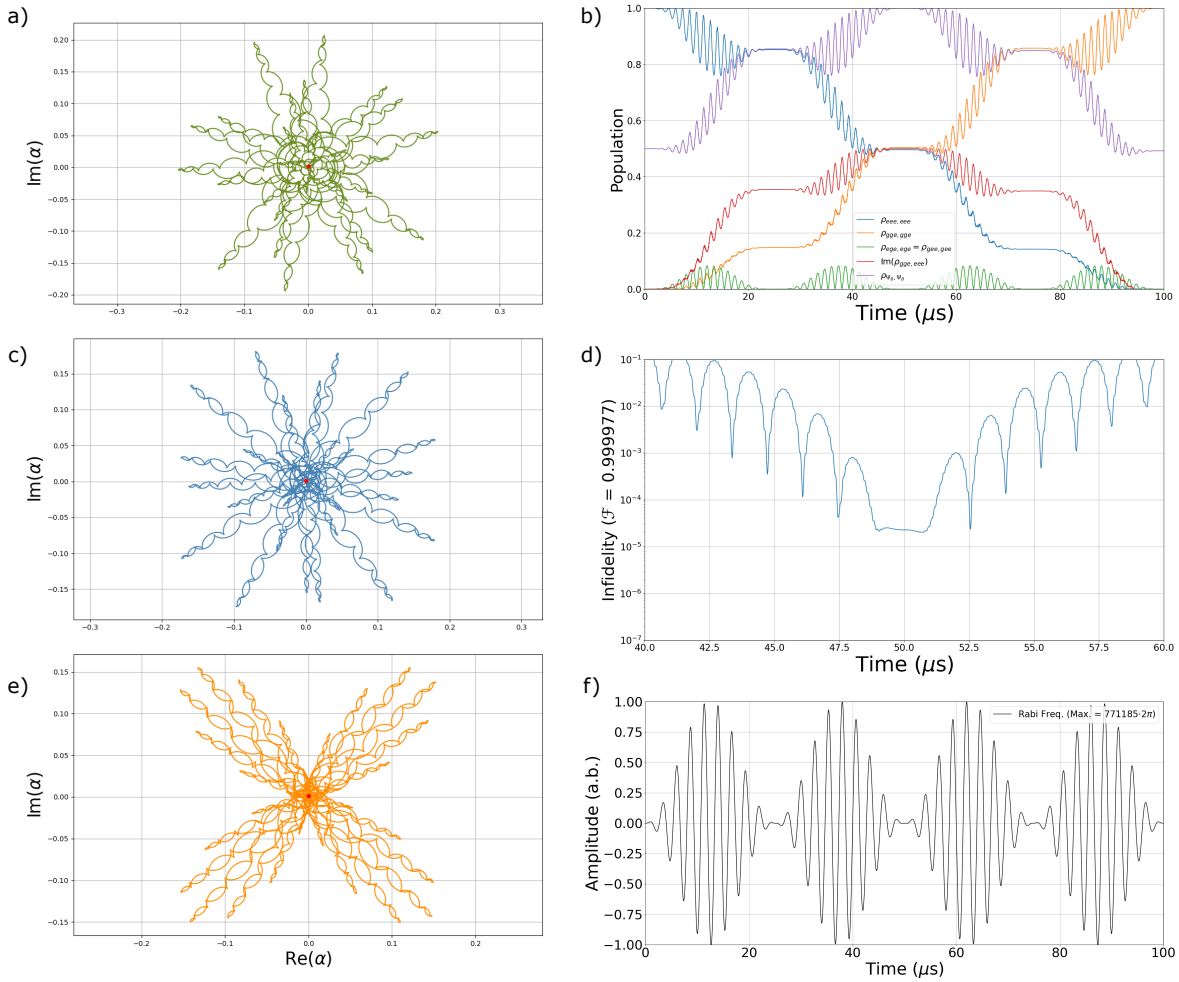


Figure 5.8: a, c, e) Phase-space trajectories of the coherent motional states α corresponding to the motional modes, ω_1, ω_2, and ω_3, respectively. The imaginary and real components of α are plotted. b) Matrix element evolution as the gate is applied to the first two ions in the chain of three ions. d) Infidelity with respect to creation of a Bell-state. The fidelity is ~ 0.999977. f) Modulated Rabi frequency $\Omega(t)$ with the sideband frequency $\omega_s = 4$.

A simplifying assumption that is made is that $\eta_{ij} = \eta = 0.1$ for all i, j. As shown in the last three examples, there are only three phase-space trajectories to be concerned with instead of nine, which would be the usual case with three ions. Regardless, the method described here can easily be adapted to more ions and phase-space trajectories. In Appendix C.3, an example of a five ion chain where all phase-space trajectories are closed simultaneously shows that even with 25 Lamb-Dicke parameters coupling all five ions independently to each motional mode that the method described here can still be used to decouple the internal states. This technique shows that a simple functional form can be used to create entanglement between arbitrary pairs of ions in a long chain, and that the only requirement is to then scale Ω_o, once the phase-space trajectories have been optimized.

Now that we have a method for creating high-fidelity entangling gates, it is time to turn attention to sources of error. This code base was written so that noise can easily be added to any of the parameters used in order to simulate laser intensity fluctuations [18], fluctuations of the motional modes due to electric field noise [170], static errors in the detuning or drifts [162], phase noise [171], and so on. The investigated errors sources are static detuning errors, motional mode fluctuations which can be caused by D.C. voltage noise, and laser intensity fluctuations, typically caused by power drifts from the laser or beam steering.

5.3.2 Detuning and Rabi Frequency Errors

A major source of error is detuning errors ϵ_δ, either due to drifts or improper calibrations [162]. Similarly, calibration of the Rabi frequency is an essential step in any trapped ion machine and Rabi frequency errors ϵ_Ω can be introduced into the system if the calibrations are not properly conducted or there has been a significant lapse of time between the last calibration routine [172]. Either of these errors can directly result in lower entangling gate fidelities. This section details static errors associated with the detuning parameter μ and the Rabi frequency Ω_o. The parameters used in this section are the same as in Fig. 5.7, except μ and Ω_o are intentionally changed from their optimized values in order to simulate slow drifts that are not calibration corrected that could occur in the lab over the course of a day or two. These errors are static in the sense that the parameters do not change over the course of the applied gate.

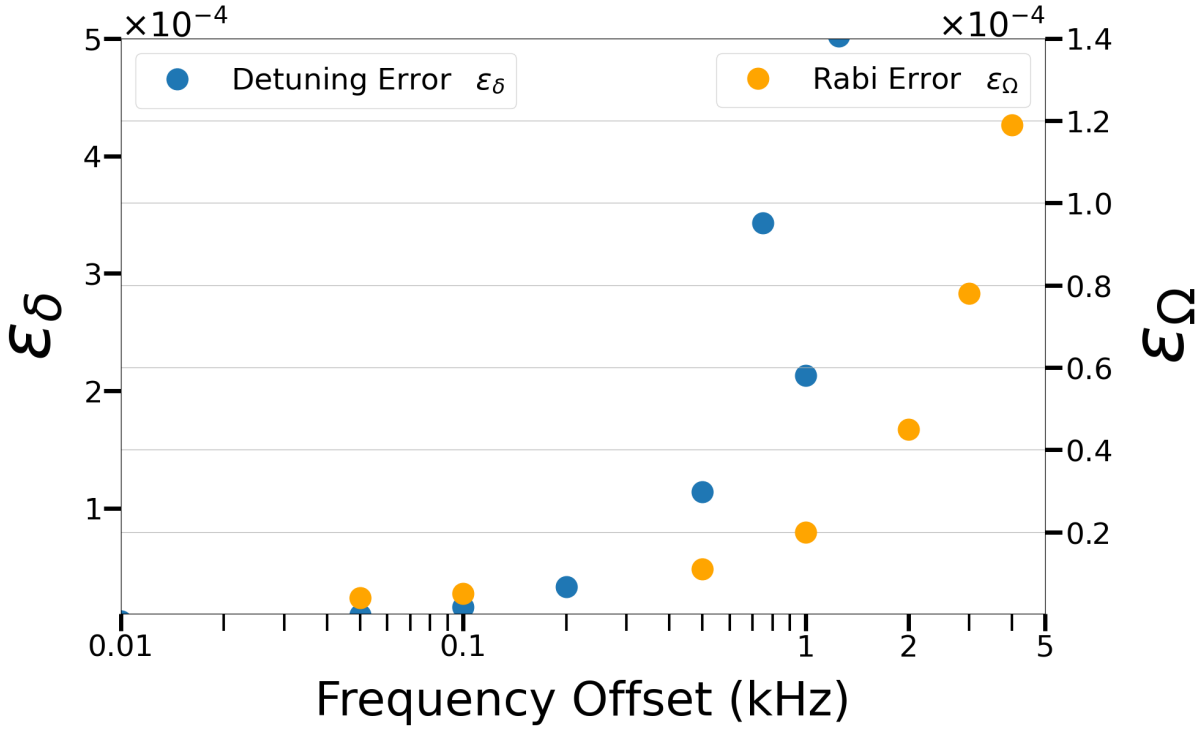


Figure 5.9: The left-hand axis (blue) plots the detuning error induced when the bichromatic light is tuned away from the optimal value of μ. Any detuning error > 2 Hz results in significant infidelity and the error is non-monotonic due to the presence of multiple motional modes [156]. The right-axis (gold) plots the Rabi error induced when the Rabi frequency is increased from the optimal value. The infidelity from the errors is calculated using the same parameters as in Fig. 5.7.

The error is plotted in Fig. 5.9. These simulations indicate that the amplitude modulation scheme described by Eq. 5.21 is considered "robust" to detuning errors when compared with previous results in literature [162], with errors at the $0.02 - 0.03\%$ level when μ is detuned ~ 1 kHz away from the optimal value. The simulations also show that modulation scheme is robust to Rabi frequency errors with only a 0.01% error when the Rabi frequency is ~ 3.5 kHz off-resonance. To achieve this in lab setting this would require stabilizing the Rabi frequency fluctuations to $3500 \cdot 2\pi/773300 \cdot 2\pi \approx 0.5\%$. These simulated results, where static errors are introduced, indicate that there is no intrinsic issue with a DSAM scheme for entangling ions.

5.3.3 Introducing Noise

In this section, instead of a static detuning error or Rabi frequency offset, noise is written onto the three motional modes of the ions. The study of electric field noise, which propagates to the secular motion of the ion, is of considerable interest with many sources being identified such as electromagnetic pick up and thermally activated fluctuators [170]. The simulations contained in this section do not take into account any specific type of noise, but simply assumes a Gaussian form for the motional frequencies. These two examples use the parameters from the previous section, but they instead take into account at each time step motional fluctuations following a Gaussian noise model described by Eq. 5.22,

$$\nu_{\zeta_n}(z) = \frac{1}{\sigma\sqrt{2\pi}} e^{-(z-\bar{x}_n)^2/(2\sigma^2)} \tag{5.22}$$

Where the mean frequency is $\bar{x}_n = \omega_n/2\pi = \nu_n$ for each motional mode, with $\nu_1 = 4.34$ MHz, $\nu_2 = 4.38$ MHz, and $\nu_3 = 4.4$ MHz. As the motional mode parameter is varied at each time step throughout the simulation based on Gaussian distributions like that shown in Fig. 5.10a, the fidelity decreases as the variation increases. The infidelity is calculated in Fig. 5.10b, as a function of the standard deviation used to generate the Gaussian vibrational frequency noise.

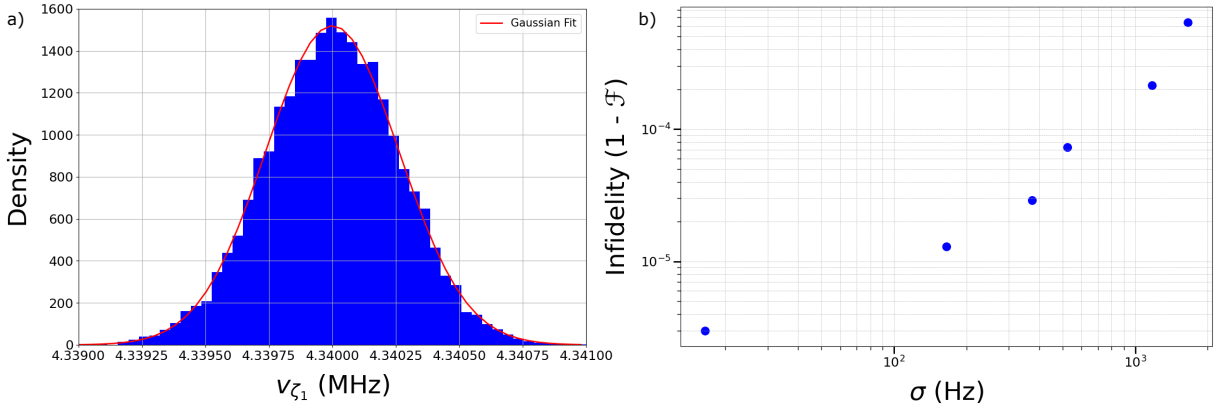


Figure 5.10: a) Example Gaussian distribution of the first motional mode that was generated in order to analyze the impact of variations in the motional frequency. Each new generated value for the first motional mode ν_{ζ_1} is used at a single time step in the simulations presented in Fig. 5.11. b) Infidelity as a function of the standard deviation in Eq. 5.22. For these secular frequencies, when $\sigma > 1$ kHz, significant error is introduced into the Bell state fidelities.

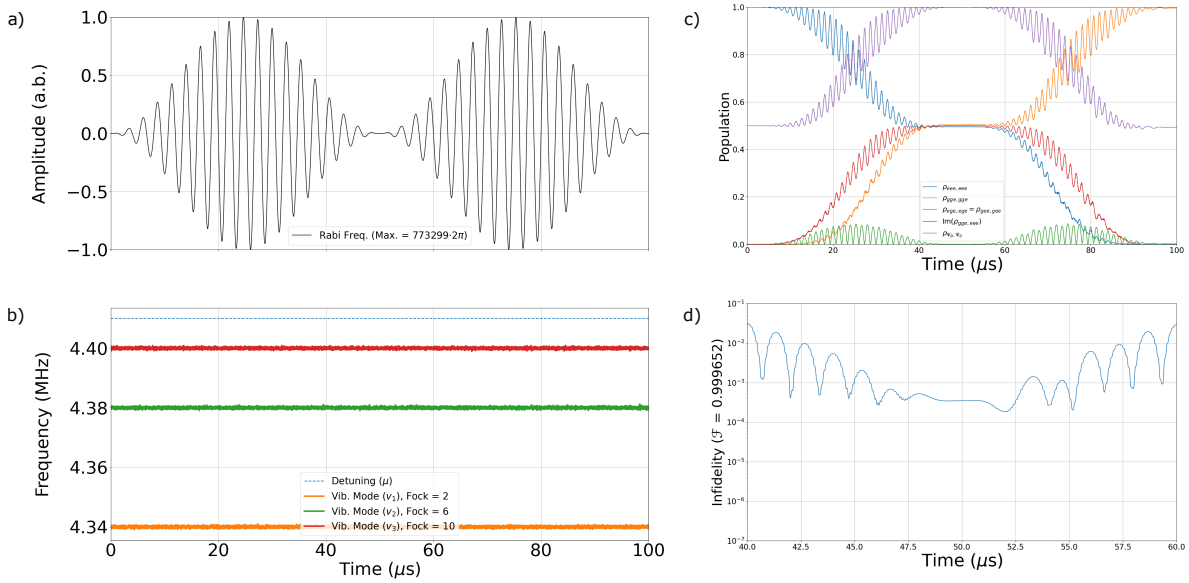


Figure 5.11: a) Rabi frequency profile used to drive the entangling gate, which is the same as the profile used in 5.6. b) Vibrational motional modes used in the simulation for the chain of three ions. More Fock states are used for motional modes closer to the detuning μ because the higher Fock states become populated more easily. At each solution step in the simulation, Gaussian noise is introduced into the motional modes to simulate perturbations from stray electric fields. The detuning parameter μ is denoted by the dashed blue line above the motional mode frequencies. c) Matrix element evolution with a final fidelity $\left|\langle\Psi|gge\rangle\right|^2 = 0.995833$. d) Corresponding Bell state infidelity curve with fidelity $\mathcal{F} = 0.999652$ when $\sigma \approx 1.66$ kHz.

Fig. 5.11 shows the evolution of the relevant matrix elements in the three ion chain as the motional modes are disrupted by a noise source. The motional mode frequencies used in the simulation have visible noise in Fig. 5.11b, ultimately reducing the fidelity by two orders of magnitude compared with static motional frequencies used in previous simulations. Fig. 5.12 shows a similar simulation, but $\omega_{sb} = 8$ in this case. With each noise simulation, whether static or dynamic, the sideband frequency ω_{sb} has no noticeable impact on the introduced errors, assuming that ω_{sb} is set such that $\Omega(t) \to 0$ as $t \to \tau$.

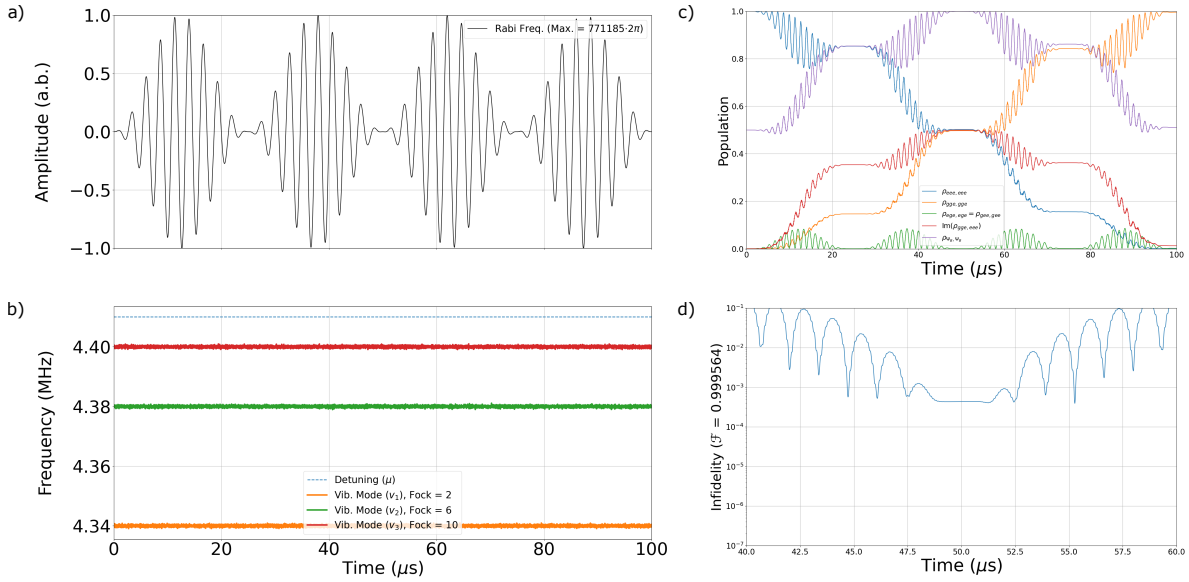


Figure 5.12: a) Rabi frequency profile used to drive the entangling gate, which is the same as the profile used in 5.7. b) Vibrational motional modes used in the simulation for the chain of three ions, assuming Gaussian electric field noise. c) Matrix element evolution with a final state fidelity $\left|\langle\Psi|eeg\rangle\right|^2 = 0.997384$. d) Corresponding Bell state infidelity curve with fidelity $\mathcal{F} = 0.999564$ when $\sigma \approx 1.66$ kHz.

The heating rate of a trapped ion $\Gamma_{\dot{\bar{n}}}$ can be related to the spectral density of the electric field noise $S_E(\omega_\zeta)$ such that $\Gamma_{\dot{\bar{n}}} \approx \frac{e^2}{4m\hbar\omega_\zeta} S_E(\omega_\zeta)$ [170], but this would require modification to Eq. 5.4 and is beyond the scope of this work since the initial goal of these simulations is to evaluate Eq. 5.21 for amplitude modulated entangling gates in chains of ions.

Gaussian noise influencing the Rabi frequency is also evaluated in a similar manner as in Fig. 5.13. The Rabi frequency $\Omega(t)$ in these cased was varied at each time step following a Gaussian distribution such that $\sigma_r = 0.05 \cdot \Omega_o$. In this case, the Bell state fidelity again was decreased by roughly two orders of magnitude compared with the previous simulations. The two-photon Rabi frequency is related to the intensity of the laser of the two beams driving the Raman transition such as $\Omega(t) \propto \sqrt{I_1 I_0}$. This example further demonstrates the flexibility of the code, which has the ability to tease out the impact of different error sources on the Bell state fidelity.

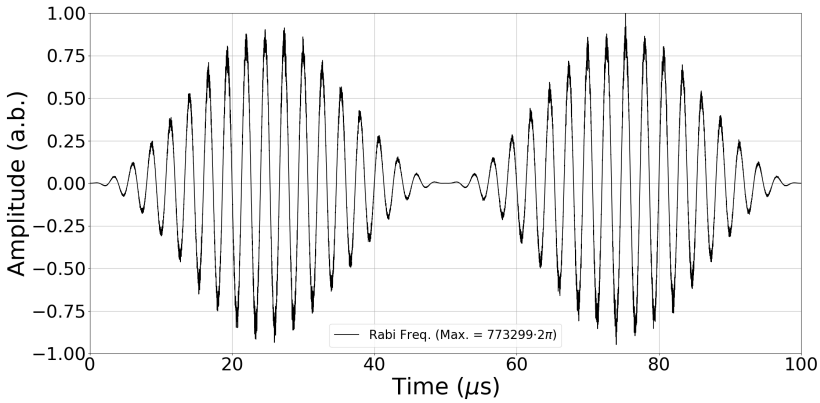


Figure 5.13: Rabi frequency profile used to drive an entangling gate, with Gaussian noise introduced to simulate laser intensity fluctuations. All other parameters are the same as those used in Fig. 5.7. The Bell-state fidelity was calculated to be $\mathcal{F} = 0.999711$ and a final fidelity of $\left|\langle\Psi|gge\rangle\right|^2 = 0.999568$.

5.4 Outlook

A specific pulse-shape, formed from a carrier signal modulated with two sidebands, was investigated for driving entangling gates between pairs of ions in chains with length $N > 2$. The amplitude modulation scheme utilizes a continuous waveform throughout the gate operation and relies on modifying only a few parameters; such as the driving carrier signal ω_c or the sideband signal ω_{sb}, in contrast to other pulse-shaping schemes which require finding $2N + 1$ pulse segments for each unique ion pair [154]. This simple and modest modulation scheme, taken from standard signal processing techniques [168], is shown to be capable of simultaneously decoupling every motional mode from each ions' spin in at least a chain of five ions with a proper choice of detuning. The pulse shapes are capable of being created with arbitrary waveform generators, which can modulate laser beams using AOMs for implementing this scheme in chains of Ba^+ ions. The trapped ion platform described in Section 4 has been designed to have the capability of implementing this amplitude-modulation scheme, which can be a direction for future work.

The presented modulation scheme relies on optimization of the detuning and Rabi frequency, which is done by solving the $\alpha(t)$ and $\chi(t)$ integrals from the unitary evolution operator for the Mølmer–Sørensen Hamiltonian in conjunction with standard Python minimization packages. This optimization is necessary for closing and scaling phase-space

trajectories of ion spins interacting with their collective motional modes. These optimized parameters are then verified by solving the von Neumann equation for the Mølmer–Sørensen Hamiltonian using density matrix formalism for the case of three ions in order to calculate and ensure a high Bell state fidelity with $\epsilon \sim 1 \cdot 10^{-5}$. Both static and dynamic errors were also introduced into the simulations as a method for evaluating the pulse shaping schemes ability to handle errors. No obvious sensitivity to a specific error type was found and in general the impact that the errors had on the fidelity were similar to what was found in previous studies [162]. The code used to simulate the three ion example is readily adaptable for larger simulations of longer ion chains, such as five ions, but solving Hilbert spaces larger than fives ions, even with the use of sparse matrices, is not easily achieved. Verification of optimized parameters in longer chains of ions would require an alternative approach such as extrapolation from what has been calculated and verified in shorter ion chains.

Future simulation work, extending this pulse shaping scheme, could be to investigate the impact that the carrier frequency ω_c has on the calculated errors. An additional extension could also be to solve the Lindblad master equation (instead of the von Neumann equation) in order to take into account effects such as motional heating of the ions [170] since motional heating can be tied to electric field noise [173]. Another approach for extending this work could be to utilize other well-known functional forms from signal processing such as the Blackman function [168, 169] and study their feasibility for creating entanglement between pairs of trapped ions in long chains. Finally, amplitude modulated schemes are often paired with frequency modulation schemes as a technique to further mitigate errors [160, 161].

Chapter 6

Conclusion

The results in this thesis are focused on easing the trapping of long chains of Ba^+ ions, with a specific concentration on the $^{133}Ba^+$ isotope. This problem was attacked by first examining different plausible photoionization schemes that could be used for the isotope-selective loading of barium, and for the specific case of $^{133}Ba^+$, different methods of fabrication were investigated for creating reliable ablation targets from microgram quantities of barium salt. What has been demonstrated on a four-rod Paul trap, is a factor of ~ 7 increase in the loading rate of $^{138}Ba^+$ ions when using an autoionizing resonance compared with previous non-resonant schemes. The outlined two-step photoionization scheme is applicable to all isotopes of barium, simply by tuning the first step of the process to be resonant with the desired neutral barium isotope. Autoionizing resonances have not been previously employed to trap Ba^+ ions, and the resonance that was used gives access to the largest experimentally measured photoionization cross-section for barium. There is likely not a more power efficient photoionization scheme that exists for loading Ba^+ ions. Using a more efficient scheme limits the chances of inadvertently charging the trap, allows for increased isotope-selectively by reducing power broadening, and greatly increases the probability of ionization, which is proportional to the probability of loading an ion.

Once this photoionization experiment had been concluded, attention was turned to the atomic source development of barium salt ablation targets. In this situation the challenge is working with microgram quantities of the salt, which is not visible to the naked eye. What was found is that by melting the salt onto the surface of a substrate, such as platinum, or into a low melting point metal like aluminum, that the salt remains present on the target for a factor of ~ 3 longer than if simply dried on the surface. These heat-treatment techniques also made the ablation targets a factor of ~ 4 times more uniform, increasing the targets probability of producing neutral barium atoms each pulse. The targets were

investigated in a purpose-built high-vacuum test chamber and the photons produced by the neutral barium atoms were collected on a PMT for evaluation. Finally, the targets were further characterized before and after ablation using SEM and EDS techniques to image the salt on the surface of the substrates in order to better estimate their lifetime. This experiment deals with a quite specific problem, as is often the case when pursing graduate education, but it opens the doors for other interested groups that want to work with the $^{133}Ba^{+}$ isotope by providing a proven and detailed recipe for creating these microgram quantity ablation targets.

Furthermore, the design and construction of an ultra-high vacuum chamber for a sophisticated chip trap has been presented, which is capable of supporting these long chains of Ba^{+} ions. The necessary optical infrastructure for initially trapping and cooling these ions has been designed and detailed as well. A high numerical aperture titanium room-temperature ultra-high vacuum was constructed and pressure tested for trapping, imaging, and addressing chains of Ba^{+} ions in a surface trap. The construction of this device, as well as supporting optical systems for laser-cooling chains of ions, supports thorough future investigations into active areas of trapped ion research such as cooling long chains to their motional ground state, shuttling and reordering ions, optical individual addressing, and native gate operations, as well as many more.

Finally, the application of double-sideband modulation schemes for amplitude-modulated entangling gates has been numerically simulated and initial results indicate their viability for driving high-fidelity entangling gates in arbitrary pairs of trapped ions within in a long chain. This thesis contains numerical simulations of high-fidelity entangling gates in pairs of trapped ions, using a slightly different approach compared with the traditional segmented-pulse shaped modulation. In this case, optimized parameters are found by tracking the spin-motion entanglement trajectory in phase-space. Then the necessary geometric phase between the two coupled spins is calculated in order to drive $|eee\rangle \rightarrow |gge\rangle$ spin flips. These parameters were then numerically verified using density matrix formalism by solving the von Neumann for the Mølmer–Sørensen Hamiltonian to find Bell state fidelities for the base case of a three ion chain, but the technique itself is likely applicable to longer chains.

References

[1] Peter W. Shor. Polynomial-time algorithms for prime factorization and discrete logarithms on a quantum computer. *SIAM Journal on Computing*, 26(5):1484–1509, October 1997.

[2] Lov K. Grover. A fast quantum mechanical algorithm for database search, 1996.

[3] C. Monroe, D. M. Meekhof, B. E. King, S. R. Jefferts, W. M. Itano, D. J. Wineland, and P. Gould. Resolved-sideband raman cooling of a bound atom to the 3d zero-point energy. *Phys. Rev. Lett.*, 75:4011–4014, Nov 1995.

[4] J. I. Cirac and P. Zoller. Quantum computations with cold trapped ions. *Phys. Rev. Lett.*, 74:4091–4094, May 1995.

[5] Thomas Monz, Daniel Nigg, Esteban A. Martinez, Matthias F. Brandl, Philipp Schindler, Richard Rines, Shannon X. Wang, Isaac L. Chuang, and Rainer Blatt. Realization of a scalable shor algorithm. *Science*, 351(6277):1068–1070, March 2016.

[6] C. Figgatt, D. Maslov, K. A. Landsman, and et al. Complete 3-qubit grover search on a programmable quantum computer. *Nature Communications*, 8:1918, 2017.

[7] S. J. Evered, D. Bluvstein, M. Kalinowski, and et al. High-fidelity parallel entangling gates on a neutral-atom quantum computer. *Nature*, 622:268–272, 2023.

[8] He-Liang Huang, Dachao Wu, Daojin Fan, and Xiaobo Zhu. Superconducting quantum computing: a review. *Science China Information Sciences*, 63(8), July 2020.

[9] Colin D. Bruzewicz, John Chiaverini, Robert McConnell, and Jeremy M. Sage. Trapped-ion quantum computing: Progress and challenges. *Applied Physics Reviews*, 6(2):021314, 05 2019.

[10] H HAFFNER, C ROOS, and R BLATT. Quantum computing with trapped ions. *Physics Reports*, 469(4):155–203, December 2008.

[11] Michael A. Nielsen and Isaac L. Chuang. *Quantum Computation and Quantum Information*. Cambridge University Press, 10th anniversary edition edition, 2010.

[12] R. Blatt and C. Roos. Quantum simulations with trapped ions. *Nature Physics*, 8:277–284, 2012.

[13] T. Monz, K. Kim, A. S. Villar, P. Schindler, M. Chwalla, M. Riebe, C. F. Roos, H. Häffner, W. Hänsel, M. Hennrich, and R. Blatt. Realization of universal ion-trap quantum computation with decoherence-free qubits. *Phys. Rev. Lett.*, 103:200503, Nov 2009.

[14] Klaus Mølmer and Anders Sørensen. Multiparticle entanglement of hot trapped ions. *Phys. Rev. Lett.*, 82:1835–1838, Mar 1999.

[15] P. C. Haljan, K.-A. Brickman, L. Deslauriers, P. J. Lee, and C. Monroe. Spin-dependent forces on trapped ions for phase-stable quantum gates and entangled states of spin and motion. *Phys. Rev. Lett.*, 94:153602, Apr 2005.

[16] Peter Maunz, David Moehring, Steven Olmschenk, Kenneth C. Younge, Dzmitry N. Matsukevich, Luming M. Duan, and Christopher Monroe. Quantum interference of photon pairs from two remote trapped atomic ions. *Nature Physics*, 3:538–541, 2007.

[17] M. L. Day, P. J. Low, B. White, et al. Limits on atomic qubit control from laser noise. *npj Quantum Information*, 8:72, 2022.

[18] J. Thom, B. Yuen, G. Wilpers, et al. Intensity stabilisation of optical pulse sequences for coherent control of laser-driven qubits. *Applied Physics B*, 124:90, 2018.

[19] T. Ruster, C. T. Schmiegelow, H. Kaufmann, et al. A long-lived zeeman trapped-ion qubit. *Applied Physics B*, 122:254, 2016.

[20] Robert McConnell, Colin Bruzewicz, John Chiaverini, and Jeremy Sage. Reduction of trapped-ion anomalous heating by in situ surface plasma cleaning. *Phys. Rev. A*, 92:020302, Aug 2015.

[21] G Pagano, P W Hess, H B Kaplan, W L Tan, P Richerme, P Becker, A Kyprianidis, J Zhang, E Birckelbaw, M R Hernandez, Y Wu, and C Monroe. Cryogenic trapped-ion system for large scale quantum simulation. *Quantum Science and Technology*, 4(1):014004, oct 2018.

[22] L. Egan, D. M. Debroy, C. Noel, et al. Fault-tolerant control of an error-corrected qubit. *Nature*, 598:281–286, 2021.

[23] D. Bluvstein, S. J. Evered, A. A. Geim, and et al. Logical quantum processor based on reconfigurable atom arrays. *Nature*, 626:58–65, 2024.

[24] John Preskill. Fault-tolerant quantum computation, 1997.

[25] E. Knill. Quantum computing with realistically noisy devices. *Nature*, 434:39–44, 2005.

[26] S. A. Moses, C. H. Baldwin, M. S. Allman, R. Ancona, L. Ascarrunz, C. Barnes, J. Bartolotta, B. Bjork, P. Blanchard, M. Bohn, J. G. Bohnet, N. C. Brown, N. Q. Burdick, W. C. Burton, S. L. Campbell, J. P. Campora, C. Carron, J. Chambers, J. W. Chan, Y. H. Chen, A. Chernoguzov, E. Chertkov, J. Colina, J. P. Curtis, R. Daniel, M. DeCross, D. Deen, C. Delaney, J. M. Dreiling, C. T. Ertsgaard, J. Esposito, B. Estey, M. Fabrikant, C. Figgatt, C. Foltz, M. Foss-Feig, D. Francois, J. P. Gaebler, T. M. Gatterman, C. N. Gilbreth, J. Giles, E. Glynn, A. Hall, A. M. Hankin, A. Hansen, D. Hayes, B. Higashi, I. M. Hoffman, B. Horning, J. J. Hout, R. Jacobs, J. Johansen, L. Jones, J. Karcz, T. Klein, P. Lauria, P. Lee, D. Liefer, S. T. Lu, D. Lucchetti, C. Lytle, A. Malm, M. Matheny, B. Mathewson, K. Mayer, D. B. Miller, M. Mills, B. Neyenhuis, L. Nugent, S. Olson, J. Parks, G. N. Price, Z. Price, M. Pugh, A. Ransford, A. P. Reed, C. Roman, M. Rowe, C. Ryan-Anderson, S. Sanders, J. Sedlacek, P. Shevchuk, P. Siegfried, T. Skripka, B. Spaun, R. T. Sprenkle, R. P. Stutz, M. Swallows, R. I. Tobey, A. Tran, T. Tran, E. Vogt, C. Volin, J. Walker, A. M. Zolot, and J. M. Pino. A race-track trapped-ion quantum processor. *Phys. Rev. X*, 13:041052, Dec 2023.

[27] Jwo-Sy Chen, Erik Nielsen, Matthew Ebert, Volkan Inlek, Kenneth Wright, Vandiver Chaplin, Andrii Maksymov, Eduardo Páez, Amrit Poudel, Peter Maunz, and John Gamble. Benchmarking a trapped-ion quantum computer with 29 algorithmic qubits, 2023.

[28] J. M. Pino, J. M. Dreiling, C. Figgatt, and et al. Demonstration of the trapped-ion quantum ccd computer architecture. *Nature*, 592:209–213, 2021.

[29] M. Malinowski, D.T.C. Allcock, and C.J. Ballance. How to wire a 1000-qubit trapped-ion quantum computer. *PRX Quantum*, 4:040313, Oct 2023.

[30] M. Akhtar, F. Bonus, F. R. Lebrun-Gallagher, et al. A high-fidelity quantum matter-link between ion-trap microchip modules. *Nature Communications*, 14:531, 2023.

[31] D. Kielpinski, C. Monroe, and D. Wineland. Architecture for a large-scale ion-trap quantum computer. *Nature*, 417:709–711, 2002.

[32] K. Brown, J. Kim, and C. Monroe. Co-designing a scalable quantum computer with trapped atomic ions. *npj Quantum Inf*, 2:16034, 2016.

[33] C. Monroe, R. Raussendorf, A. Ruthven, K. R. Brown, P. Maunz, L.-M. Duan, and J. Kim. Large-scale modular quantum-computer architecture with atomic memory and photonic interconnects. *Phys. Rev. A*, 89:022317, Feb 2014.

[34] B. Blinov, D. Moehring, L. Duan, et al. Observation of entanglement between a single trapped atom and a single photon. *Nature*, 428:153–157, 2004.

[35] R. Srinivas, C. M. Löschnauer, M. Malinowski, A. C. Hughes, R. Nourshargh, V. Negnevitsky, D. T. C. Allcock, S. A. King, C. Matthiesen, T. P. Harty, and C. J. Ballance. Coherent control of trapped-ion qubits with localized electric fields. *Phys. Rev. Lett.*, 131:020601, Jul 2023.

[36] Joseph Aidan Delf Randall. *High-Fidelity Entanglement of Trapped Ions using Long-Wavelength Radiation*. PhD thesis, February 2016. Submitted for the degree of Doctor of Philosophy.

[37] I. Pogorelov, T. Feldker, Ch. D. Marciniak, L. Postler, G. Jacob, O. Krieglsteiner, V. Podlesnic, M. Meth, V. Negnevitsky, M. Stadler, B. Höfer, C. Wächter, K. Lakhmanskiy, R. Blatt, P. Schindler, and T. Monz. Compact ion-trap quantum computing demonstrator. *PRX Quantum*, 2:020343, Jun 2021.

[38] Laird Egan. *Scaling Quantum Computers with Long Chains of Trapped Ions*. PhD thesis, University of Maryland, Department of Physics, 2021.

[39] M. Akhtar, F. Bonus, F.R. Lebrun-Gallagher, et al. A high-fidelity quantum matter-link between ion-trap microchip modules. *Nat Commun*, 14:531, 2023.

[40] M A Weber, C Löschnauer, J Wolf, M F Gely, R K Hanley, J F Goodwin, C J Ballance, T P Harty, and D M Lucas. Cryogenic ion trap system for high-fidelity near-field microwave-driven quantum logic. *Quantum Science and Technology*, 9(1):015007, oct 2023.

[41] Tyler Ogoshi. Ionq achieves industry leading performance on next generation barium qubits. https://ionq.com/news/ionq-achieves-industry-leading-performance-on-next-generation-barium-qubits, October 2023.

[42] Clayton Crocker. *High Purity Single Photons Entangled with Barium Ions for Quantum Networking*. Doctoral dissertation, University of Maryland, College Park, 2018.

[43] Brendan M. White, Pei Jiang Low, Yvette de Sereville, Matthew L. Day, Noah Greenberg, Richard Rademacher, and Crystal Senko. Isotope-selective laser ablation ion-trap loading of $^{137}Ba^{+}$ using a $bacl_2$ target. *Phys. Rev. A*, 105:033102, 3 2022.

[44] Noah Greenberg, Brendan M White, Pei Jiang Low, and Crystal Senko. Trapping ba+ with seven-fold enhanced efficiency utilizing an autoionizing resonance. *Quantum Science and Technology*, 9(3):035023, may 2024.

[45] Noah Greenberg, Akbar Jahangiri Jozani, Collin J. C. Epstein, Xinghe Tan, Rajibul Islam, and Crystal Senko. Microgram $BaCl_2$ ablation targets for trapped ion experiments, 2024.

[46] Melissa C. Revelle. Phoenix and peregrine ion traps, 2020.

[47] D. T. C. Allcock, W. C. Campbell, J. Chiaverini, I. L. Chuang, E. R. Hudson, I. D. Moore, A. Ransford, C. Roman, J. M. Sage, and D. J. Wineland. omg blueprint for trapped ion quantum computing with metastable states. *Applied Physics Letters*, 119(21), 11 2021. 214002.

[48] Noah Greenberg, Akbar Jahangiri Jozani, Collin J. C. Epstein, Xinghe Tan, Rajibul Islam, and Crystal Senko. Microgram BaCl2 ablation targets for trapped ion experiments. *Review of Scientific Instruments*, 95(4):045117, 04 2024.

[49] Nikhil Kotibhaskar, Noah Greenberg, Sainath Motlakunta, Chung-You Shih, and Rajibul Islam. Fast and high-yield fabrication of axially symmetric ion-trap needle electrodes via two step electrochemical etching. *Review of Scientific Instruments*, 94(3):033201, 03 2023.

[50] Ali Binai-Motlagh, Matthew L Day, Nikolay Videnov, Noah Greenberg, Crystal Senko, and Rajibul Islam. A guided light system for agile individual addressing of ba+ qubits with 10^{-4} level intensity crosstalk. *Quantum Science and Technology*, 8(4):045012, jul 2023.

[51] Virginia Frey, Richard Rademacher, Elijah Durso-Sabina, Noah Greenberg, Nikolay Videnov, Matthew L. Day, Rajibul Islam, and Crystal Senko. A quantum computing programming language for transparent experiment descriptions. In *2021 IEEE International Conference on Quantum Computing and Engineering (QCE)*, pages 244–254, 2021.

[52] I. I. Rabi, J. R. Zacharias, S. Millman, and P. Kusch. A new method of measuring nuclear magnetic moment. *Phys. Rev.*, 53:318–318, Feb 1938.

[53] Norman F. Ramsey. A molecular beam resonance method with separated oscillating fields. *Phys. Rev.*, 78:695–699, Jun 1950.

[54] W Paul and M Raether. Das elektrische massenfilter. *Zeitschrift für Physik*, 140:262–273, 1955.

[55] Robert Weinstock. On a fallacious proof of Earnshaw's theorem. *American Journal of Physics*, 44(4):392–393, 04 1976.

[56] D. Leibfried, R. Blatt, C. Monroe, and D. Wineland. Quantum dynamics of single trapped ions. *Rev. Mod. Phys.*, 75:281–324, Mar 2003.

[57] Wolfgang Paul. Electromagnetic traps for charged and neutral particles. *Rev. Mod. Phys.*, 62:531–540, Jul 1990.

[58] Pei Jiang Low, Brendan M. White, Andrew A. Cox, Matthew L. Day, and Crystal Senko. Practical trapped-ion protocols for universal qudit-based quantum computing. *Phys. Rev. Res.*, 2:033128, Jul 2020.

[59] Patrick See, Guido Wilpers, Patrick Gill, and Alastair G. Sinclair. Fabrication of a monolithic array of three dimensional si-based ion traps. *Journal of Microelectromechanical Systems*, 22(5):1180–1189, 2013.

[60] Zbigniew Dominik Romaszko, Seokjun Hong, Marcin Siegele, Christian Schmiegelow, Lars Bojer Madsen, Peter Krüger, Thomas K Nielsen, Klaus Mølmer, and Anders S Sørensen. Engineering of microfabricated ion traps and integration of advanced on-chip features. *Nature Reviews Physics*, 2:285–299, 2020.

[61] J. D. Sterk, M. G. Blain, M. Delaney, R. Haltli, E. Heller, A. L. Holterhoff, T. Jennings, N. Jimenez, A. Kozhanov, Z. Meinelt, E. Ou, J. Van Der Wall, C. Noel, and D. Stick. Multi-junction surface ion trap for quantum computing, 2024.

[62] S Auchter, C Axline, C Decaroli, M Valentini, L Purwin, R Oswald, R Matt, E Aschauer, Y Colombe, P Holz, T Monz, R Blatt, P Schindler, C Rössler, and J Home. Industrially microfabricated ion trap with 1 ev trap depth. *Quantum Science and Technology*, 7(3):035015, may 2022.

[63] Carmelo Mordini, Alfredo Ricci Vasquez, Yuto Motohashi, Mose Müller, Maciej Malinowski, Chi Zhang, Karan K. Mehta, Daniel Kienzler, and Jonathan P. Home. Multi-zone trapped-ion qubit control in an integrated photonics qccd device, 2024.

[64] M. R. Dietrich, N. Kurz, T. Noel, G. Shu, and B. B. Blinov. Hyperfine and optical barium ion qubits. *Phys. Rev. A*, 81:052328, May 2010.

[65] A. A. Madej and J. D. Sankey. Quantum jumps and the single trapped barium ion: Determination of collisional quenching rates for the $5d^2D_{5/2}$ level. *Phys. Rev. A*, 41:2621–2630, 3 1990.

[66] Natalie C. Brown and Kenneth R. Brown. Comparing zeeman qubits to hyperfine qubits in the context of the surface code: $^{174}Yb^+$ and $^{171}Yb^+$. *Phys. Rev. A*, 97:052301, May 2018.

[67] H. Shao, H. Yue, Z. Ma, Y. Huang, H. Guan, and K. Gao. Precision determination of the $5d^2d_{3/2}$ state lifetime of single $^{174}Yb^+$ ion. *Phys. Rev. Res.*, 5:023193, Jun 2023.

[68] R. Blatt, H. Häffner, C.F. Roos, et al. Ion trap quantum computing with ca^+ ions. *Quantum Information Processing*, 3:61–73, 2004.

[69] David Hucul, Justin E. Christensen, Eric R. Hudson, and Wesley C. Campbell. Spectroscopy of a synthetic trapped ion qubit. *Phys. Rev. Lett.*, 119:100501, Sep 2017.

[70] Justin E. Christensen, David Hucul, Wesley C. Campbell, and Eric R. Hudson. High-fidelity manipulation of a qubit enabled by a manufactured nucleus. *npj Quantum Information*, 6(1):35, Apr 2020.

[71] Noah Greenberg. Vacuum and optical designs for an open-access trapped ion quantum processor. Master's thesis, 2020. http://hdl.handle.net/10012/16334.

[72] Ali Binai-Motlagh, Matthew Day, Nikolay Videnov, Noah Greenberg, Crystal Senko, and Rajibul Islam. A guided light system for agile individual addressing of ba^+ qubits with 10^{-4} level intensity crosstalk, 2023.

[73] Ksenia Sosnova. *Mixed-Species Ion Chains for Quantum Networks*. PhD thesis, University of Maryland, College Park, 2020.

[74] D. Rotter. *Quantum feedback and quantum correlation measurements with a single Barium ion*. PhD thesis, University of Innsbruck, Innsbruck, Austria, 2008.

[75] R. D. Graham, S.-P. Chen, T. Sakrejda, J. Wright, Z. Zhou, and B. B. Blinov. A system for trapping barium ions in a microfabricated surface trap. *AIP Advances*, 4(5):057124, 05 2014.

[76] J. Zhang, G. Pagano, P. Hess, and et al. Observation of a many-body dynamical phase transition with a 53-qubit quantum simulator. *Nature*, 551:601–604, 2017.

[77] Grahame Vittorini. *Stability of Ion Chains in a Cryogenic Surface-Electrode Ion Trap*. PhD thesis, Georgia Institute of Technology, December 2013.

[78] B. Wang, J. W. Zhang, C. Gao, and L. J. Wang. Highly efficient and isotope selective photo-ionization of barium atoms using diode laser and led light. *Opt. Express*, 19(17):16438, 2011.

[79] G Leschhorn, T Hasegawa, and T Schaetz. Efficient photo-ionization for barium ion trapping using a dipole-allowed resonant two-photon transition. *Applied Physics B*, 108(1):159–165, July 2012.

[80] S. Olmschenk and P. Becker. Laser ablation production of Ba, Ca, Dy, Er, La, Lu, and Yb ions. *Appl. Phys. B Lasers Opt.*, 123(4):1–6, 2017.

[81] X. Shi, S. L Todaro, G. L. Mintzer, C. D. Bruzewicz, J. Chiaverini, and I. L. Chuang. Ablation loading of barium ions into a surface-electrode trap. *Applied Physics Letters*, 122(26):264002, 06 2023.

[82] Nikhil Kotibhaskar. Design and construction of an ion trapping apparatus for quantum simulation experiments. UWSpace, 2019.

[83] R J Hendricks, D M Grant, P F Herskind, A Dantan, and M Drewsen. An all-optical ion-loading technique for scalable microtrap architectures. *Applied Physics B*, 88(4):507–513, September 2007.

[84] S. De, U. Dammalapati, K. Jungmann, and L. Willmann. Magneto-optical trapping of barium. *Phys. Rev. A*, 79:041402, Apr 2009.

[85] Marko Cetina, Andrew Grier, Jonathan Campbell, Isaac Chuang, and Vladan Vuletić. Bright source of cold ions for surface-electrode traps. *Phys. Rev. A*, 76:041401, Oct 2007.

[86] K. Vant, J. Chiaverini, W. Lybarger, and D. J. Berkeland. Photoionization of strontium for trapped-ion quantum information processing, 2006.

[87] Sainath Motlakunta. Developing a large-scale, programmable trapped ion quantum simulator with in situ mid-circuit measurement and reset. http://hdl.handle.net/10012/19938, 2023.

[88] Michael N.R. Ashfold and Colin M. Western. Multiphoton spectroscopy, applications. In John C. Lindon, editor, *Encyclopedia of Spectroscopy and Spectrometry*, pages 1424–1433. Elsevier, Oxford, 1999.

[89] S. Niggli and M. C. Huber. Transition probabilities in neutral barium. *Phys. Rev. A*, 35(7):2908–2918, 1987.

[90] S. Niggli and M. C. E. Huber. Transition probabilities for infrared and visible lines in neutral barium. *Phys. Rev. A*, 39:3924–3931, Apr 1989.

[91] J. Z. Klose, J. R. Fuhr, and W. L. Wiese. Critically Evaluated Atomic Transition Probabilities for Ba I and Ba II. *Journal of Physical and Chemical Reference Data*, 31(1):217–230, 04 2002.

[92] Hans Karlsson and Ulf Litzén. Revised ba i and ba ii wavelengths and energy levels derived by fourier transform spectroscopy. *Physica Scripta*, 60(4):321, oct 1999.

[93] A.M. Akulshin, A.A. Celikov, and V.L. Velichansky. Nonlinear doppler-free spectroscopy of the 61s0-63p1 intercombination transition in barium. *Optics Communications*, 93(1):54–58, 1992.

[94] V. A. Dzuba, V. V. Flambaum, and J. S. M. Ginges. Calculation of parity and time invariance violation in the radium atom. *Phys. Rev. A*, 61:062509, May 2000.

[95] B Willke and M Kock. Measurement of photoionization cross sections from the laser-excited ba i (6s6p) 1p10 state. *Journal of Physics B: Atomic, Molecular and Optical Physics*, 26(6):1129, 3 1993.

[96] L.-W. He, C. E. Burkhardt, M. Ciocca, J. J. Leventhal, and S. T. Manson. Absolute cross sections for the photoionization of the 6s6p ^{1}p excited state of barium. *Phys. Rev. Lett.*, 67:2131–2134, 10 1991.

[97] M. M. Ali Kalyar. *Two-step Laser Excitation Studies of Bound and Autoionizing States in Barium*. PhD thesis, Quaid-i-Azam University, Islamabad, 2008.

[98] U. Fano. Effects of configuration interaction on intensities and phase shifts. *Phys. Rev.*, 124:1866–1878, 12 1961.

[99] A. G. Shenstone. Ultra-ionization potentials in mercury vapor. *Phys. Rev.*, 38:873–875, 9 1931.

[100] U Fano. Correlations of two excited electrons. *Reports on Progress in Physics*, 46(2):97, 2 1983.

[101] M Aymar. Eigenchannel r-matrix calculation of the j=1 odd-parity spectrum of barium. *Journal of Physics B: Atomic, Molecular and Optical Physics*, 23(16):2697, 8 1990.

[102] M Aymar and O Robaux. Multichannel quantum-defect analysis of the bound even-parity j=2 spectrum of neutral barium. *Journal of Physics B: Atomic and Molecular Physics*, 12(4):531, 2 1979.

[103] Mireille Aymar, Chris H. Greene, and Eliane Luc-Koenig. Multichannel rydberg spectroscopy of complex atoms. *Rev. Mod. Phys.*, 68:1015–1123, 10 1996.

[104] Chris H. Greene and Constantine E. Theodosiou. Photoionization of the ba 6s6p $^1p_1$ state. *Phys. Rev. A*, 42:5773–5775, 11 1990.

[105] Chris H. Greene and Mireille Aymar. Spin-orbit effects in the heavy alkaline-earth atoms. *Phys. Rev. A*, 44:1773–1790, 8 1991.

[106] P. J. A. Buttle. Solution of coupled equations by r-matrix techniques. *Phys. Rev.*, 160:719–729, Aug 1967.

[107] P Camus, M Dieulin, A El Himdy, and M Aymar. Two-step optogalvanic spectroscopy of neutral barium: Observation and interpretation of the even levels above the 6s ionization limit between 5.2 and 7 ev. *Physica Scripta*, 27(2):125, 2 1983.

[108] L. Deslauriers, M. Acton, B. B. Blinov, K.-A. Brickman, P. C. Haljan, W. K. Hensinger, D. Hucul, S. Katnik, R. N. Kohn, P. J. Lee, M. J. Madsen, P. Maunz, S. Olmschenk, D. L. Moehring, D. Stick, J. Sterk, M. Yeo, K. C. Younge, and C. Monroe. Efficient photoionization loading of trapped ions with ultrafast pulses. *Phys. Rev. A*, 74:063421, 12 2006.

[109] X. Shi, S. L. Todaro, G. L. Mintzer, C. D. Bruzewicz, J. Chiaverini, and I. L. Chuang. Ablation loading of barium ions into a surface electrode trap, 2023.

[110] Putterman S. Kirilov E. Two-photon ionization for efficient seeding and trapping of strontium ions. *The European Physical Journal D*, 54(2):683–691, 2009.

[111] Alto Osada and Atsushi Noguchi. Deterministic loading of a single strontium ion into a surface electrode trap using pulsed laser ablation. *Journal of Physics Communications*, 6(1):015007, jan 2022.

[112] Peter Maunz, Jonathan Mizrahi, and Josh Goldberg. Ioncontrol v. 1.0, version 00, 6 2016.

[113] P. J. Low. Tolerable experimental imperfections for a quadrupole blade ion trap and practical qudit gates with trapped ions. Master's thesis, University of Waterloo, 2019.

[114] D. M. Lucas, A. Ramos, J. P. Home, M. J. McDonnell, S. Nakayama, J.-P. Stacey, S. C. Webster, D. N. Stacey, and A. M. Steane. Isotope-selective photoionization for calcium ion trapping. *Phys. Rev. A*, 69:012711, Jan 2004.

[115] B. Bramman. *Ablation loading and qudit measurements with barium ions*. PhD thesis, University of Waterloo, Waterloo, 2023.

[116] P.J. Low. *Control and Readout of High-Dimensional Trapped Ion Qudits*. PhD thesis, University of Waterloo, Waterloo, 2023.

[117] M. G. Payne and G. S. Hurst. *Theory of Resonance Ionization Spectroscopy*, pages 183–188. Springer US, Boston, MA, 1985.

[118] Darrell J. Armstrong, Robert P. Wood, and Chris H. Greene. Photoionization of the 5d6p $^3d_1$ state of barium. *Phys. Rev. A*, 47:1981–1988, Mar 1993.

[119] S. Gao, W. J. Hughes, D. M. Lucas, T. G. Ballance, and J. F. Goodwin. An optically heated atomic source for compact ion trap vacuum systems. *Rev Sci Instrum*, 92(3):033205, Mar 2021.

[120] J. E. Christensen. *High-fidelity operation of a radioactive trapped ion qubit,* ^{133}Ba. PhD thesis, University of California, Los Angeles, 2020.

[121] Z.S. Smith et al. The 133ba+ ion platform. In *51st Annual Meeting of the APS Division of Atomic, Molecular and Optical Physics*, volume 65, Portland, Oregon, June 2020. APS, American Physical Society.

[122] Andres Vazquez Brennan et al. Towards building and controlling large registers of 133ba+ trapped-ion qubits. In *53rd Annual Meeting of the APS Division of Atomic, Molecular and Optical Physics*, volume 67, Orlando, Florida, June 2022. APS, American Physical Society.

[123] Nuclear substances and radiation devices regulations, Oct 2015.

[124] Marcel Rey, Johannes Walter, Johannes Harrer, Carmen Morcillo Perez, Salvatore Chiera, Sharanya Nair, Maret Ickler, Alesa Fuchs, Mark Michaud, Maximilian J Uttinger, Andrew B Schofield, Job H J Thijssen, Monica Distaso, Wolfgang Peukert, and Nicolas Vogel. Versatile strategy for homogeneous drying patterns of dispersed particles. *Nature Communications*, 13(1):2840, May 2022.

[125] Shyamashis Das, Atreya Dey, Govardhan Reddy, and D. D. Sarma. Suppression of the coffee-ring effect and evaporation-driven disorder to order transition in colloidal droplets. *The Journal of Physical Chemistry Letters*, 8(19):4704–4709, 2017. PMID: 28885853.

[126] Michael J. Hertaeg, Clare Rees-Zimmerman, Rico F. Tabor, Alexander F. Routh, and Gil Garnier. Predicting coffee ring formation upon drying in droplets of particle suspensions. *Journal of Colloid and Interface Science*, 591:52–57, 2021.

[127] Frank Rösch. *Nuclear- and Radiochemistry*. De Gruyter, 2014.

[128] https://pubchem.ncbi.nlm.nih.gov/compound/Barium-133. Accessed: 2023-11-8.

[129] Joseph I. Goldstein, Dale E. Newbury, Joseph R. Michael, Nicholas W.M. Ritchie, John Henry J. Scott, and David C. Joy. *Scanning Electron Microscopy and X-Ray Microanalysis*. Springer New York, NY, 4th edition, 2017.

[130] Geert Vrijsen, Yuhi Aikyo, Robert F. Spivey, I. Volkan Inlek, and Jungsang Kim. Efficient isotope-selective pulsed laser ablation loading of 174yb+ ions in a surface electrode trap. *Opt. Express*, 27(23):33907–33914, Nov 2019.

[131] J. A. Sedlacek, J. Stuart, D. H. Slichter, C. D. Bruzewicz, R. McConnell, J. M. Sage, and J. Chiaverini. Evidence for multiple mechanisms underlying surface electric-field noise in ion traps. *Phys. Rev. A*, 98:063430, Dec 2018.

[132] Q. A. Turchette, Kielpinski, B. E. King, D. Leibfried, D. M. Meekhof, C. J. Myatt, M. A. Rowe, C. A. Sackett, C. S. Wood, W. M. Itano, C. Monroe, and D. J. Wineland. Heating of trapped ions from the quantum ground state. *Phys. Rev. A*, 61:063418, May 2000.

[133] L. Deslauriers, S. Olmschenk, D. Stick, W. K. Hensinger, J. Sterk, and C. Monroe. Scaling and suppression of anomalous heating in ion traps. *Phys. Rev. Lett.*, 97:103007, Sep 2006.

[134] J. A. Sedlacek, A. Greene, J. Stuart, R. McConnell, C. D. Bruzewicz, J. M. Sage, and J. Chiaverini. Distance scaling of electric-field noise in a surface-electrode ion trap. *Phys. Rev. A*, 97:020302, Feb 2018.

[135] F R Lebrun-Gallagher, N I Johnson, M Akhtar, S Weidt, D Bretaud, S J Hile, A Owens, F Bonus, and W K Hensinger. A scalable helium gas cooling system for trapped-ion applications. *Quantum Science and Technology*, 7(2):024002, mar 2022.

[136] Robert Fulton Spivey. *A Compact Cryogenic Package Approach to Ion Trap Quantum Computing*. PhD thesis, Duke University, 2022.

[137] M. Day. *Microfabricated Optics for Quantum Control of Trapped Ions*. Doctoral thesis, University of Bristol, November 6 2018.

[138] K. K. Mehta, C. Zhang, M. Malinowski, and et al. Integrated optical multi-ion quantum logic. *Nature*, 586:533–537, 2020.

[139] Jungsang Kim and Peter Lukas Wilhelm Maunz. System and method for improved vacuum in compact packages, 2023.

[140] Allison L. Carter, Jameson O'Reilly, George Toh, Sagnik Saha, Mikhail Shalaev, Isabella Goetting, and Christopher Monroe. Ion trap with in-vacuum high numerical aperture imaging for a dual-species modular quantum computer. 2023.

[141] Wermac.org. Density of metals. https://www.wermac.org/materials/density_of_metal.html. [Accessed on 15th March 2024].

[142] H Kurisu, K Ishizawa, S Yamamoto, M Hesaka, and Y Saito. Application of titanium materials to vacuum chambers and components. *Journal of Physics: Conference Series*, 100(9):092002, mar 2008.

[143] C Sittig, M Textor, ND Spencer, M Wieland, and PH Vallotton. Surface characterization of implant materials c.p. ti, ti-6al-7nb and ti-6al-4v with different pretreatments. *Journal of Materials Science: Materials in Medicine*, 10(1):35–46, 1999.

[144] R. Kersevan and J.-L. Pons. Introduction to MOLFLOW+: New graphical processing unit-based Monte Carlo code for simulating molecular flows and for calculating angular coefficients in the compute unified device architecture environment. *Journal of Vacuum Science Technology A*, 27(4):1017–1023, 06 2009.

[145] Ruta Sirvinskaite. Non-evaporable getter coating optimisation for future particle accelerators, 2023.

[146] Pedro Parrado-Rodríguez, Ciarán Ryan-Anderson, Alejandro Bermudez, and Markus Müller. Crosstalk suppression for fault-tolerant quantum error correction with trapped ions. *Quantum*, 5:487, June 2021.

[147] M. Cetina, L.N. Egan, C. Noel, M.L. Goldman, D. Biswas, A.R. Risinger, D. Zhu, and C. Monroe. Control of transverse motion for quantum gates on individually addressed atomic qubits. *PRX Quantum*, 3:010334, Mar 2022.

[148] Pei Jiang Low, Brendan White, and Crystal Senko. Control and readout of a 13-level trapped ion qudit, 2023.

[149] Donald S Smith and Michael G Stabin. Exposure rate constants and lead shielding values for over 1,100 radionuclides. *Health Phys*, 102(3):271–291, Mar 2012.

[150] U.S. Environmental Protection Agency. Radiation Sources and Doses, Accessed 2024. Accessed on: 2024-03-22.

[151] Ali Binai-motlagh. Robust optical engineering for a trapped ion quantum computer. Master's thesis, 2022. http://hdl.handle.net/10012/18710.

[152] Nikolay Videnov. Optical design for an open access trapped ion quantum processor. Master's thesis, 2021. http://hdl.handle.net/10012/17323.

[153] XingHe Tan. Optimization of the optical infrastructure and trapping potential for a quantum processor based on trapped barium ions. Master's thesis, 2024. http://hdl.handle.net/10012/20332.

[154] T. Choi, S. Debnath, T. A. Manning, C. Figgatt, Z.-X. Gong, L.-M. Duan, and C. Monroe. Optimal quantum control of multimode couplings between trapped ion qubits for scalable entanglement. *Phys. Rev. Lett.*, 112:190502, May 2014.

[155] J. I. Cirac and P. Zoller. Quantum computations with cold trapped ions. *Phys. Rev. Lett.*, 74:4091–4094, May 1995.

[156] Timothy Andrew Manning. *Quantum Information Processing with Trapped Ion Chains*. PhD thesis, University of Maryland, Department of Physics, 2014.

[157] P J Lee, K-A Brickman, L Deslauriers, P C Haljan, L-M Duan, and C Monroe. Phase control of trapped ion quantum gates. *Journal of Optics B: Quantum and Semiclassical Optics*, 7(10):S371, sep 2005.

[158] Caroline Margaret Figgatt. *Building and Programming a Universal Ion Trap Quantum Computer*. Doctor of philosophy, Department of Physics, University of Maryland-College Park, College Park, Maryland, 2018.

[159] Colin P. Williams. Quantum gates. In *Explorations in Quantum Computing*, Texts in Computer Science, pages 51–122. Springer, London, 2011.

[160] Reinhold Blümel, Nikodem Grzesiak, Neal Pisenti, Kenneth Wright, and Yunseong Nam. Power-optimal, stabilized entangling gate between trapped-ion qubits. *npj Quantum Information*, 7(1):147, Oct 2021.

[161] Reinhold Blümel, Nikodem Grzesiak, Nhung H. Nguyen, Alaina M. Green, Ming Li, Andrii Maksymov, Norbert M. Linke, and Yunseong Nam. Efficient stabilized two-qubit gates on a trapped-ion quantum computer. *Phys. Rev. Lett.*, 126:220503, Jun 2021.

[162] Pak Hong Leung, Kevin A. Landsman, Caroline Figgatt, Norbert M. Linke, Christopher Monroe, and Kenneth R. Brown. Robust 2-qubit gates in a linear ion crystal using a frequency-modulated driving force. *Phys. Rev. Lett.*, 120:020501, Jan 2018.

[163] Alistair R. Milne, Claire L. Edmunds, Cornelius Hempel, Federico Roy, Sandeep Mavadia, and Michael J. Biercuk. Phase-modulated entangling gates robust to static and time-varying errors. *Phys. Rev. Appl.*, 13:024022, Feb 2020.

[164] John von Neumann. *Mathematical Foundations of Quantum Mechanics*. Princeton University Press, Princeton, NJ, 1932.

[165] Christian F Roos. Ion trap quantum gates with amplitude-modulated laser beams. *New Journal of Physics*, 10(1):013002, jan 2008.

[166] D. J. Wineland, C. Monroe, W. M. Itano, D. Leibfried, B. E. King, and D. M. Meekhof. Experimental issues in coherent quantum-state manipulation of trapped atomic ions. *Journal of Research of the National Institute of Standards and Technology*, 103(3):259, May–June 1998.

[167] S. Blanes, F. Casas, J.A. Oteo, and J. Ros. The magnus expansion and some of its applications. *Physics Reports*, 470(5–6):151–238, January 2009.

[168] B.A. Shanoi. *Introduction to Digital Signal Processing and Filter Design*. Wiley Interscience, 2006.

[169] K. M. M. Prabhu. *Window Functions and Their Applications in Signal Processing*. CRC Press, Taylor Francis Group, 1st edition, October 2013.

[170] M. Brownnutt, M. Kumph, P. Rabl, and R. Blatt. Ion-trap measurements of electric-field noise near surfaces. *Rev. Mod. Phys.*, 87:1419–1482, Dec 2015.

[171] Haim Nakav, Ran Finkelstein, Lee Peleg, Nitzan Akerman, and Roee Ozeri. Effect of fast noise on the fidelity of trapped-ion quantum gates. *Phys. Rev. A*, 107:042622, Apr 2023.

[172] Brennan de Neeve. Calibrating an ion-trap quantum computer. Master's thesis, ETH Zürich, July 2017.

[173] Crystal Noel, Maya Berlin-Udi, Clemens Matthiesen, Jessica Yu, Yi Zhou, Vincenzo Lordi, and Hartmut Häffner. Electric-field noise from thermally activated fluctuators in a surface ion trap. *Phys. Rev. A*, 99:063427, Jun 2019.

[174] Larry Brown and Tom Holme. *Chemistry for Engineering Students*. Brooks Cole, 2nd edition, 2010.

[175] Ioannis Arvanitidis, Du Sichen, and Seshadri Seetharaman. A study of the thermal decomposition of baco3. *Metall. and Mater. Trans. B*, 27B:409–416, 06 1996.

[176] Henry W Rahn and Charles J Sindlinger. Calcination of barium carbonate, 11 1956.

[177] Robert Kresse, Ulrich Baudis, Paul Jäger, H. Riechers, Heinz Wagner, Jochen Winkler, and Hans Wolf. *Barium and Barium Compounds*, volume 36. 07 2007.

[178] Larry Brown and Tom Holme. *Chemistry for Engineering Students*. Brooks Cole, 4th edition, Publication Year.

[179] Gordon Drake. *Springer Handbook of Atomic, Molecular, and Optical Physics*. 01 2006.

[180] International chemical safety card for barium chloride. https://www.inchem.org/documents/icsc/icsc/eics0615.htm. Accessed: 2024-01-13.

[181] C. J. Ballance, T. P. Harty, N. M. Linke, M. A. Sepiol, and D. M. Lucas. High-fidelity quantum logic gates using trapped-ion hyperfine qubits. *Phys. Rev. Lett.*, 117:060504, Aug 2016.

[182] P. Wang, C. Y. Luan, M. Qiao, and et al. Single ion qubit with estimated coherence time exceeding one hour. *Nat Commun*, 12:233, 2021.

[183] Ben Barber, Kenton M. Barnes, Tomasz Bialas, Okan Buğdaycı, Earl T. Campbell, Neil I. Gillespie, Kauser Johar, Ram Rajan, Adam W. Richardson, Luka Skoric, Canberk Topal, Mark L. Turner, and Abbas B. Ziad. A real-time, scalable, fast and highly resource efficient decoder for a quantum computer, 2023.

[184] Elijah Durso-Sabina. Flag fault-tolerant error correction with qudits. Master's thesis, 2022.

[185] Colin D Bruzewicz, Robert McConnell, Jeffrey Stuart, and et al. Dual-species, multi-qubit logic primitives for ca+/sr+ trapped-ion crystals. *npj Quantum Inf*, 5:102, 2019.

[186] Patricia J. Lee. *Quantum Information Processing with Two Trapped Cadmium Ions*. Doctor of philosophy, University of Michigan, Physics, 2006.

[187] Chun Kit Lam, Stephan Maka, David Nadlinger, Chris Ballance, and Sébastien Bourdeauducq. Combining processing throughput, low latency and timing accuracy in experiment control, 2021.

[188] Di Yan, Tao Wu, Ying Liu, and Yang Gao. An efficient sparse-dense matrix multiplication on a multicore system. In *2017 IEEE 17th International Conference on Communication Technology (ICCT)*, pages 1880–1883, 2017.

[189] Kendall E. Atkinson. *An Introduction to Numerical Analysis*. John Wiley & Sons, 2nd edition, 1989.

[190] Uri M. Ascher and Linda R. Petzold. *Computer Methods for Ordinary Differential Equations and Differential-Algebraic Equations*. Society for Industrial and Applied Mathematics, Philadelphia, 1998.

APPENDICES

Appendix A

Atomic Source Testing

A.1 Measuring Ring Thickness & Ablation Spot Size

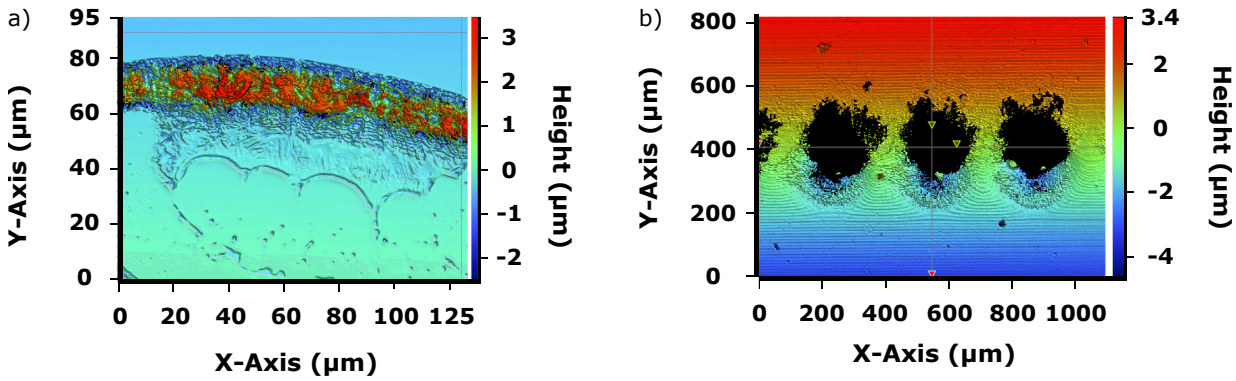


Figure A.1: a) Optical profilometer measurement of a $BaCl_2$ ring on a gold microfabricated substrate. The thickness is at most 3 μm and the ring thickness is $\sim$ 20 μm. b) Ablation of a microfabricated gold chip. The chip was mounted where the tested $BaCl_2$ ablation targets were placed inside the high-vacuum chamber to get an accurate spot size. The spot size was measured to be $\sim$ 300 μm in diameter.

In order to ensure the procedure is depositing known quantities of salt onto the ablation targets described in Section 3, a test solution was made such that $\sim$ 1 μg of material would be deposited per drop (10 μl drop volume). Using a pipette, a single drop was deposited onto a gold microfabricated substrate. An image of a section of the $BaCl_2$ ring is shown in

Fig. A.1a. The smooth surface allows the formation of rings with a uniform radius so that the volume can be estimated and the mass roughly calculated. The image of the ring gave a maximum thickness of $\sim 3\ \mu$m and a maximum ring width of $\sim 20\ \mu$m. The ring diameter is roughly ~ 1.5 mm based on the optical profilometer measurements. The maximum volume of $BaCl_2$ in this drop can then be calculated $v_{\text{salt}} \approx \left(0.1501^2 - 0.15^2\right) \pi\,\text{cm}^2 \times 3 \cdot 10^{-4}\,\text{cm} \approx 2.8368 \times 10^{-7}\text{cm}^3$ and assuming a density 3.86 g/cm^3 for $BaCl_2$ [180], the amount of material can be estimated to be $m_{\text{salt}} \approx 1.1\ \mu$g.

Additionally, Fig. A.1b shows ablation spots on gold microfabricated chips. This was done for the purposes of aligning the ablation telescope initially and estimating the beam waist to be $\sim 150\ \mu$m. This was used to calculate the fluence for the set of experiments discussed in Section 3 ($\sim 0.42 \pm 0.02$ J/cm^2).

A.2 Optical Diagrams for Ablation Testing

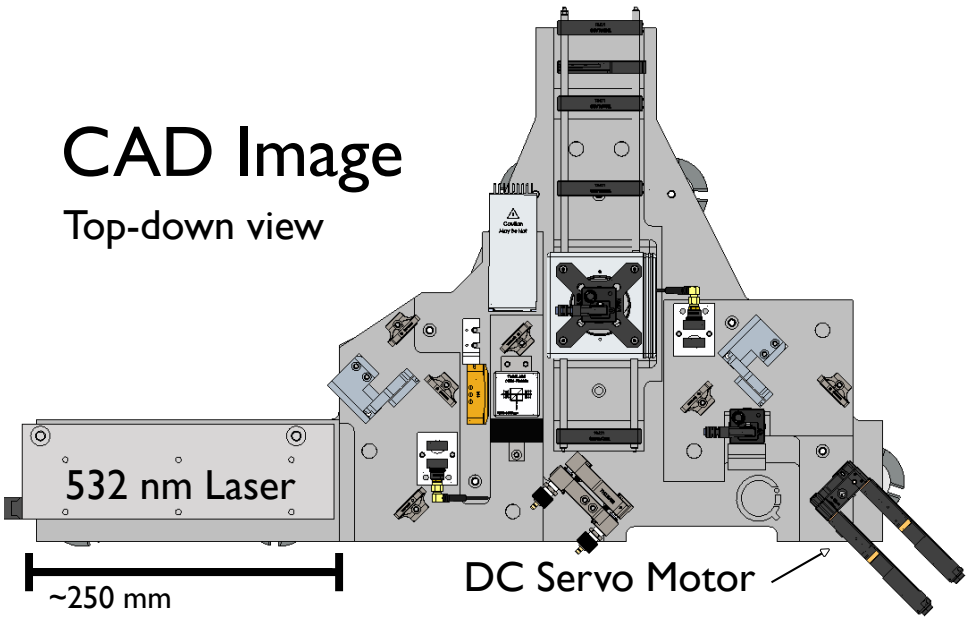


Figure A.2: CAD rendering of the ablation beam path used to test different $BaCl_2$ targets. The 532 nm laser is nanosecond pulsed laser with repetition rates up to 2 kHz and pulse energies up to 1 mJ. The DC servo-motor mirror mount is used to scan the surface of the ablation target. Thanks to engineering student Levi Medeiros for designing the CAD model for the ablation beam path and drawing the parts for machining.

Two figures are presented, Fig. A.2 and Fig. A.3, describing the ablation beampath that was used in Section 3 to test $BaCl_2$ ablation targets. This beampath will also be used for ablating and trapping ions in a chip trap housed inside an ultra-high vacuum chamber described in Section 4.

The CAD model in Fig. A.2 shows a top-down view of the optical beampath for ablating barium targets. There is a large, custom aluminum base breadboard ($\sim$ 2 $''$ thick) on which the ablation laser and optics sit. On this base breadboard, smaller custom aluminum breadboards sit that contain specific modules of the beampath such as the polarization and gross power control section, beam dumping, beam pointing, and beam shaping (telescope) sections. Modularization of these boards allow for independent assembly and testing and makes initial alignment or realignment into a vacuum chamber inherently easier. The ablation beam will scan the surface of the target with a DC servo motorized mirror mount from Thorlabs (PN: KS1-Z8). The DC servo motor mirror mount gives angular adjustments of $\pm 4^{\circ}$, which is in contrast to piezo electric mirror mounts with a much smaller angular throw. With a focal length of $\sim$ 250 mm, over 1 mm^2 of the ablation target surface can be scanned remotely using the servo motor. To scan a separate section of the ablation target, the beam pointing can be adjusted manually using two mirrors, which will allow targets up to $\sim 20 \times 20$ mm^2 to be scanned.

A breadboard was not designed for the 554 nm laser beampath. Instead, common optical components like dielectric mirrors and lenses were assembled from Thorlabs products. The beampath consisted of a collimator, followed by a half-wave plate and polarizing beam splitter before entering a set of four dielectric mirrors, wrapping and ultimately sending the beam through a 125 mm focal length lens directly infront of the vacuum viewport. The 554 nm beam is aligned through a set of two apertures, referenced to the high-vacuum chamber. The beam diameter is estimated to be ~ 44 μm.

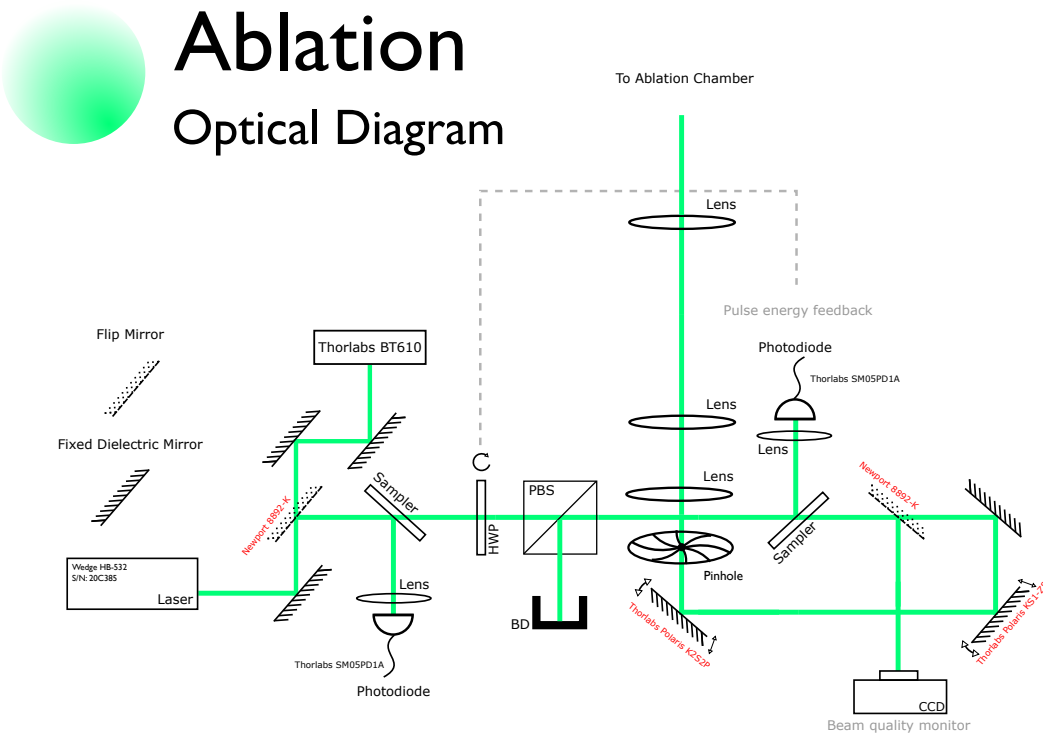


Figure A.3: Optical circuit diagaram of the ablation beampath shown in Fig. A.2. The ablation beam is telescoped through 2 ″ lenses and focused down $\sim$ 250 mm away from the last lens on the ablation target. The laser has a high divergence with a maximum value of $\sim$ 6 mrad.

Many of the components and layout of the optical beampaths discussed in Section 4 are similar to what is presented here in Fig. A.3. All of the breadboards are designed to be entirely remotely controlled, allowing for power and polarization to be adjusted with motorized stages. For example, a half-wave plate in a motorized rotation stage is coupled with a polarizing beam splitter and sampler onto a photodiode for gross power control. A flip mirror can also be activated to monitor the beam profile on a CCD and as already mentioned, the beam pointing can be remotely set. Including these types of devices throughout the optical setup allows for more consistency when running experiments by implementing calibration routines when sensors detect drifts from desired set points.

A.3 Selected SEM Images of Ablation Targets

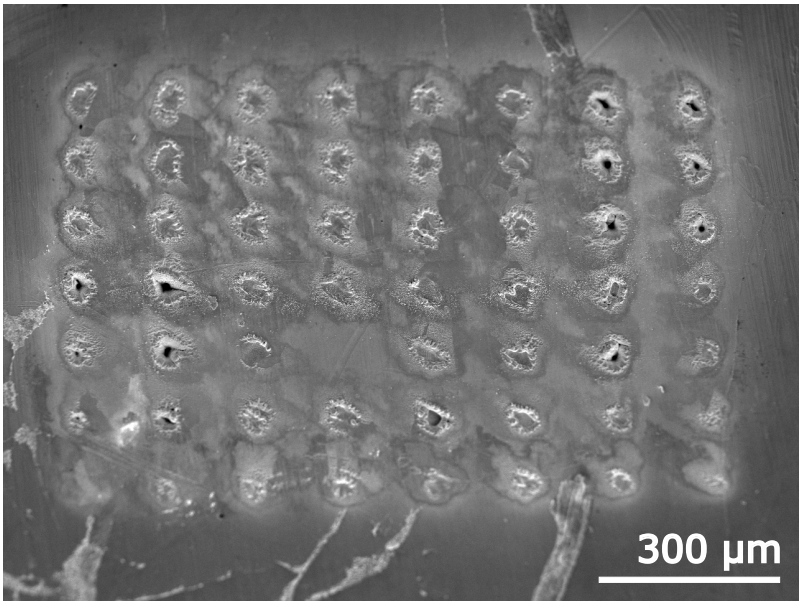


Figure A.4: Image taken of a Pt ablation target with 5 μg of $BaCl_2$ with a JEOL JSM-7200F scanning electron microscope. A total of 7/55 spots met the σ_1 criteria, with an average lifetime of 100 pulses. A total of 4/55 spots met the σ_2 criteria, with an average lifetime of 154 pulses. It is estimated that only 12/55 spots were impingement on a section of the $BaCl_2$ ring.

Another image of a non heat-treated Pt ablation target is shown in Fig. A.4. This image highlights the concentration of the $BaCl_2$ into rings on the surface of the platinum substrate. Attempting to ablate the $BaCl_2$ rings is difficult because they sparsely populate the surface. Assuming a ring has been found, it will last at most a couple hundred of pulses, and then the surface of the ablation target will have to be scanned again in order to reload the ion trap. This could correspond to finding a new ablation spot at least every few days, which would be an unfortunate amount of effort to spend on simply loading ions. Melting the $BaCl_2$ on the surface of the platinum makes ablation targets more uniform.

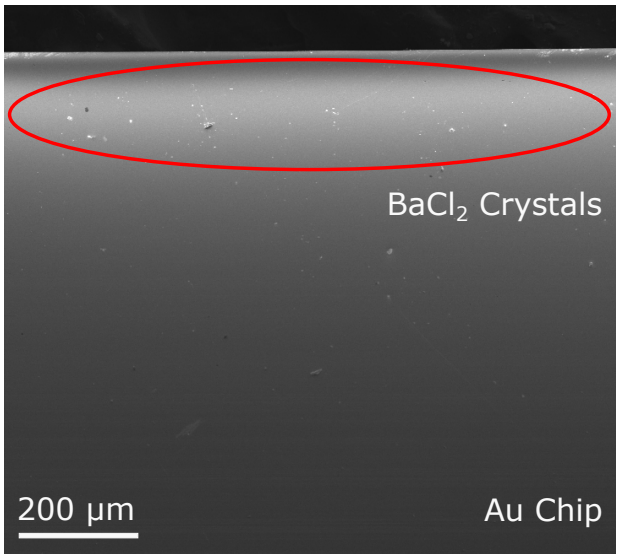


Figure A.5: SEM image of a gold microfabricated chip with $BaCl_2$ crystals on the surface after ablation of a heat-treated macroscopic Pt* ablation target with ~ 0.2 mg of $BaCl_2$. This shows that even with relatively small amounts of $BaCl_2$ used on ablation targets, contamination would likely still immediately be evident on a surface trap.

A.4 Recipe for Producing ^{133}Ba Metal

Ablation of metals is favorable when compared with salts. Ablation of a salt can produce an atomic plume, on average, several orders of magnitude faster than a metal. This has been shown directly with barium metal and barium salt ablation targets [81]. Unfortunately ^{133}Ba metal is not readily available, but there are plausible recipes for producing metallic barium from barium salts, one of which is outlined below. This was not attempted in this manuscript, as this process would work best with significantly more ^{133}Ba than what we can easily obtain or work with in an academic setting.

1. The first step, assuming one has acquired ^{133}Ba in the form of $BaCl_2$, is to perform a precipitation reaction. This can be done by by mixing $BaCl_2$ into an aqueous solution of Na_2CO_3 [174].

$$Na_2CO_3(aq) + BaCl_2(aq) \rightarrow BaCO_3(s) + 2NaCl(aq) \tag{A.1}$$

   The barium carbonate ($BaCO_3$) will form in the solution, which can then be strained out and used in the next step to produce barium oxide.

2. The second step is to perform a decomposition of the barium carbonate [175], or more specifically calcination, which can occur when barium carbonate is heated to 1360° C [176].

$$\mathrm{BaCO_3(s) \rightarrow BaO(s) + CO_2(g)} \tag{A.2}$$

   This will produce barium oxide and carbon dioxide gas.

3. The final step is a reduction in which the barium oxide is heated to at least 1100° with aluminum in an inert gas such as argon [177]. Note that $\mathrm{BaAl_4(s)}$ metal forms as a reaction intermediate. The overall reaction is written below [178].

$$\mathrm{4BaO(s) + 2Al(s) \rightarrow 3Ba + BaAl_2O_4} \tag{A.3}$$

   In principle, this last step could be done with a tube furnace or chamber equipped with argon.

$$\mathrm{3BaO(s) + 14Al(s) \rightarrow 3BaAl_4(s) + Al_2O_3(s)} \tag{A.4}$$

$$\mathrm{8BaO(s) + BaAl_4(s) \rightarrow Ba + 7BaAl_2O_4} \tag{A.5}$$

$$\mathrm{BaO(s) + Al_2O_3(s) \rightarrow BaAl_2O_4} \tag{A.6}$$

The above steps detail a recipe for producing metallic barium from $\mathrm{BaCl_2}$. The recipe could be greatly simplified if one was able to obtain ^{133}Ba in the form of barium carbonate, or better still, barium oxide. In a production setting, in order to prevent oxidation of the metallic barium after creation, it would be best to package the source with the trap in the same machine.

Appendix B

Infrastructure

B.1 Electrical Infrastructure

The are multiple popular hardware systems that can be used to run trapped ion quantum experiments, which require precise timings, typically controlled by field-programmable gate arrays (FPGA). Readily available solutions exist such as IonControl [112], Riverlane [183], Quantum Machines, Keysight, and ARTIQ [187]. In this thesis, IonControl was used to run the autoionizing experiments in Section 2, which consists of primarily a single FPGA for sending pulses with a 20 ns resolution. Given that gate times are on the order of microseconds for trapped ion experiments, this resolution is sufficient. ARTIQ is likely now the most popular existing solution for running trapped ion experiments, with many additional off-the-shelf solutions for running almost all aspects of a trapped ion experiment. This includes cards for direct digital synthesis for triggering AOMs, digital to analog converters for setting trap voltages, digital in/out for triggering, and high-frequency cards for modulating beams with EOMs. The ablation target neutral fluorescence collection experiments described in Section 3 were all ran on the hardware in Fig. B.1a. The electrical rack housing the ARTIQ system is on the outside of the air-handling unit (AHU). This is connected to the devices inside the AHU in another rack housing optical control devices in Fig. B.1b via the feedthroughs in Fig. B.1c. Thanks to Collin Epstein for taking the lead on setting up the initial ARTIQ system for the project.

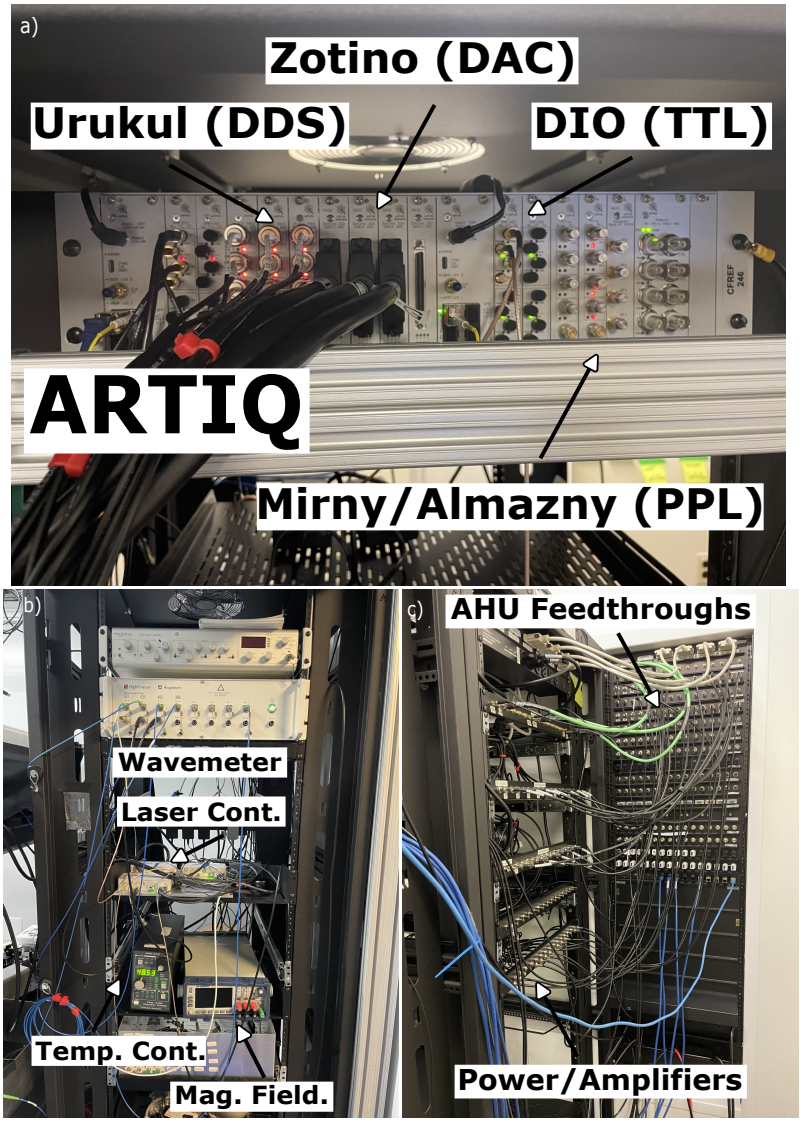


Figure B.1: a) Picture of the ARTIQ system used to run real-time experiments like that described in Chapter 3. b) Optical rack inside the air-handling unit (AHU), next to the optical table, housing crucial components like the wavemeter for locking lasers and the laser controllers. c) Outside of the AHU there are electrical racks holding power supplies and amplifiers. These signals are sent through the feedthrough on the AHU wall.

The optical rack in Fig. B.1b houses critical control devices such as a HighFinesse wavemeter (WS8-2), laser controllers from AOSense Inc., temperature controllers for fre-

quency doublers, a magnetic field controllers and so on. The majority of these devices can be sensitive to temperature and humidity fluctuations so they are placed inside the AHU. The are also modulators such as AOMs and EOMs (not shown) that are on the optics table for providing fast optical switching, amplitude-modulation, and sideband generation. These amplifiers and power supplies sit outside the AHU, inside the electrical rack, because they generate significant heat that would disturb air flow otherwise.

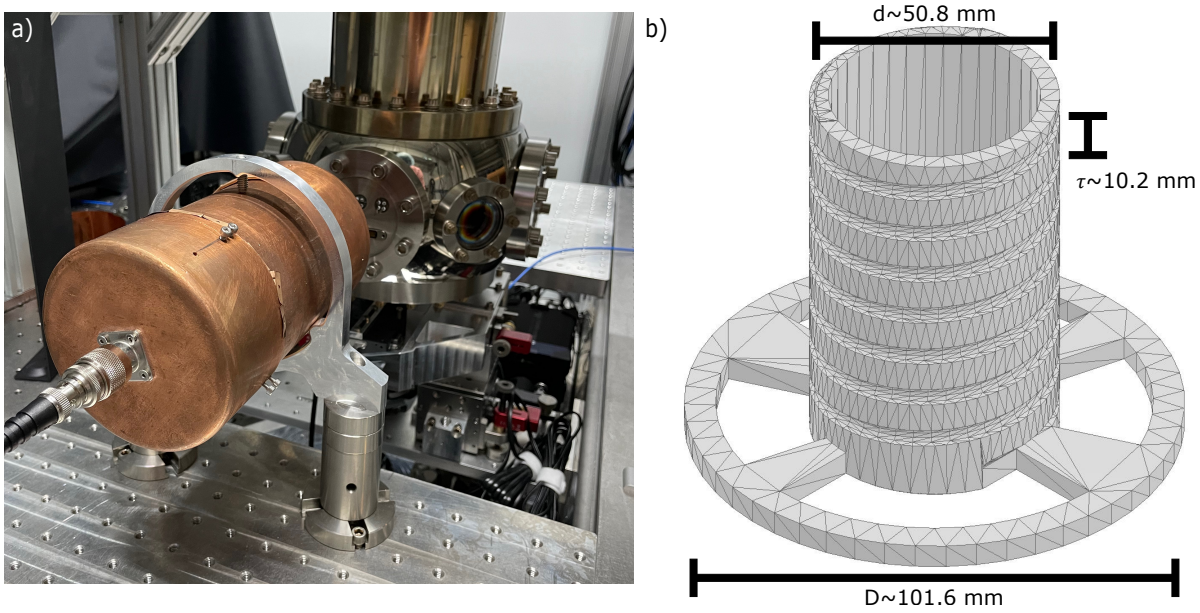


Figure B.2: a) Picture of the resonator on the optics table attached to the vacuum feedthrough. b) STL rendering of the 3D printed support structure for holding the main coil of the resonator in place.

Slight modifications to the resonator pictured in Fig. B.2 initially constructed by Ali Binai-Motlagh [151] are discussed. The desired unloaded frequency was originally measured at $\sim$ 74 MHz, however, the target loaded frequency for trap operation is 35-45 MHz and in practice, usually only a 10 MHz drop is observed when loading the resonator. The pitched $\tau \approx 10.2$ mm and main coil diameter $d \approx 50.8$ mm were modified to drop the unloaded resonance $\sim$ 25 MHz. Since the trap package from Sandia National Laboratories varies in capacitance for each trap ($\sim$ 16 pF), without having the resonator hooked up to the exact trap, it is unclear if more modifications will need to be made. A 3D printed supported was added to hold the $\sim$ 3 mm thick wire, as the main coil was previously unsupported. In terms of the big picture, the secular frequencies of the ions are related to the trap frequency

such that $\omega \propto 1/\Omega_{trap}$. So by using a lower trap frequency, the secular frequencies increase, which allows for faster gate times.

Appendix C

Amplitude-Modulated Entangling Gates

C.1 Code Description

The code for producing the results in Section 5 was written entirely in Python 3. The script consists of eight main sections. The first section in the Jupyter Notebook imports all of the necessary packages and defines the initial parameters. Some examples of the initial parameters defined are the Lamb-Dicke parameters, motional modes, detuning, Fock states, choice of Hamiltonian and so on. The second section is a block of code where commonly used functions are defined. These functions are used mainly in the next section where the spin and motional matrices are initialized. For most simulations, the ion spins are initialized to the "up" state and the motional states are initialized such that $\bar{n} = 0$. At the end of this third section, the initial density matrix, consisting of the spin and motional matrices, is converted to a row-reduced sparse matrix using *scipy.sparse*. Sparse matrices are useful tools for computing large Hilbert spaces on classical machines because they keep track of only the non-zero elements in a matrix, rather than each element individually [188]. Since the majority of the matrix elements in these simulations are zero, this drastically reduces memory requirements.

The fourth section or code block is where the modulated signals such as amplitude, frequency, or phase are generated. This section is commonly modified in order to investigated different amplitude-modulated entangling schemes. After having all of the signals and initial matrices generated, then the phase-space trajectories are calculated two different ways, one way is numerically using Simpson's rule [189] and the other way is analytically using

the function in Appendix C.2. After the phase-space trajectories are verified to close, the Rabi frequency is scaled by numerically solving the double integral for $\chi(t)$ using the trapezoidal rule. Optimization of the $\alpha(t)$ and $\chi(t)$ parameters comprises the fifth section of the code. Once these parameters are optimized, the next code block consists of solving the von Neumann equation for the desired Hamiltonian using density matrix formalism, which in most cases is the Mølmer–Sørensen Hamiltonian. This is done using a function written following the 4^{th} order Runge-Kutta method [190]. Typically at least 12000 steps are used to simulate a gate that is 50 μs.

Once the simulation is complete, there will now be a density matrix at each time step that can be measured in order to extract different matrix elements. This is done again using sparse matrices and in the same manner that the fidelity would be calculated in Eq. 5.7. Finally the last code block simply plots the calculated matrix elements. The code can be accessed at 10.5281/zenodo.10800833.

C.2 Analytical Expression for α_{ij} Integral using Double-Sideband Amplitude Modulation

$$
\begin{aligned}
\alpha_{ij} =& \eta_{ij}\Omega_o\Bigg(\frac{\tau}{2}\Bigg(- \frac{i\omega_j\tau}{(\omega_c\pi + (-\mu+\omega_j)\tau)(\omega_c\pi - (\mu+\omega_j)\tau)} \\
&+ \frac{i\omega_j\tau}{(\omega_c\pi + (\mu-\omega_j)\tau)(\omega_c\pi + (\mu+\omega_j)\tau)} \\
&+ e^{it\omega_j}\Bigg(\frac{i\omega_j\tau\cos\left[t\left(\mu-\frac{\omega_c\pi}{\tau}\right)\right] + (-\omega_c\pi+\mu\tau)\sin\left[t\left(\mu-\frac{\omega_c\pi}{\tau}\right)\right]}{(\omega_c\pi + (-\mu+\omega_j)\tau)(\omega_c\pi - (\mu+\omega_j)\tau)} \\
&- \frac{i\omega_j\tau\cos\left[t\left(\mu+\frac{\omega_c\pi}{\tau}\right)\right] + (\omega_c\pi+\mu\tau)\sin\left[t\left(\mu+\frac{\omega_c\pi}{\tau}\right)\right]}{(\omega_c\pi + (\mu-\omega_j)\tau)(\omega_c\pi + (\mu+\omega_j)\tau)}\Bigg)\Bigg) \\
&- m\Bigg(- \frac{\tau}{4}\Bigg(\frac{i\omega_j\tau}{(\omega_c\pi - \pi\omega_s + (-\mu+\omega_j)\tau)(\omega_c\pi - \pi\omega_s - (\mu+\omega_j)\tau)} \\
&+ \frac{i\omega_j\tau}{(\omega_c\pi + \pi\omega_s + (-\mu+\omega_j)\tau)(\omega_c\pi + \pi\omega_s - (\mu+\omega_j)\tau)} \\
&- \frac{i\omega_j\tau}{(\omega_c\pi - \pi\omega_s + (\mu-\omega_j)\tau)(\omega_c\pi - \pi\omega_s + (\mu+\omega_j)\tau)} \\
&- \frac{i\omega_j\tau}{(\omega_c\pi + \pi\omega_s + (\mu-\omega_j)\tau)(\omega_c\pi + \pi\omega_s + (\mu+\omega_j)\tau)}\Bigg) \\
&+ \frac{\tau}{4}e^{it\omega_j}\Bigg(\frac{i\omega_j\tau\cos\left[\frac{t(-\omega_c\pi-\pi\omega_s+\mu\tau)}{\tau}\right] - (\omega_c\pi+\pi\omega_s-\mu\tau)\sin\left[\frac{t(-\omega_c\pi-\pi\omega_s+\mu\tau)}{\tau}\right]}{(\omega_c\pi + \pi\omega_s + (-\mu+\omega_j)\tau)(\omega_c\pi + \pi\omega_s - (\mu+\omega_j)\tau)} \\
&- \frac{i\omega_j\tau\cos\left[\frac{t(\omega_c\pi-\pi\omega_s+\mu\tau)}{\tau}\right] + (\omega_c\pi-\pi\omega_s+\mu\tau)\sin\left[\frac{t(\omega_c\pi-\pi\omega_s+\mu\tau)}{\tau}\right]}{(\omega_c\pi - \pi\omega_s + (\mu-\omega_j)\tau)(\omega_c\pi - \pi\omega_s + (\mu+\omega_j)\tau)} \\
&+ \frac{i\omega_j\tau\cos\left[\frac{t(-\omega_c\pi+\pi\omega_s+\mu\tau)}{\tau}\right] + (-\omega_c\pi+\pi\omega_s+\mu\tau)\sin\left[\frac{t(-\omega_c\pi+\pi\omega_s+\mu\tau)}{\tau}\right]}{(\omega_c\pi - \pi\omega_s + (-\mu+\omega_j)\tau)(\omega_c\pi - \pi\omega_s - (\mu+\omega_j)\tau)} \\
&- \frac{i\omega_j\tau\cos\left[\frac{t(\omega_c\pi+\pi\omega_s+\mu\tau)}{\tau}\right] + (\omega_c\pi+\pi\omega_s+\mu\tau)\sin\left[\frac{t(\omega_c\pi+\pi\omega_s+\mu\tau)}{\tau}\right]}{(\omega_c\pi + \pi\omega_s + (\mu-\omega_j)\tau)(\omega_c\pi + \pi\omega_s + (\mu+\omega_j)\tau)}\Bigg)\Bigg)\Bigg)
\end{aligned}
\tag{C.1}
$$

C.3 Amplitude-Modulation in Long Ion Chains

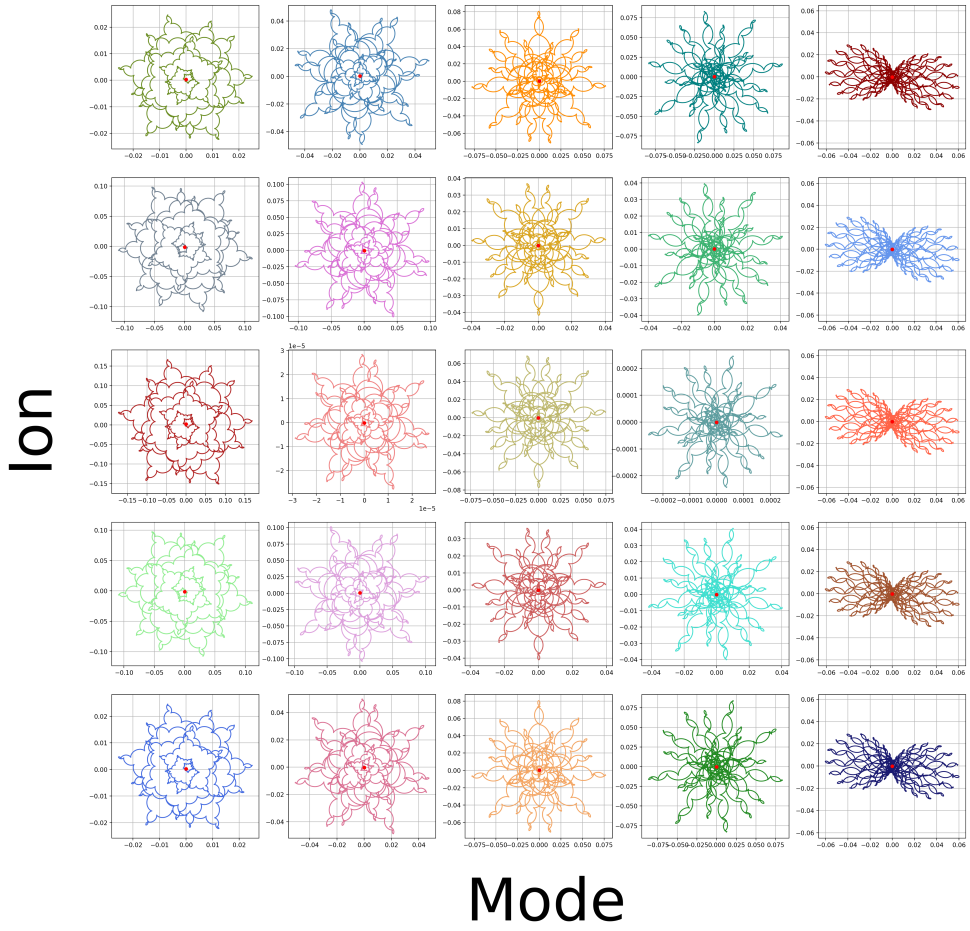


Figure C.1: Closed phase-space trajectories for a chain of five ion using the same optimization routine discussed in Section 5. Each row represents an ion coupled to a motional mode (which are represented by the columns). For a chain of five ions, there are five internal spin states to consider, each coupled to five motional modes, giving a total of 25 phase-space trajectories that must be closed.

In order to evaluate the feasibility of using double-sideband amplitude modulation in longer chains of trapped ions, an example with five ions is investigated. Full simulations are not calculated, but instead the $\alpha_{ij}(t)$ integrals relating to the phase-space trajectories for all ions with each motional mode are closed using a minimization function in Python. This example shows that with the right choice of detuning ($\mu = 24930380 \cdot 2\pi$ Hz) and gate time ($\tau \approx 54.298$ μs) as free parameters, that phase-space trajectories for all modes and spins can be closed *simultaneously*. This leaves the experimentalist to only determine the proper scaling factor Ω_o for entangling the desired ion pairs, which can be done by solving the integral $\chi(t)$. The motional modes ω, Lamb-Dicke parameters η_{ij}, and detuning are taken from [160]. The Lamb-Dicke parameters are also listed in Table C.2.

$$\eta_{ij} = \begin{bmatrix} 0.01248 & 0.03474 & 0.06091 & 0.07149 & -0.04996 \\ -0.05479 & -0.07263 & -0.03150 & 0.03406 & -0.05016 \\ 0.08428 & -0.00002 & -0.05848 & -0.00021 & -0.05013 \\ -0.05440 & 0.07306 & -0.03098 & -0.03459 & -0.04991 \\ 0.01243 & -0.03514 & 0.06094 & -0.07163 & -0.04946 \end{bmatrix} \tag{C.2}$$